SEDIMENT DYNAMICS DURING HEINRICH EVENT H1 INFERRED FROM GRAIN SIZE

by

Laura deGelleke

Submitted in partial fulfillment of the requirements
for the degree of Master of Science

at

Dalhousie University
Halifax, Nova Scotia
July 2011

© Copyright by Laura deGelleke, 2011

DALHOUSIE UNIVERSITY

DEPARTMENT OF OCEANOGRAPHY

The undersigned hereby certify that they have read and recommend to the Faculty of Graduate Studies for acceptance a thesis entitled "SEDIMENT DYNAMICS DURING HEINRICH EVENT H1 INFERRED FROM GRAIN SIZE" by Laura deGelleke in partial fulfillment of the requirements for the degree of Master of Science.

Dated: July 21, 2011

External Examiner: _____

Supervisors: _____

_____

Readers: _____

_____

DALHOUSIE UNIVERSITY

DATE: July 21, 2011

AUTHOR: Laura deGelleke

TITLE: SEDIMENT DYNAMICS DURING HEINRICH EVENT H1 INFERRED FROM GRAIN SIZE

DEPARTMENT OR SCHOOL: Department of Oceanography

DEGREE: M.Sc. CONVOCATION: October YEAR: 2011

Permission is herewith granted to Dalhousie University to circulate and to have copied for non-commercial purposes, at its discretion, the above title upon the request of individuals or institutions. I understand that my thesis will be electronically available to the public.

The author reserves other publication rights, and neither the thesis nor extensive extracts from it may be printed or otherwise reproduced without the author's written permission.

The author attests that permission has been obtained for the use of any copyrighted material appearing in the thesis (other than brief excerpts requiring only proper acknowledgement in scholarly writing), and that all such use is clearly acknowledged.

Signature of Author

For the Blue Planet

Table of Contents

List of Tables . . . . . **vii**

List of Figures . . . . . **viii**

Abstract . . . . . **x**

List of Abbreviations and Symbols Used . . . . . **xi**

Acknowledgements . . . . . **xiv**

Chapter 1 Introduction **1**

1.1 Significance 1

1.2 Overview 2

Chapter 2 Background **4**

2.1 Heinrich Events in the North Atlantic 4

2.2 Climatic Implications of Massive Freshwater Discharge 5

2.3 Anatomy of the Heinrich Layer 7

2.4 Plume Sedimentation 8

2.5 Oceanographic Setting 13

Chapter 3 Methods **16**

3.1 H1 Layer Identification 16

3.2 H1 Layer Thickness 19

3.3 Grain Size Analysis 20

3.4 Calcium Carbonate 23

3.5 Sand & Gravel 24

3.6 Inverse Floc Model 25

3.6.1 Formulation 27

3.7 Entropy Analysis 29

3.7.1 Formulation 30

Chapter 4 Results **32**
4.1 H1 Layer Thickness 32
4.2 DIGS Entropy Analysis 33
4.3 Calcium Carbonate and Sand-Gravel Content 38
4.4 Inverse Model Parameters 38

Chapter 5 Discussion **43**
5.1 Association of Textural Groups with Delivery Mechanisms 43
5.2 Unfolding the H1 Event Using Sediment Texture 44
5.3 Comparison with Facies Interpretations 50
5.4 Implications 50

Chapter 6 Conclusion **52**

Appendix A Core Summaries **53**

Appendix B Electronic Supplement **76**

Bibliography **77**

LIST OF TABLES

Table 3.1 Cores chosen for grain size analysis and determination of calcium carbonate and sand-gravel content. 22

LIST OF FIGURES

Figure 2.1 The δ^{18}O record from the GISP2 ice core in Greenland and an IRD record from deep-sea core in the North Atlantic showing the repeated occurrence of H events. 6

Figure 2.2 X-radiograph examples of the three H layer subunits A, B, and C. . 9

Figure 2.3 Diagram illustrating differences in sediment sorting between ice-rafting and plume delivery mechanisms. 10

Figure 2.4 Removal rate constants and percent present in the sediments by size fraction using SPM data from Bute Inlet, British Columbia. . . 12

Figure 2.5 General surface circulation in the North Atlantic. 14

Figure 3.1 Map of piston cores held in the repository at BIO. 17

Figure 3.2 Location of 11 cores with identified H1 layers chosen for grain size analysis and determination of calcium carbonate and sand-gravel content. 21

Figure 3.3 Conceptual basis for the inverse floc model. 25

Figure 3.4 Stylized DIGS distribution. 26

Figure 4.1 H1 layer thickness in cores from the western North Atlantic. . . . 33

Figure 4.2 H1 layer thickness by along-margin distance. 34

Figure 4.3 H1 layer thickness by cross-margin distance. 35

Figure 4.4 Entropy analysis of sample DIGS distributions. 36

Figure 4.5 Entropy grouping of DIGS distributions downcore. 37

Figure 4.6 Variability of % carbonate, % sand & gravel, and model parameters along-margin. 40

Figure 4.7 Variability of % carbonate, % sand & gravel, and model parameters cross-margin. 41

Figure 4.8 Variability of % carbonate, % sand & gravel, and model parameters in core. 42

Figure 5.1 Sand-gravel content by weight for all samples in each entropy group. 44

Figure 5.2 H1 layer thickness normalized to median carbonate content by along-margin distance. 48

ABSTRACT

Throughout the last glacial period, massive volumes of icebergs were discharged periodically from the Hudson Strait region during so-called Heinrich (H) events. These icebergs transported sediments that were subsequently deposited in distinct layers across the North Atlantic as they melted. The occurrence of H events has been correlated with disruptions in deep ocean circulation and cold events recorded in Greenland ice cores. The objective of this research was to measure and describe sedimentation associated with a meltwater plume discharged during the H1 ice-rafting event (14–19 ka) by examining sediment texture. The H1 layer was sampled in 11 piston cores that cover about 4000 km of the slope between Hudson Strait and the Bay of Fundy and range in water depth from 818–2740 m. Disaggregated inorganic grain size (DIGS) distributions were determined using a Coulter counter. Additionally, the $CaCO_3$ content and the > 63 μm fraction were measured and DIGS spectra were parameterized using an inverse floc model and sorted using entropy analysis. Entropy analysis proved to be a useful tool for distinguishing between delivery mechanisms and provided insights not necessarily evident from the results of other analyses. Results suggest that H1 layer sediments were mainly delivered by plume, ice-rafting and turbidites. In general, plume deposition was only significant proximally ($<$ 500–1000 km from source) during the event and distal sediments were mainly delivered by ice-rafting. However, the lack of plume deposited sediments distally does not necessarily imply the absence of a plume. Discrepancies between delivery mechanisms interpreted from sediment texture and facies highlight small scale variability of texture within facies that is often ignored and not always in agreement with facies interpretations.

List of Abbreviations and Symbols Used

Abbreviation	Description
H	Heinrich (event or layer)
H1–H6	Heinrich event 1–6
NADW	North Atlantic deep water
BIO	Bedford Institute of Oceanography
DIGS	disaggregated inorganic grain size
$^{230}Th_{xs}$	applied to sediment flux, 'excess' ^{230}Th or the scavenged portion of ^{230}Th in the sediment that was adsorbed onto sinking particles
LIS	Laurentide Ice Sheet
IRD	Ice-rafted detritus
$\delta^{18}O$	change in ratio of stable oxygen isotopes ^{18}O to ^{16}O relative to a standard
DC	Detrital Carbonate
D-O	Dansgaard-Oeschger events
SPM	suspended particulate matter
Sv	Sverdrup measure of volume transport equal to 10^6 m^3/s
NSOW	Nordic Sea Overflow Water
LSW	Labrador Sea Water
GSC-A	Geological Society of Canada - Atlantic
AMS	atomic mass spectrometry
MS3	Multi-sizer III Coulter Counter
CO_2	carbon dioxide
pH	logarithmic scale that measures the acidity or basicity of an aqueous solution
$CaCO_3$	calcium carbonate
H_2O_2	hydrogen peroxide
NaCl	sodium chloride

Symbol	Description	Units
μ	dynamic viscosity of seawater	$\mathrm{kg\,m^{-1}\,s^{-1}}$
ϕ	grain size logarithmic scale where $\phi = log_2 D/D_0$	–
ρ	density of seawater	$\mathrm{kg\,m^{-3}}$
ρ_s	density of sediment	$\mathrm{kg\,m^{-3}}$
A	y-intercept of exponential regression of thickness by distance on linear axes	m
A_n	y-intercept of exponential regression of thickness by distance on semilog-y axes	m
b	slope of exponential regression of thickness by distance	–
B	vertical sediment flux of reference diameter d_0	$\mathrm{kg\,m^{-3}}$
C	particle concentration	$\mathrm{kg\,m^{-3}}$
C_f	particle concentration of flocs	$\mathrm{kg\,m^{-3}}$
C_s	particle concentration of single grains	$\mathrm{kg\,m^{-3}}$
$\hat{d}$	falloff diameter	m
d_0	reference diameter	m
d_f	floc limit	m
D	diameter	m
D_{50}	median diameter of grains $< 100\ \mu$m	m
E	entropy	–
f	"floc fraction" in suspension	–
g	acceleration due to gravity	$\mathrm{m\,s^{-2}}$
h	plume thickness	m
i	particle size class	m
I	inequality statistic	–
I_B	inequality statistic between groups	–
j	spectrum number	–
J	number of spectra	–
K_f	fraction of flocs in seabed by weight	–
m	source slope	–
N	number of size classes	–
p_i	proportion of particles in size class i	–

Symbol	Description	Units
Q	mass concentration of reference diameter d_0	$\mathrm{kg\,m^{-3}}$
r	entropy group number	–
R	number of entropy groups	–
R^2	coefficient of determination	–
R_s	R-statistic that measures explained variability	–
u_0	plume speed	$\mathrm{m\,s^{-1}}$
VC_{ij}	volume concentration of particles in spectrum j, size class i	$\mathrm{m^3\,m^{-3}}$
w_f	floc settling velocity	$\mathrm{m\,s^{-1}}$
w_s	single grain settling velocity	$\mathrm{m\,s^{-1}}$
x	distance	m
Y_i	proportion of total volume concentration in size class i	–
Y_j	proportion of total volume concentration in spectrum j	–
Y_{ij}	proportion of total volume concentration in spectrum j, size class i	–
Z	vertical sediment flux	$\mathrm{kg\,m^{-3}}$
Z_f	vertical sediment flux of flocs	$\mathrm{kg\,m^{-3}}$
Z_s	vertical sediment flux of single grains	$\mathrm{kg\,m^{-3}}$

Acknowledgements

Foremost, I would like to thank my advisors Paul Hill and Markus Kienast for their assistance and guidance during the entirety of my research. Additionally, I would like to extend my gratitude to David Piper and Francky Saint-Ange at BIO for sharing their knowledge of cores in my study region, Kate Jarrett for her help in the GSC-A Core Processing Laboratory at BIO, and Tim Milligan and Brent Law at BIO for sharing their particle ideas and methods. At Dalhousie, Jessica Carrier-Garwood and Claire Normandeau were both of great assistance in the lab, and John Newgard generously shared his Matlab expertise. Lastly, I thank my family and friends for their support during my studies.

CHAPTER 1

INTRODUCTION

1.1 Significance

Throughout the last glacial period, massive volumes of icebergs were discharged periodically from the Hudson Strait region during so-called Heinrich (H) events [*Broecker et al.*, 1992]. These icebergs transported sediments that were deposited in distinct layers across the North Atlantic as they melted. *Hemming* [2004] estimated a total discharge of 3×10^4 km^3 to greater than 5×10^6 km^3 of ice was required to account for the sediment deposited across the deep North Atlantic ocean. This is roughly the same volume necessary to fill the Mediterranean Sea! H events are truly epic episodes in Earth's geological past and their occurrence has been correlated with disruptions in deep ocean circulation and cold events recorded in Greenland ice cores.

Since their recognition by *Heinrich* [1988], H layers and the events responsible for their deposition have received much attention from the scientific community. The nature of H events and their correlation with climate fluctuations makes them excellent examples of recent ocean-atmosphere-cryosphere interaction that have attracted considerable interest, especially in light of the imminent climate changes facing today's society. Research on H events has largely been focused on timing, duration and provenance, with the assumption that the significant mechanism of sediment transport is iceberg rafting [*Andrews*, 1998]. However, considerable evidence indicates that depositional and transport processes are much more complicated in ice-proximal regions where debris flows and turbidites are common [*Andrews et al.*, 1994; *Wang and Hesse*, 1996]. The character of sediments

deposited proximally in the Labrador Sea indicates that H ice-rafting events were accompanied by massive meltwater discharge rich in carbonate sediments [e.g., *Hillaire-Marcel et al.*, 1994; *Hesse and Khodabakhsh*, 1998; *Rashid et al.*, 2003b] that likely occurred prior to the launching of icebergs across the North Atlantic [*Hemming*, 2004]. However, little attention has been given to understanding the sedimentation associated with this meltwater discharge.

Sediment and meltwater discharged during H events are advected great distances with the prevailing currents and have significantly affected the hydrology of the region. Distinct H layers have been identified in the Labrador Sea [*Andrews and Tedesco*, 1992] and across the North Atlantic [e.g., *Bond et al.*, 1992; *Grousset et al.*, 1993; *Dowdeswell et al.*, 1995] as far as the Iberian margin [e.g., *Lebreiro et al.*, 1996; *Bard et al.*, 2000]. Additionally, fine-grained sediment originating from the Scotian margin has been found to complicate the interpretation of the sediment record in drifts on the Bermuda Rise [*Ohkouchi et al.*, 2002]. Evidence from foraminifera indicates that low temperature and low salinity surface waters extended much farther south during H events [*Bond et al.*, 1992; *Hillaire-Marcel et al.*, 1994]. Multiple proxies have been used to suggest that hydrological changes in surface waters across the North Atlantic during H events caused a reduction of North Atlantic Deep Water (NADW) formation [*Keigwin and Lehman*, 1994; *McManus et al.*, 2004] and models have demonstrated this possibility [*Stocker*, 2000; *Khodri et al.*, 2003]. Investigating the sediment transported by a meltwater component of H events will help constrain the discharge and better our understanding of ice sheet dynamics and their effect on NADW formation and climate. Additionally, insight into how the Earth system reacts to a large North Atlantic meltwater input may help develop strategies to address this possibility in the future.

1.2 Overview

This research aims to build an understanding of the meltwater component of the H1 ice-rafting event that occurred from about 19 to 14 ka by investigating the sedimentary character of H1 layers in marine sediment cores from the Labrador and Scotian slopes stored at the Bedford Institute of Oceanography (BIO), Dartmouth, NS, Canada. Specifically, H1 layer thickness and the < 100 μm grain size distribution in H1 layers are examined across the region in attempt to identify plume-style sediment deposition. Cores were chosen

mainly for spatial representation of the region, and priority was given to newer cores and well-studied cores. The major challenge of this research was to tease out a plume-style sediment deposition signature from cores where sediments were delivered by a variety of mechanisms. Comparing disaggregated inorganic grain size (DIGS) distributions of core samples measured using a Coulter Counter with entropy analysis allowed identification of major sediment delivery mechanisms during the H1 event. Investigating sediment texture across the entire DIGS size spectra provides insight into the H1 event not necessarily available from facies interpretations or more traditional grain size statistics alone. Here, I present relevant background information, methods, results, and a discussion including a spatial and temporal description of the H1 event in the context of my results.

CHAPTER 2

BACKGROUND

2.1 Heinrich Events in the North Atlantic

Heinrich [1988] documented evidence from marine sediment cores for the occurrence of six short-lived episodes of sudden and intense iceberg discharge into the North Atlantic during the Late Pleistocene (126–10 ka). During these episodes, icebergs transported sediments that were deposited in distinct layers as the ice melted across the North Atlantic, mainly between 40–50°N [*Ruddiman*, 1977; *Heinrich*, 1988; *Bond et al.*, 1992; *Broecker et al.*, 1992]. These H layers occur repeatedly through the sediment record for the last 70 ka and are labeled H1–H6 (Fig. 2.1, bottom) [*Bond et al.*, 1992]. Ice-rafting events older than 70 ka have been documented [*Heinrich*, 1988], but are not as distinct, may have different sources, and are not normally penetrated with piston cores in high sedimentation-rate areas such as the Labrador Sea [*Rashid et al.*, 2003b]. The duration of H events has been estimated using analytical techniques such as ^{14}C dating [e.g., *Andrews and Tedesco*, 1992] and $^{230}\mathrm{Th}_{xs}$ method [e.g., *Francois and Bacon*, 1994; *Veiga-Pires and Hillaire-Marcel*, 1999]. *Hemming* [2004] surveyed published duration estimates and found a range from 208 to 2280 yrs with an average duration of 495±255 yrs. Overall, there is an eastward thinning of H layers across the North Atlantic that supports a sediment origin in Canada [*Hemming*, 2004]. Additionally, the presence of detrital carbonate within lithic layers and the geochemical signature of the non-carbonate fraction have led to the conclusion that the major source of icebergs during these ice-rafting events was the Laurentide Ice Sheet (LIS) discharging from the northwest Labrador Sea near Hudson

Strait [*Andrews and Tedesco*, 1992; *Bond and Lotti*, 1995; *Gwiazda et al.*, 1996; *Hemming et al.*, 2000]. (It should be noted that H3 and H6 are somewhat different in character from other H events, but these differences are not discussed here.) Various mechanisms have been suggested to explain the occurrence of Heinrich events including catastrophic ice sheet purging [*MacAyeal*, 1993], ice-dam breaching (jökulhlaup activity) [*Johnson and Lauritzen*, 1995], and ice shelf buildup/collapse [*Hulbe*, 1997; *Hulbe et al.*, 2004]. However, the cause of the ice sheet collapse still remains a topic of debate.

In North Atlantic deep sea sediment cores, H layers were first identified by a sudden increase in coarse-grained detrital carbonate and lithic fragments called ice-rafted detritus (IRD) because the presence of such coarse grains in deep sea sediments can only be explained by iceberg delivery. Additionally, North Atlantic H layers are characterised by reduced concentration of foraminifera, light δ^{18}O values in planktonic foraminifera, low gray-level colour values (high reflectivity), and high magnetic susceptibility [*Heinrich*, 1988; *Bond et al.*, 1992; *Broecker et al.*, 1992; *Grousset et al.*, 1993]. In the northwest Labrador Sea, correlative detrital carbonate (DC) layers were identified by *Andrews and Tedesco* [1992]. These DC events are equivalent to H events in the North Atlantic, but include sediment delivered by other ice-proximal transport processes that results in a somewhat different anatomy [*Rashid et al.*, 2003a]. Here, both North Atlantic H layers and Labrador Sea DC layers are referred to as H layers and are composed of one or more subunits described in Section 2.3. H layers near the Hudson Strait are enriched in fine-grained DC at concentrations that could not have been delivered by ice-rafting alone and suggest delivery by a meltwater plume [*Hesse and Khodabakhsh*, 1998].

2.2 Climatic Implications of Massive Freshwater Discharge

The occurrence of H events has been correlated with climate fluctuations recorded in the Greenland Summit ice cores GISP2 and GRIP [*Bond et al.*, 1993; *Dansgaard et al.*, 1993; *Broecker*, 1994]. *Dansgaard et al.* [1993] identified climate oscillations termed Dansgaard-Oeschger (D-O) events in the Greenland GRIP ice core that consist of an abrupt (within decades) warming to near-interglacial conditions followed by a gradual cooling. A total of 25 of these D-O events have been observed and occur about every 1,500 yrs during the last glacial period. The 20 most recent D-O events are labeled on

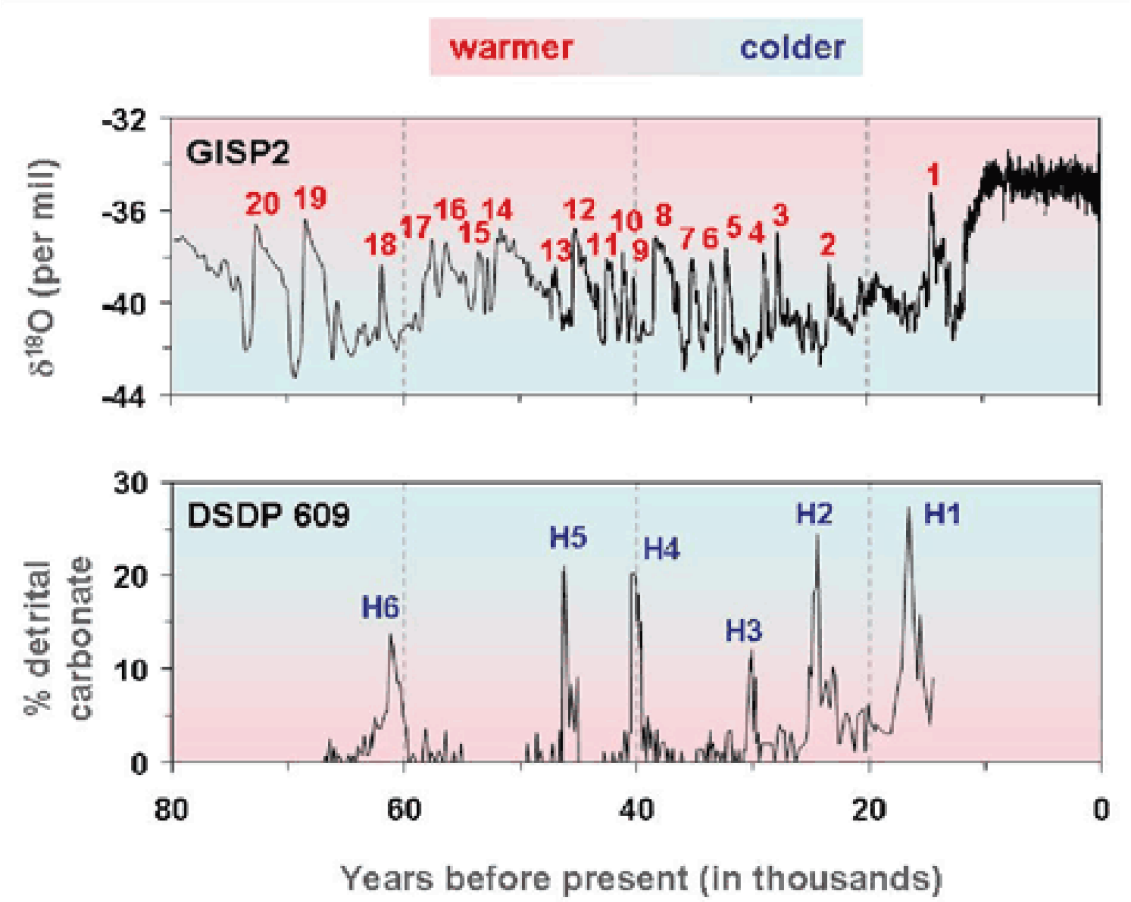

Figure 2.1: (Top) The δ^{18}O record from the GISP2 ice core in Greenland, showing 20 of the 25 observed D-O events during the last glacial period. (Bottom) A record of ice-rafted material during H events from a deep-sea core in the North Atlantic. For reference, dashed lines appear every 20 ka. Figure from *http://lwf.ncdc.noaa.gov/paleo/abrupt/data3.html*, data from *Grootes et al*. [1993] and *Bond and Lotti* [1995].

the GISP2 δ^{18}O record in Fig. 2.1, top. A lower-frequency cycle occurring every 3,000–8,000 yrs, called a Bond cycle, is superimposed on the pattern of D-O cycles [*Bond and Lotti*, 1995]. D-O events are packaged into Bond cycles in which successive D-O events become progressively colder. H events occur at the end of the Bond cycle, during the coldest D-O event.

Since the correlation of H events with Greenland temperature oscillations by *Bond et al.* [1993], records of climate variability from around the world have also been found to coincide with the variability recorded in the Greenland ice cores. Millennial-scale variability similar to that seen in Greenland ice cores has been observed in Antarctic ice cores [e.g., *Blunier and Brook*, 2001; *Brook et al.*, 2005], marine sediment cores [e.g., *Schulz et al.*, 1998; *Peterson et al.*, 2000; *Hendy and Kennett*, 2000; *Stott et al.*, 2002], lake sediments [e.g., *Benson et al.*, 1996; *Allen et al.*, 1999], and cave stalagmites [e.g., *Wang et al.*, 2001; *Genty et al.*, 2003; *Cruz et al.*, 2005]. The abrupt nature of the variability and the correlation of global records suggests the occurrence of H events is intimately linked to the global ocean-atmosphere system. However, the mechanism driving this variability is not well understood. It has been suggested that changes in sea surface salinity associated with H events may reduce deep water formation in the North Atlantic and affect the global thermohaline circulation responsible for much of the planet's heat redistribution. Indeed, evidence from marine sediment cores supports a reduction or shutdown of NADW formation associated with the H1 event [*Hillaire-Marcel et al.*, 1994; *Keigwin and Lehman*, 1994; *Elliot et al.*, 2002; *McManus et al.*, 2004; *Gherardi et al.*, 2009], and models have shown this is a possibility [*Clark et al.*, 2002; *Rahmstorf*, 2002]. In general, research shows that massive meltwater discharge can have a significant effect on ocean circulation and the global climate and likely has in the past. Careful analysis of the sediments in H layers can help build an understanding of meltwater dynamics.

2.3 Anatomy of the Heinrich Layer

The composition of H layers is different from core to core. This variability makes identification and accurate recording of layer thickness difficult. However, previous work has identified H layer subunits and spatial trends in their presence that are used as guidelines for identification and characterisation [*Hesse and Khodabakhsh*, 2006; *Rashid et al.*,

2003b]. Three H layer units (A,B, and C from the bottom-up) are recognized here following *Rashid et al*. [2003b], and examples are shown in Fig. 2.2. Unit A is characterised by significant amounts of coarse IRD incorporated into hemipelagic sediment. Unit A has a gradational contact at the base and sedimentary structures are not present except near the top of the unit where faint lamination begins. Unit B is typically the thickest subunit in the Labrador Sea region and comprises many graded mud beds and alternating mud turbidite deposits and thin IRD lamina. The contact is sharp at the base of unit B where unit A is absent. The muds in unit B are carbonate-rich (often $>50\%$ $CaCO_3$ by weight) with low magnetic susceptibility and contain sparse foraminifera with light $\delta^{18}O$. Unit C is composed of carbonate-rich hemipelagic mud with IRD. Lamination begins to diminish at the bottom of unit C with increasing absence of sedimentary structures toward the subunit top. The IRD and dropstone content also increases toward the top of unit C. The transition from unit C to the overlying sediments can be gradual or abrupt.

The spatial distribution of subunits in the Labrador Sea has allowed *Rashid et al*. [2003b] to make inferences about depositional mechanisms. Unit A is only found at the base of H layers in Labrador Sea cores from the shelf margin and upper slope, where it is overlain by units B and C. Units B and C are found in H layers from the slope and much of the basin of the Labrador Sea. Only unit C is found in cores outside the Labrador Sea, and it is this subunit that was originally defined as an H Layer by *Heinrich* [1988] and others. Unit A is interpreted to result from sediment released from the basal layer of the floating ice margin that extended to the shelf margin in most places. Unit B represents deposits from low concentration particle suspensions or nepheloid layers over the shelf and slope region. It also comprises turbidites and IRD. Unit C represents a waning supply of fines resulting from decreased nepheloid flow as the ice margin retreated. The concentration of IRD in unit C increased as intense ice-rafting continued. Gradual transition from unit C to overlying sediments is typically interpreted to be a result of post-depositional bioturbation. Together, the anatomy of H layers indicates massive iceberg and meltwater discharge of a magnitude much greater than any modern analogue.

2.4 Plume Sedimentation

Plume sedimentation can be distinguished from ice-rafting deposition because the former sorts sediment based on size, while the latter does not. This is illustrated schematically in

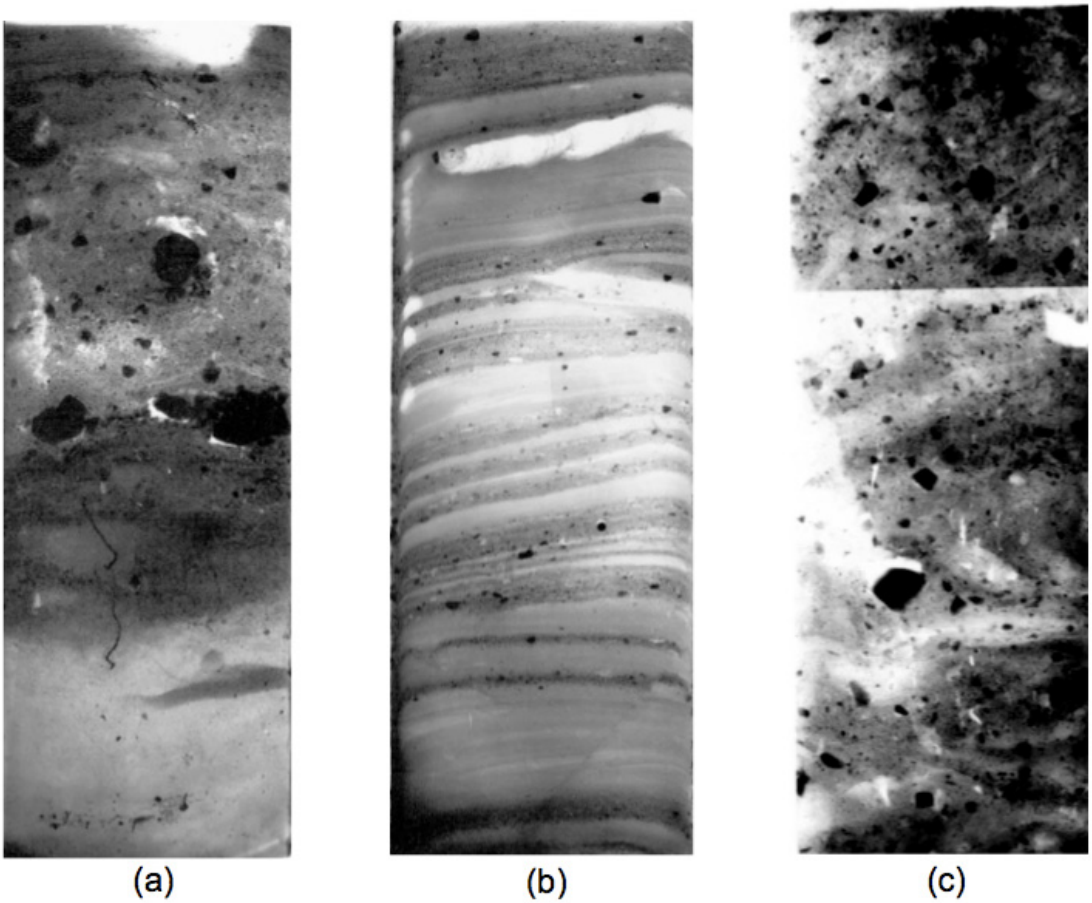

Figure 2.2: X-radiograph examples of the three H layer subunits A, B, and C. (a) Hemipelagic sediments with abundant coarse IRD (Hu97-048-16, 833–860 cm). (b) Nepheloid flow deposits (Hu97-048-16, 509–536 cm). (c) Carbonate-rich hemipelagic sediment with IRD (Hu97-048-09, 115–142 cm). From *Rashid et al*. [2003b].

Fig. 2.3 where sediment is being delivered to the seafloor by both icebergs and meltwater discharged from the same source. *Syvitski et al*. [1988] described a simple model for transport of sediment from the continents to the oceans based on data collected in fjords. They divided sediment processes at the deltaic land-sea interface into four main types: bedload dumping at the river mouth, river plume sedimentation, sediment bypassing processes (i.e. turbidity currents, slope failure), and diffusion processes (i.e. tides, waves). In regard to sediment delivery through meltwater discharge, we are mainly concerned with freshwater plume sedimentation because of the potential of freshwater plumes to affect global climate through interaction with the atmosphere. In their simple model, the plume is treated as a buoyancy-dominated, free, two-dimensional jet discharging into an ocean basin. If the concentration of total suspended particulate matter (SPM) at the river mouth is C_0, and assuming uniform particle size and first-order removal from the water column, the change in water column SPM in size class i can be written as

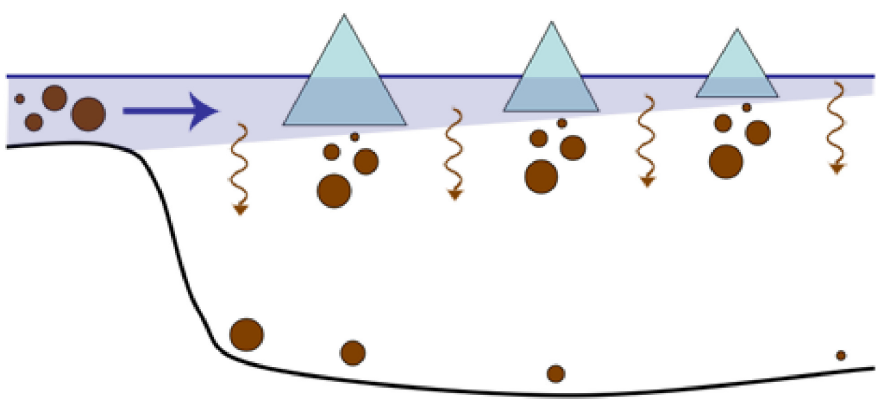

Figure 2.3: Diagram illustrating differences in sediment sorting between ice-rafting and plume delivery mechanisms. Sediment delivered by icebergs is not sorted while sediment delivered by plume is sorted by grain size with distance from the source.

$$\frac{dC(i)}{dt} = -\lambda C(i), \tag{2.1}$$

which can be integrated over boundary conditions to give

$$C(i) = C_0(i)e^{-\lambda t}. \tag{2.2}$$

The λ variable is a decay constant with units of inverse time. Letting $w_s(i)$ be the diameter-dependent sinking speed of a suspended particle and h be the plume thickness, it follows that λ is proportional to $w_s(i)/h$. If x is the distance along the plume trajectory and u_0 is the plume velocity (assumed constant), then $t = x/u_0$ can be substituted into Eq. 2.2 to give

$$C(i) = C_0(i)e^{-\frac{w_s(i)x}{hu_0}}. \tag{2.3}$$

Assuming removal of SPM from the water column occurs only by sedimentation, then the vertical sediment flux, $Z(x)$, is the product of settling velocity and concentration, giving

$$Z(x,i) = w_s(i)C_0(i)e^{-\frac{w_s(i)x}{hu_0}} \tag{2.4}$$

This model makes two important predictions. First, it predicts that sedimentation rate will decrease exponentially with increasing distance from the source. Second, the model predicts a fining of sediments in the bed with increasing distance from the source. *Syvitski et al*. [1988] verified both predictions using SPM data from sediment traps in Bute Inlet, British Columbia, Canada. In Fig. 2.4, the inorganic sediment inventory, $C(i)$, collected from a surface plume is used to calculate the removal rate constant for each size fraction which is used to predict the percentage of each size fraction in the bottom sediments with distance from the river mouth. Removal rate decreases with decreasing grain size and results in a fining of grains in the bottom sediments with distance from the plume source. These predictions agree well with most observations [e.g. *Geyer et al*., 2004; *Hill et al*., 2007].

If there is significant single-sourced meltwater discharge during H1, one would expect to find a thinning of the H1 sediment layer and a fining of the sediment grains within the layer moving further from the Hudson Strait region. This plume signature would be complicated by other modes of concurrent sedimentation, most notably sediment delivery by ice-rafting. Sediment of all sizes is carried on the ocean surface in icebergs that release sediment to the underlying bed as they melt. In this way, ice-rafting can be thought of as a moving river mouth and would contain sediment of all sizes with much coarser grains than would be expected under normal hemipelagic conditions. The difference in sediment grain size signatures of H1 layers in cores from the eastern Canadian margin will be

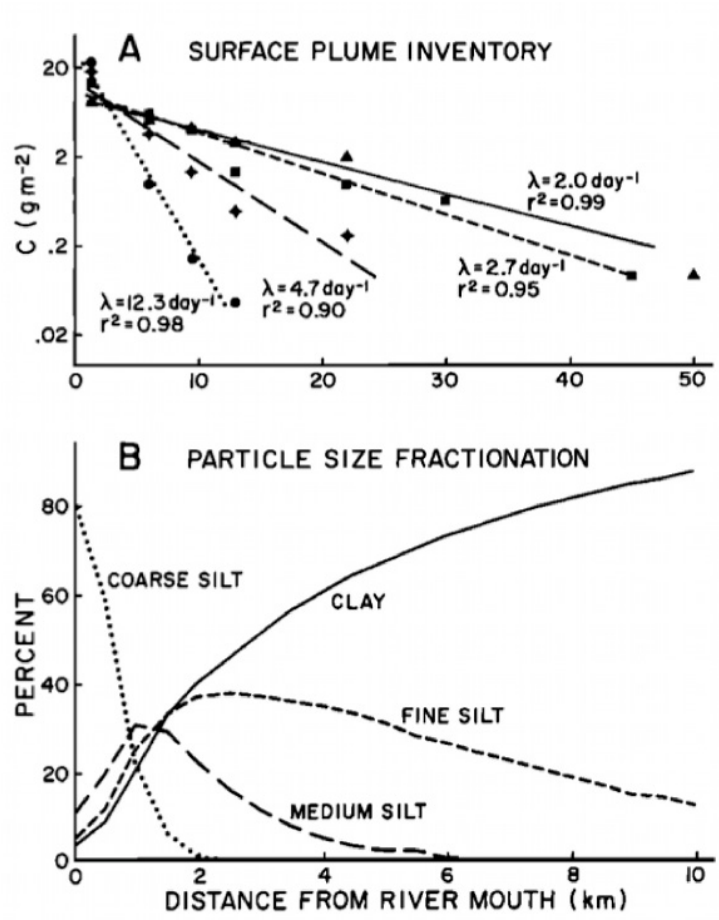

Figure 2.4: SPM data from Bute Inlet, British Columbia is used to calculate (a) the removal rate constants for each size fraction and to predict (b) the percentage of each size fraction present in the bottom sediments with distance from the river mouth. Figure from *Syvitski et al*. [1988].

interpreted to infer the relative contribution of plume and ice-rafted sedimentation during the H1 event.

2.5 Oceanographic Setting

In order to understand sediment transport during H events and hydrological changes associated with freshwater discharge, the general circulation of the North Atlantic must be considered. The easterly trade winds in the tropics and the mid-latitude westerlies generate an anticyclonic (clockwise) subtropical gyre between ∼10–45°N and a cyclonic (counterclockwise) subpolar gyre above ∼45°N (Fig. 2.5). The North Atlantic subtropical gyre has a particularly intense western boundary current known as the Gulf Stream which continues across the Atlantic as the North Atlantic Current. South of the Grand Banks (∼50°W), the Gulf Stream transports approximately 70 Sv of water from the tropics northward, making it the strongest western boundary current of the world's oceans [*Schmitz and McCartney*, 1993]. The North Atlantic Current splits as it approaches the European margin. Most of the current continues northeast into the subpolar region along the Subarctic Front, and some is carried southward in an eastern boundary current called the Canary Current to continue circulation in the subtropical gyre.

Part of the subpolar flow proceeds north into the Norwegian Sea and part of the subpolar circulation makes its way westward past Iceland and around Greenland into the Labrador Sea. Western boundary currents in the subpolar gyre are found along the eastern side of Greenland (East Greenland Current) and along the Labrador coast (Labrador Current). The cold Labrador Current meets the warmer North Atlantic Current near the Grand Banks leading to complicated circulation patterns. Inshore of the North Atlantic Current there is southward flow between Newfoundland and Flemish Cap, and north of the separated Gulf Stream there is westward flow along the continental slope (Slope Water Current).

The Gulf Stream and North Atlantic Current redistribute heat from the tropics poleward and play a key role in driving the global thermohaline circulation. The warm, salty water transported from the tropics by the Gulf Stream and North Atlantic Current is cooled in the subpolar region to form deep water. NADW components are formed in the Nordic and Labrador Seas as Nordic Sea Overflow Water (NSOW) and Labrador Sea Water (LSW) respectively. NADW is transported south in the Deep Western Boundary Current and

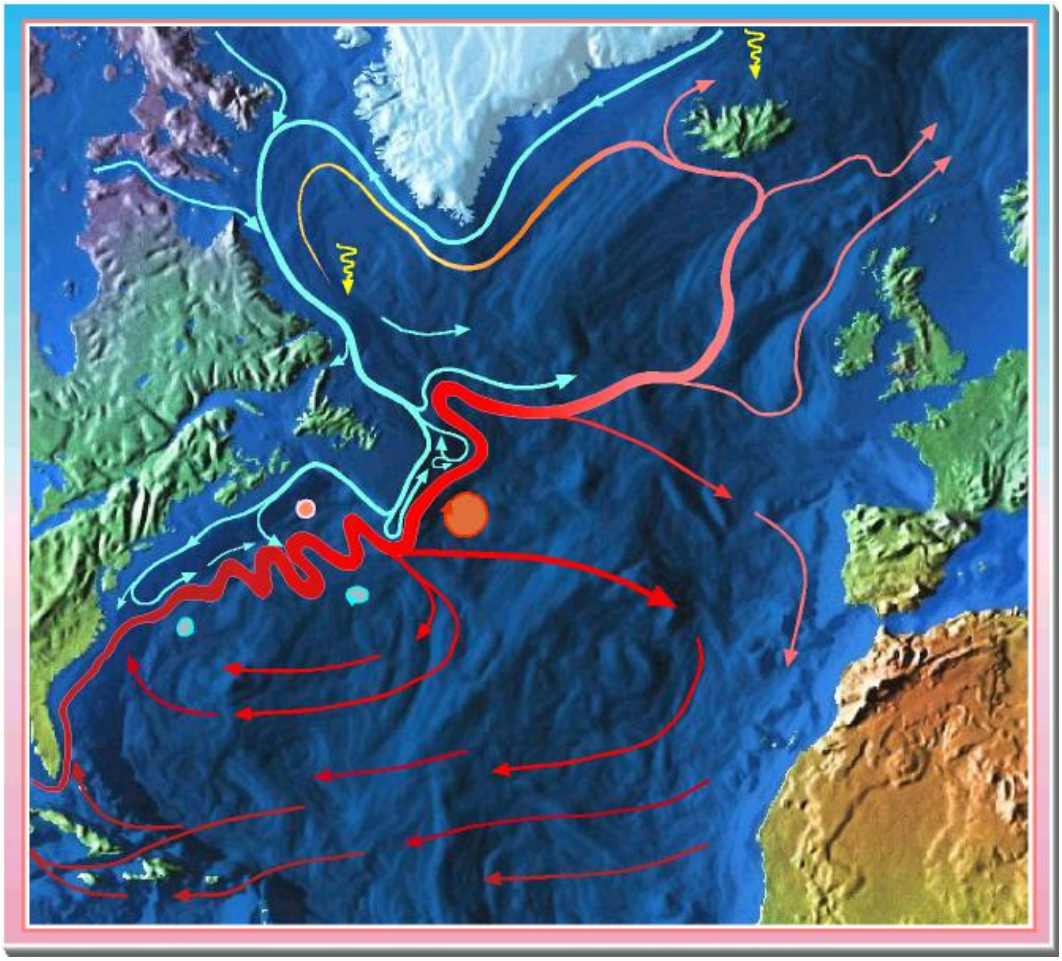

Figure 2.5: General surface circulation in the North Atlantic region between roughly 85°W to 5°E and 15–80°N. Warm water currents and eddies are drawn in red and cold water currents and eddies are drawn in blue. Deep water formation is shown as a curved, downward-pointing yellow arrow. From Igor Yashayaev, BIO.

injected into the western interior of the subtropical gyre.

The North Atlantic Ocean is the most studied of the world's oceans, yet a thorough explanation and description of the circulation of the region is still lacking [*Schmitz and McCartney*, 1993]. This is especially true in the region near the Scotian margin and the Grand Banks of Newfoundland where the Gulf Stream meanders considerably and sheds eddies as it meets colder water and peels away from the eastern seaboard across the Atlantic. Much less is known about the past circulation of the North Atlantic. While it is reasonable to expect some differences in past circulation, the ocean basin shape, wind forcing, and Coriolis forcing that result in the current general circulation pattern are not expected to have been significantly different during the H1 event approximately 16 ka. Meltwater and icebergs discharged from the Hudson Strait region during the event would have been advected south in a surface plume along the shelf edge in the Labrador Current. At Orphan Basin, some discharge would be advected eastward across the ocean in the North Atlantic Current while some would continue south through Flemish Pass, around the Tail of Grand Banks, and along the Scotian Slope.

CHAPTER 3

METHODS

As of October, 2008, a total of 2,258 piston cores from the general study area were available for investigation at BIO (Fig. 3.1). In order to maintain a manageable scope, focus was placed on the 614 piston cores recovered since 1999 (shown in red).

If significant plume sedimentation is associated with the H1 event, then one would expect to find a thinning of the sediment layer *and* a fining of the sediment grains within the layer with increasing distance from the Hudson Strait region (See Section 2.4). Accordingly, both H1 layer thickness and grain size distributions within H1 layers were investigated. Due to time and resource constraints, a subset of the cores whose H1 layer thickness was measured was chosen for grain size analysis and determination of calcium carbonate and sand-gravel content. An inverse floc model and entropy analysis were used to examine grain size distribution variability.

3.1 H1 Layer Identification

A variety of data were obtained from published articles, BIO technical reports, and internally shared core photography and physical data to aid in identifying H1 layers and determining thicknesses in the post-1999 piston cores. This approach was necessitated by the fact that the presence of H layers can be determined by a variety of parameters, and no single parameter was consistently available for every core. The following parameters were typically available from the BIO GSC-A Core Processing Laboratory and used to identify the presence and thickness of the H1 layer in the surveyed cores.

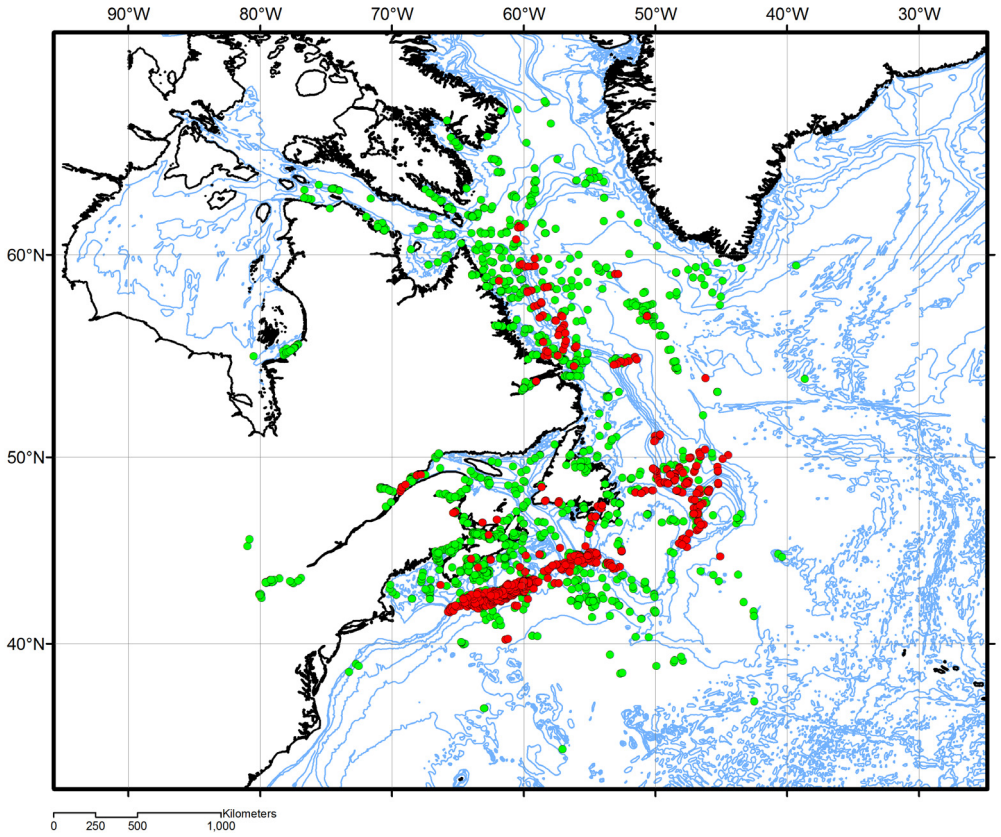

Figure 3.1: Location of all piston cores (2,258 total) held in the repository at BIO. The post-1999 piston cores (614 total) are shown in red.

Core photography Photographs of the archived half of most recently recovered cores were taken using a Nikon D100 six megapixel digital camera. Overlapping digital photographs were taken at 30 cm and 90 cm scales. Depth in the core was indicated by metre tape in each photograph and Munsell colour swatches were placed adjacently for comparison. H layers in the Labrador Sea can often be identified visually by increased IRD content and lighter colour that results from high detrital carbonate content.

X-radiographs Radiographs of 1 cm thick slabs taken from the split core provide a valuable tool for visually identifying the position and thickness of the H1 layer and subunits.

% IRD H layers were originally defined by *Heinrich* [1988] based on high levels of coarse lithic grains > 180 μm. Since then, it has become more common to use the > 150 μm fraction.

Reflectance L^* colour value Reflectance in the visual spectrum on the split core face was measured using a Minolta Spectrophotometer CM 2002 with measurements expressed in terms of the L^*, a^* and b^* values following ASTM E308-85 and E1164-02. The $L^*a^*b^*$ system represents coordinates in 3-dimensional space where the L^* represents lightness, a^* represents chroma (red to green), and b^* represents hue (blue to yellow). The L^* value ranges from zero (black) to 100 (white). Decreased L^* has been shown to be a useful proxy for IRD content and magnetic susceptibility [e.g., *Grousset et al.*, 1993] while increased L^* is a useful proxy for DC content [e.g., *Rashid et al.*, 2003b].

% $CaCO_3$, % calcite, % dolomite H layers in the Labrador Sea were originally defined by their high detrital limestone and dolomite content and H layers across the Atlantic have been identified by high DC content [e.g., *Broecker et al.*, 1992; *Andrews and Tedesco*, 1992]. A variety of techniques are used to measure the detrital carbonate content contribution to H layer sediments including CO_2 coulometry, infrared gas analysis, Mg/Ca weight fraction, Mg/Al weight fraction.

Magnetic susceptibility (SI units) Unopened cores are analysed by a Geotek multi-sensor track device to measure bulk density, P-wave velocity and magnetic susceptibility.

Changes in the oscillator frequency caused by material that has a magnetic susceptibility is measured and converted into magnetic susceptibility values. High whole-core magnetic susceptibility has been associated with increased carbonate content, but high DC content results in low magnetic susceptibility [*Grousset et al.*, 1993].

Bulk density (mg/m^3) Before splitting, cores are analysed by a Geotek multi-sensor track device to measure bulk density, P-wave velocity and magnetic susceptibility. Additionally, bulk density can be measured from constant volume samples following ASTM D2216-98. H layers often have increased bulk density due to high IRD content. However, high bulk density is also observed outside H layers, particularly in sand beds, and must be used with caution.

^{14}C dating Carbon-bearing material in samples from many cores has been radiometrically dated using the atomic mass spectrometry (AMS) technique. H events are cyclic and unconformities in the sediment record are common, so an absolute date is often helpful in determining which H events have been preserved in the sediment record.

δ^{18}O (‰) Changes in the amount of water stored on land as ice result in changes in the ratio of stable isotopes ^{18}O:^{16}O in the seawater due to fractionation processes. This ratio is recorded in the carbonate shells of foraminifera that can be picked from core samples and analysed. As a result of the melting of ice and the return of isotopically light water to the ocean, H events are typically associated with low planktonic and benthic δ^{18}O [e.g., *Bond et al.*, 1992; *Rasmussen et al.*, 2003].

3.2 H1 Layer Thickness

The total thickness of the H1 layer was recorded in 104 of the 614 post-1999 piston cores and along-margin distance from the mouth of Hudson Strait was estimated ($\pm$ 100 km) to represent the distance the plume would have travelled to the core location with the prevailing current. Typically, the H1 layer was defined by carbonate content, most often indirectly from visual or digital detection of lightness but occasionally directly from calcite and/or dolomite measurements. Unfortunately, this definition often excludes the darker subunit A when present. If present, subunit A is the smallest subunit and is not

expected to contain substantial plume delivered sediments so this deficiency is accepted here. Other parameters were used in conjunction with carbonate content for confirmation and less frequently for definition. Because of the inconsistency in the parameters used to define the layer, these thicknesses are not to be interpreted as exact and have an estimated 1–10% error associated with them. This problem is not unique and the lack of a consistent and widely applicable H layer definition has been noted by other researchers as stated by *Hemming* [2004].

3.3 Grain Size Analysis

Eleven cores with confirmed H1 layers were selected for grain size analysis, with their locations shown in Fig. 3.2 and summarized in Table 3.1, along with other attributes. These cores were chosen by location to represent the study area and cover approximately 4000 km off the margin between Hudson Strait and the Bay of Fundy and range in water depth from 818–2740 m. Core locations allow construction of a proximal to distal along-margin transect of 8 cores and a cross-margin transect of 4 cores in Orphan Basin. Complex sediment transport processes characteristic of Orphan Basin [e.g., *Tripsanas and Piper*, 2008] may complicate interpretation of the cross-margin transect. However, the preliminary core survey did not confirm the presence of H1 layers in cores suitable for any other cross-margin transect.

Vertical spacing of samples in each core varied because of the different H1 layer thicknesses and inter-sample spacing ranges from 2–11 cm. The thicker H1 layers in cores from the Labrador slope and Grand Banks region were sampled at larger intervals, and the thinner H1 layers in cores from the Scotian margin were subsampled at smaller intervals. At least one sample above and one sample below the H1 layer were analysed

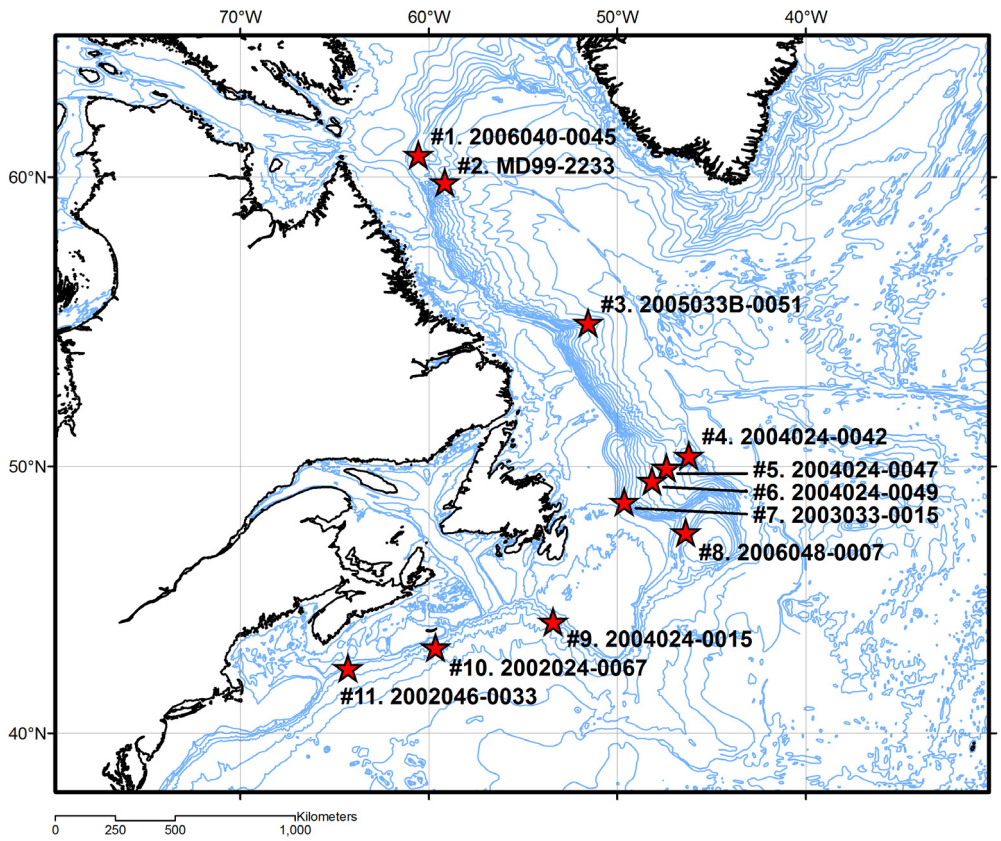

Figure 3.2: Location of 11 cores with identified H1 layers chosen for grain size analysis and determination of calcium carbonate and sand-gravel content. Two transects are available to investigate variability: a proximal to distal along-margin transect of 8 cores and a cross-margin transect of 4 cores in Orphan Basin.

Table 3.1: Cores chosen for grain size analysis and determination of calcium carbonate and sand-gravel content.

#	Core ID	Core Location	Water Depth (m)	Along-Margin Distance (km)	H1 Layer Depth (cm)	H1 Layer Thickness (cm)	# of Samples	Resolution (cm/sample)	Reference
1	2006040-0045pc	60.726°N 60.552°W	1589	200	390–565	175	18	11	GSC-Atlantic
2	MD99-2233pc	59.824°N 59.156°W	2350	300	50–203	153	18	10	*Rashid et al.* [2003b], *Rashid and Piper* [2007], *Tripsanas and Piper* [2008]
3	2005033B-0051pc	55.072°N 51.546°W	2740	1000	512–537	25	16	2	GSC-Atlantic
4	2004024-0042pc	50.378°N 46.211°W	1875	1700	30–54	22	14	2	GSC-Atlantic
5	2004024-0047pc	49.951°N 47.400°W	2691	1700	81–104	23	15	2	*Tripsanas et al.* [2007], *Tripsanas and Piper* [2008]
6	2004024-0049pc	49.476°N 48.164°W	2322	1700	333–360	27	14	3	*Tripsanas et al.* [2007], *Tripsanas and Piper* [2008]
7	2003033-0015pc	48.710°N 49.641°W	818	1700	113–143	30	15	3	*Tripsanas et al.* [2007]
8	2006048-0007pc	47.586°N 46.375°W	1134	1900	146–198	52	18	4	GSC-Atlantic
9	2004024-0015pc	44.266°N 53.413°W	1045	2900	582–600	18	12	2	*Piper et al.* [2006]
10	2002046-0067pc	43.288°N 59.643°W	2564	3500	765–772	7	8	2	*Jenner et al.* [2007]
11	2002046-0033pc	42.508°N 64.289°W	1270	3900	205-210	5	6	2	*Hundert and Piper* [2008]

to characterise background sedimentation. A total of 154 samples were taken, and the number of samples in a core ranged from 6–18. Core photography and X-radiographs were used to guide sampling and interpretation of results, especially in proximal H1 layers.

The disaggregated inorganic grain size (DIGS) of each sample was determined with a Beckman Coulter Counter Multi-sizer III (MS3) using a procedure similar to that described in *Milligan and Kranck* [1991]. In preparation for analysis, samples were dried in an oven at 40°C and organic matter was digested with 30% H_2O_2 solution that was subsequently evaporated from the sample on a hot plate. Digested samples were resuspended in 0.45 μm filtered 1% NaCl and sonified using a sapphire-tipped ultrasonic probe immediately before analysis to disaggregate component grains. Coulter Counters draw sample in electrolyte solution through an aperture across which a constant current is maintained. When a particle flows through the aperture, it results in an increased electrical resistance that causes a spike in voltage that is proportional to particle volume. The ability of a Coulter Counter to resolve particles of a particular size is dependent on the aperture size through which the sample solution passes. The MS3 effectively resolves particles with diameters between 2–50% of the apertures used. Samples were run using two tubes with aperture sizes of 30 and 200 μm, which were able to resolve particle of diameters 0.6–100 μm. To prevent large grains from clogging the aperture, sample solutions were screened at 100 μm prior to analysis with the 200 μm tube and then at 25 μm prior to analysis with the 30 μm tube. The MS3 outputs particle counts for each tube in 256 bins in 1/50ϕ increments. Using a Matlab routine, the particle counts were summed across 10 bins and re-binned in 1/5ϕ increments using the midpoint diameter. Bins with counts below 10 were discarded and each tube distribution was normalized to produce a single distribution curve for each sample.

3.4 Calcium Carbonate

Prior to H_2O_2 digestion, a portion of each dried sample was ground with a mortar and pestal, weighed, and analysed for total inorganic carbon content using a UIC Inc. CM5130 acidification module and CM5014 coulometer. The coulometer essentially performs an

automated titration of the CO_2 liberated from a sample digested in the acidification module. 2N H_2SO_4 is added to ~20 mg dried and ground sample and heated in the acidification unit. The CO_2 liberated is carried into the coulometric cell containing a solution of monoethanolamine and a colorimetric pH indicator. Platinum (cathode) and silver (anode) electrodes are placed in the cell creating a circuit. When CO_2 enters the cell it reacts to form a titratable acid that causes the colour of the pH indicator to fade. The cell is located between a light source and a photodetector, and the reaction is monitored by change in percent transmittance. As the percent transmittance increases, a titration current is activated to create base at a proportionate rate. The endpoint is reached at full transmittance. The total amount of current required for the titration is integrated and yields a mass of total inorganic carbon with detection limits of 0.01 μg and 100 mg. Calcium carbonate ($CaCO_3$) content was calculated using the carbon mass and assuming no other carbonate-bearing species was present. Analytical precision and accuracy were calculated each time the instrument was run using pure $CaCO_3$ and NRC MESS-3 marine sediment standards and were never found to be greater than $\pm$1.0% and $\pm$1.8% respectively.

3.5 Sand & Gravel

A portion of each digested sample was suspended in a filtered 1% NaCl solution and divided into a fine (<63 μm) and coarse (>63 μm) fraction by screening. Both fractions were filtered through a pre-weighed millipore 8.0 μm filter under vacuum. The use of this size filter is recommended in previous studies [e.g., *Sheldon et al.*, 1972; *Law et al.*, 2008], because it has much smaller nominal pore sizes once filtering begins but is not as prone to clogging. The filters and collected grains were dried and weighed. The fraction weights were added for a total sample weight that was then used to calculate % sand-gravel for each sample. In an open-ocean setting, % sand-gravel would be equivalent to % IRD since ice-rafting is the only process that can account for delivery of coarse grains to the seafloor. However, in a slope setting, turbidites also deliver a significant portion of coarse grains to the seafloor. Thus, % sand-gravel in a sample represents the portion of the sample not delivered by plume but by ice-rafting and/or turbidites.

3.6 Inverse Floc Model

All DIGS distributions were analysed with an inverse floc model in attempt to identify any deposition associated with a meltwater plume. The model was developed by *Curran et al.* [2004] based on previous work by *Milligan and Kranck* [1991], *Kranck et al.* [1996], and *Curran et al.* [2002]. As Fig. 3.3 illustrates, the model assumes that sediment of a particular component grain size may exist in three different reservoirs: as suspended single grains, as suspended flocs, and as bed deposit. Grains are transferred between the single and flocculated reservoirs through aggregation and disaggregation processes. Deposition of grains to the bed deposit reservoir occurs from both suspended reservoirs, but sediment resuspension is assumed insignificant.

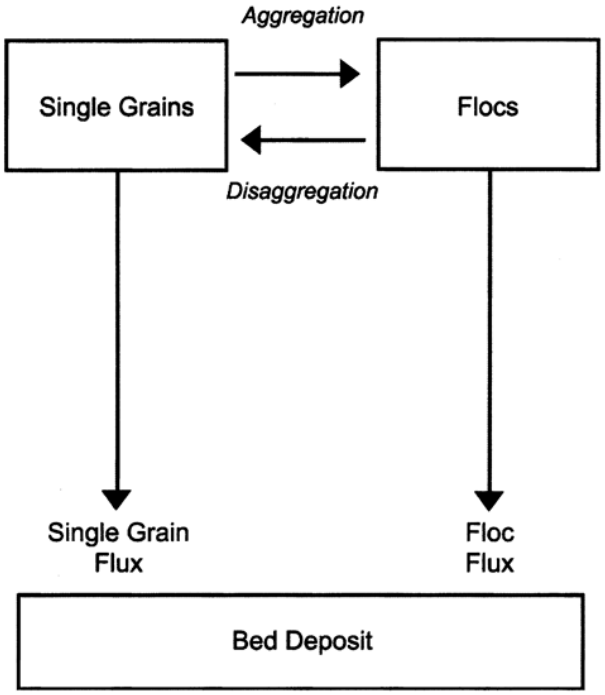

Figure 3.3: Conceptual basis for the inverse floc model outlining the behaviour of suspended fine sediment and its relationship to bottom deposits.

The model uses a non-linear fit of DIGS distributions to the modelled equation for total flux to the seabed. Four parameters describe the observed DIGS distributions in the bottom sediment:

source slope, m Graphically, this is the slope of the distribution, on a log-log plot of concentration vs. diameter, of the smallest diameters (see Fig. 3.4). It is a property of the parent material from which the deposit is derived.

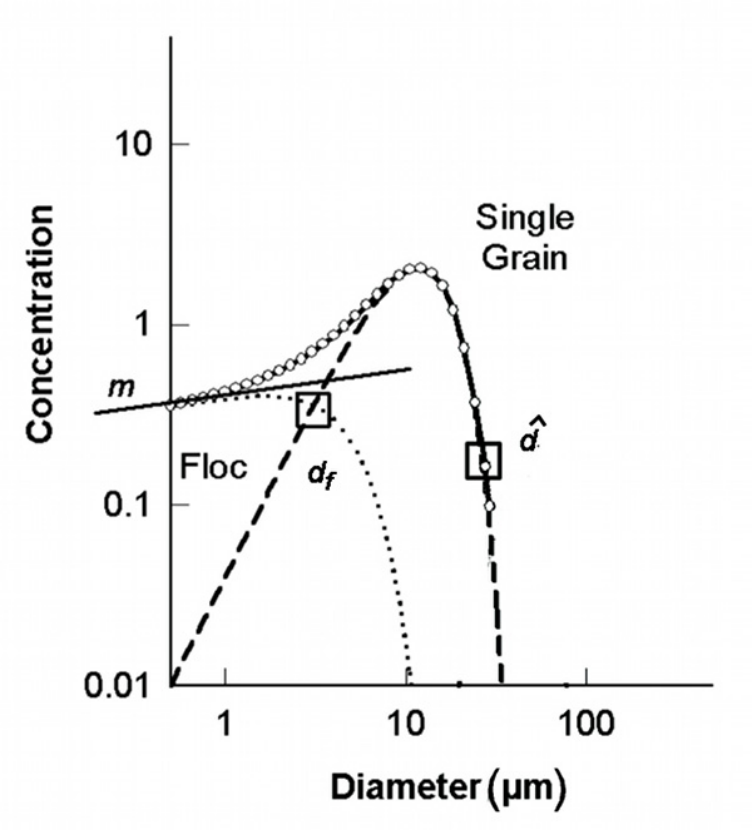

Figure 3.4: Idealized DIGS distribution (solid line) on log-log axes showing the floc component (dotted line) and single grain component (dashed line) determined by the inverse floc model. The graphical location of m, $\hat{d}$, and d_f on the distribution is identified.

falloff diameter, $\hat{d}$ The diameter of particles whose concentration has fallen to $1/e$ of its initial value in the source distribution (see Fig. 3.4). $\hat{d}$ can be thought of as the largest grain in suspension.

floc limit, d_f The diameter of particles whose flux to the seabed as single grains and in flocs is equal (see Fig. 3.4). For grain sizes greater than d_f, single grain deposition dominates while floc deposition dominates for grain sizes less than d_f.

floc fraction in the seabed, K_f The mass fraction of grains deposited in flocs on the seabed, equal to the area under the "floc" curve divided by the area under the total distribution.

3.6.1 Formulation

The distribution of a fine sediment suspension can be written as

$$C(i) = Q\left(\frac{d_i}{d_0}\right)^m \exp^{-\left(\frac{d_i}{\hat{d}}\right)^2}, \tag{3.1}$$

where $C(i)$ is mass concentration of suspended sediment in the ith size class, Q is the mass concentration of the reference diameter d_0, d_i is the diameter of class i, m is the source slope of the parent material, and $\hat{d}$ is the diameter of particles whose concentration has fallen below $1/e$ of the initial concentration in the source distribution. The suspended sediment in each size class can exist as single grains or flocs

$$C_s(i) = C(i)(1 - f), \tag{3.2}$$

and

$$C_f(i) = C(i)f, \tag{3.3}$$

where $C_s(i)$ and $C_f(i)$ are mass concentration in the ith size class of single grains and flocs respectively, and f is the mass fraction bound in flocs, or the "floc fraction" in suspension. By multiplying the concentration by a settling velocity, the flux of suspended sediment in size class i to the seabed as single grains, $Z_s(i)$, and within flocs, $Z_f(i)$, can be written as

$$Z_s(i) = w_s(i)C(i)(1 - f), \tag{3.4}$$

and

$$Z_f(i) = w_f C(i) f. \tag{3.5}$$

Here, $w_s(i)$ is the settling velocity of single grains in class i, and w_f is the settling velocity of flocs. Notice that a constant settling velocity is used for all flocs, which is justified by observed mean floc settling velocities of approximately 1 mm/s in a variety of environments [e.g., *Hill et al.*, 1998]. The sum of Eq. 3.4 and Eq. 3.5 is the total flux, $Z(i)$, to the the seabed

$$Z(i) = w_s(i)C(i)(1-f) + w_f C(i) f. \tag{3.6}$$

After simplifying and substituting Eq. 3.1, Eq. 3.6 becomes

$$Z(i) = \Big(w_s(i)(1-f) + w_f f\Big) Q \left(\frac{d_i}{d_0}\right)^m \exp^{-\left(\frac{d_i}{\bar{d}}\right)^2}. \tag{3.7}$$

If a threshold grain size whose flux to the seabed as single grains and within flocs is equal is defined as the floc limit, d_f, then Eq. 3.4 and Eq. 3.5 can be equated and simplified using d_f as follows:

$$\frac{w_s(d_f)}{w_f} = \frac{f}{1-f} \tag{3.8}$$

Stokes' law can be applied to settling grains to approximate w_s, so d_f can be written as

$$d_f = \sqrt{\frac{w_f f 18\mu}{(1-f)(\rho_s - \rho)g}} \tag{3.9}$$

where μ is the dynamic viscosity of seawater, ρ_s is the density of the sediment, ρ is the density of seawater, and g is the acceleration due to gravity. w_f is assumed to be constant for mature flocs. $w_s(d_f)$ can be written in terms of $w_s(i)$ as

$$w_s(d_f) = w_s(i) \left(\frac{d_f}{d_i}\right)^2 \tag{3.10}$$

Substituting Eq. 3.10 into Eq. 3.8 yields

$$w_s(i) = w_f \left(\frac{d_f}{d_i}\right)^2 \left(\frac{f}{1-f}\right) \tag{3.11}$$

Substituting Eq. 3.11 into Eq. 3.7, the total flux to the seabed is then

$$Z(i) = B\left(\frac{d_i}{d_0}\right)^m \exp^{-\left(\frac{d_i}{d}\right)^2}\left(1+\left(\frac{d_i}{d_f}\right)^2\right), \tag{3.12}$$

where B is the flux of grains of reference size d_0 to the seabed within flocs. The mass fraction of sediment delivered to the seabed in flocs, K_f, is the sum of $Z_f(i)$ for all size classes divided by the total mass flux to the seabed

$$K_f = \frac{\sum_{i=1}^{N} C(i)}{\sum_{i=1}^{n}\left(1+\left(\frac{d_i}{d_f}\right)^2\right)C(i)}, \tag{3.13}$$

where N is the number of size classes used.

3.7 Entropy Analysis

Entropy analysis was used to investigate DIGS distribution variability. In information theory, entropy is a measure of the randomness associated with a variable and was first described by *Shannon* [1948]. In essence, entropy describes the information content, since the value of a measured variable decreases with increasing randomness. Applied to particle size distributions, entropy is greatest and randomness is at a maximum when particles are evenly distributed between all size classes. On the other hand, entropy is least and there is no randomness in a distribution when all particles are found in one size class. In this way, entropy can be used to describe particle size distributions. Because the entire size spectrum is taken into consideration, entropy analysis provides insight not available through more traditional particle size spectra descriptors such as mean particle diameter and standard deviation [e.g. *Hill et al.*, 2000]. *Johnston and Semple* [1983] used a FORTRAN routine to apply the information theory of *Shannon* [1948] to sediment size which was later adapted to a QBASIC routine by *Woolfe and Michibayashi* [1995] who showed that entropy analysis of bottom sediment size distributions provided groupings that could be correlated to depositional environment. Since, many more researchers have confirmed that entropy groupings can be meaningfully associated with sediment facies. More recently, *Orpin and Kostylev* [2006] used entropy analysis to characterise bottom sediment texture on the Scotian Shelf and define ecological habitats, while *Mikkelsen et al.* [2007]

used entropy analysis to investigate the role of turbulence variation on floc formation. An adaptation of the entropy analysis routine of *Mikkelsen et al*. [2007] was used to group the core sample DIGS distributions in this study. This routine is a Matlab translation of the QBASIC routine used by *Woolfe and Michibayashi* [1995]. DIGS spectra are divided into three groups with a R_s value of 66.0% (See Section 3.7.1 for definition of R_s). The optimum number of groups was determined to be 13 with a R_s value of 88.3%. However, three groups explain a majority of the variability and provide distinct groups that can be associated with the sediment facies observed in the H layers.

3.7.1 Formulation

For a particle size distribution with n size classes, the entropy, E, is given by

$$E = -\sum_{i=1}^{n} p_i \log p_i, \tag{3.14}$$

where p_i is the proportion of particles in size class i [*Shannon*, 1948; *Johnston and Semple*, 1983]. Entropy can be related to information gain or inequality statistic, I, by

$$I = (\log n) - E. \tag{3.15}$$

This reflects the concept that as entropy decreases and volume within a spectrum is concentrated into fewer size classes, the spectrum becomes more informative in regards to particle processes and depositional environment.

Sample DIGS distributions are grouped using the inequality statistic by maximizing the inequality between groups and minimizing the inequality within groups. In order to do this, the volume of particles in each size class in each spectrum must be expressed as proportions of the total volume of all size classes in all spectra [*Johnston and Semple*, 1983]. Following *Mikkelsen et al*. [2007], the proportion of the total volume concentration in spectrum j, size class i is Y_{ij} and is defined as

$$Y_{ij} = \frac{VC_{ij}}{\sum_{j=1}^{J} \sum_{i=1}^{N} VC_{ij}}, \tag{3.16}$$

where N is the total number of size classes in each spectrum, J is the total number of spectra, VC_{ij} is the volume concentration in spectrum j, size class i. The total inequality for all spectra is then given by

$$I = \sum_{i=1}^{N} Y_i \sum_{j=1}^{J} Y_j \log N Y_j, \tag{3.17}$$

where $Y_i = \sum_{j=1}^{J} Y_{ij}$ and $Y_j = \frac{Y_{ij}}{Y_i}$.

The percentage of the inequality in the spectra explained by the grouping is the R_s statistic [*Johnston and Semple*, 1983]

$$R_s = \left(\frac{I_B}{I}\right) 100, \tag{3.18}$$

where I_B is the inequality between groups defined as [*Mikkelsen et al.*, 2007]

$$I_B = \sum_{i=1}^{N} Y_i \sum_{j=r}^{R} p_{ir} \log \left(\frac{p_{ir}}{J_r/J}\right), \tag{3.19}$$

where $p_{ir} = (\sum_{j \in r} Y_{ij})/Y_i$ and J_r is the number of spectra in group r of R total groups. To obtain an optimal grouping defined as the best R_s statistic, it is necessary to perform calculations for all the possible combinations of J into R groups for each R and use the combination with the greatest R_s. Similarly, to obtain the optimal number of groups, the optimal grouping must be determined for r of R groups then for $r + 1$ groups, and the resulting R_s statistics are compared to assess validity of the groupings. The routine ends when increasing the number of groupings fails to increase the R_s statistic.

CHAPTER 4

RESULTS

The H1 layer thicknesses obtained from the survey of post-1999 cores are presented in the following sections along with results from the 11 cores chosen for grain size analysis and determination of carbonate and sand-gravel content. The presentation of results focuses on spatial (between layer) and temporal (within layer) variability in the H1 layers of the study region. Spatially, results are presented along- and cross-margin to show variability with distance along and across the path of sediment transport. Temporally, results are presented by layer fraction (in 10% increments) to allow comparison between layers of different thicknesses. By doing this, a constant sedimentation rate within each core for the event duration is implicitly assumed. A summary of the analyses made in each core can be found in Appendix A.

4.1 H1 Layer Thickness

The thickness of the H1 layers in 104 cores from the study region are shown in Fig. 4.1 and range from 2–175 cm. H1 layer thickness is plotted by along-margin distance in Fig. 4.2 to investigate the change in sedimentation rate with distance from the source. An exponential function (displayed on the plot) is fitted to the thickness data with a R^2 of 0.69. This trend supports a single source of sediment delivery to the Labrador Sea during the H1 event from the Hudson Strait region. Much of the Labrador Slope (700–1000 km) contains cores with H1 layers that are thinner than predicted by the exponential relationship, while the Orphan Basin and Flemish Pass regions (1700–2200 km) contain

cores with H1 layers that are generally thicker than predicted. H1 layer thickness is plotted by water depth for cores with the same along-margin distance in Fig. 4.3. No apparent trend in H1 layer thickness with water depth can be discerned at any distance from the Hudson Strait. The lack of a cross-margin trend in thickness negates significant cross-margin transport (i.e., resulting from meltwater discharged at various points along the margin or mass transport events after deposition).

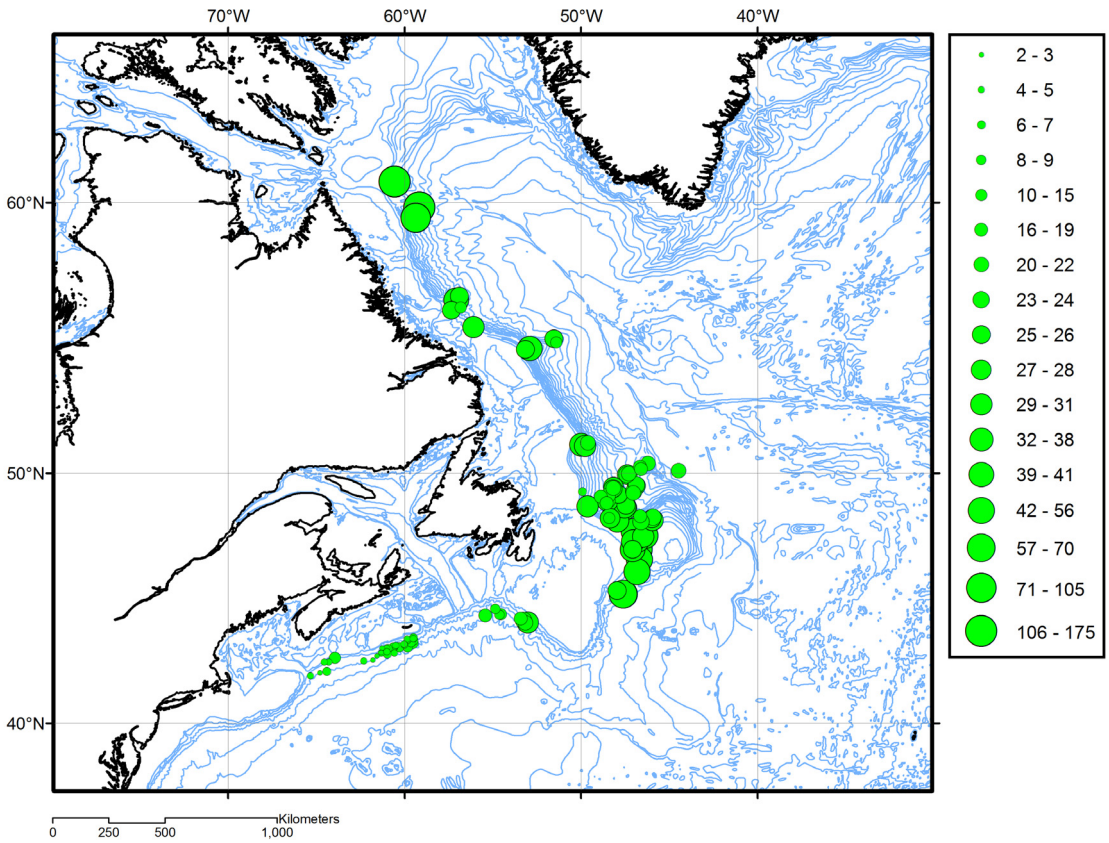

Figure 4.1: H1 layer thickness (cm) in 104 cores from the western North Atlantic. The size of the core location marker indicates layer thickness.

4.2 DIGS Entropy Analysis

All DIGS distributions were divided into three groups using entropy analysis. Fig. 4.4(a) shows all core sample spectra together and in their assigned groups with the average group spectra shown in black. Fig. 4.4(b) shows the average group spectra for all three groups on the same axes, and Fig. 4.4(c) shows the median diameter of each sample

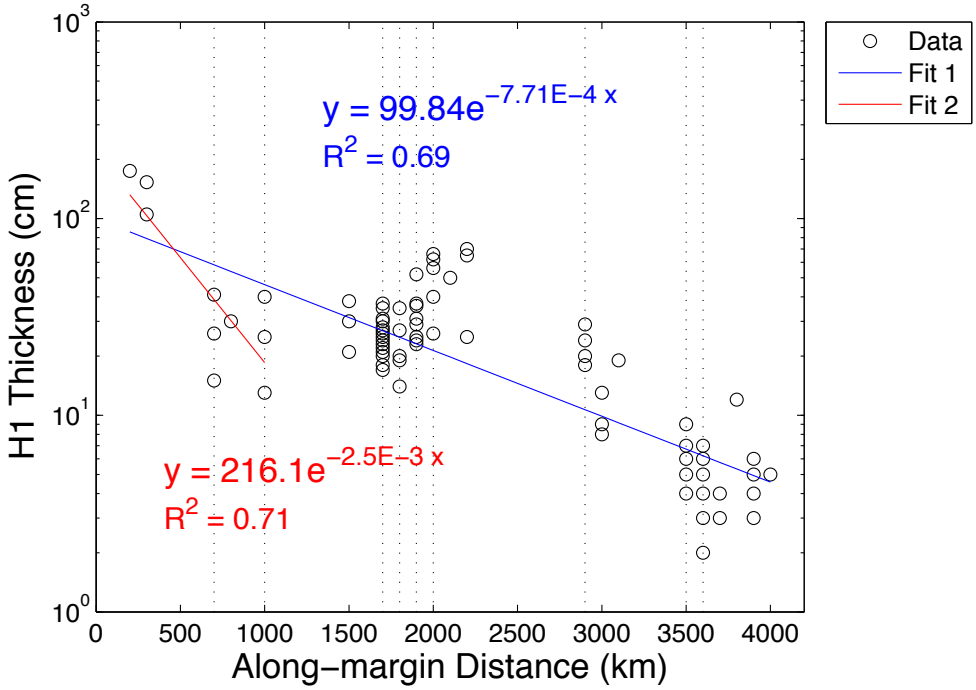

Figure 4.2: H1 layer thickness (cm) by along-margin distance (km) on semilog-y axes for 104 cores from the western North Atlantic. Fit 1 is a linear regression of all recorded layer thicknesses and is shown in blue with the equation and R^2 value. Fit 2 is a linear regression of layer thicknesses in cores only within 1000 km of Hudson Strait and is shown in red with the equation and R^2 value. Dotted vertical lines mark along-margin distances used in Fig. 4.3 to examine cross-margin variation in H1 layer thickness.

distribution coloured by group. Group #1 has the greatest volume of fine grains and the smallest median diameter, group #3 has the greatest volume of coarser grains and the largest median diameter, and group #2 has an intermediate median diameter and contains the majority of its volume at these intermediate sizes.

The group # assigned to each core sample DIGS distribution is presented downcore in Fig. 4.5. The number of samples in each core varies from 6–18 generally decreasing with distance from the source and is a good indicator of relative thickness of the H layer. Histograms in Fig. 4.5 show the number of occurrences of each group in all cores, by layer fraction, by cores in the along-margin transect, and by cores in the cross-margin transect.

Occurrences of group #1 range from 0–14 per core. In general, the occurrence of group #1 decreases with distance from the source along-margin and is completely absent in some distal cores. The number of occurrences of group #2 with along-margin distance is

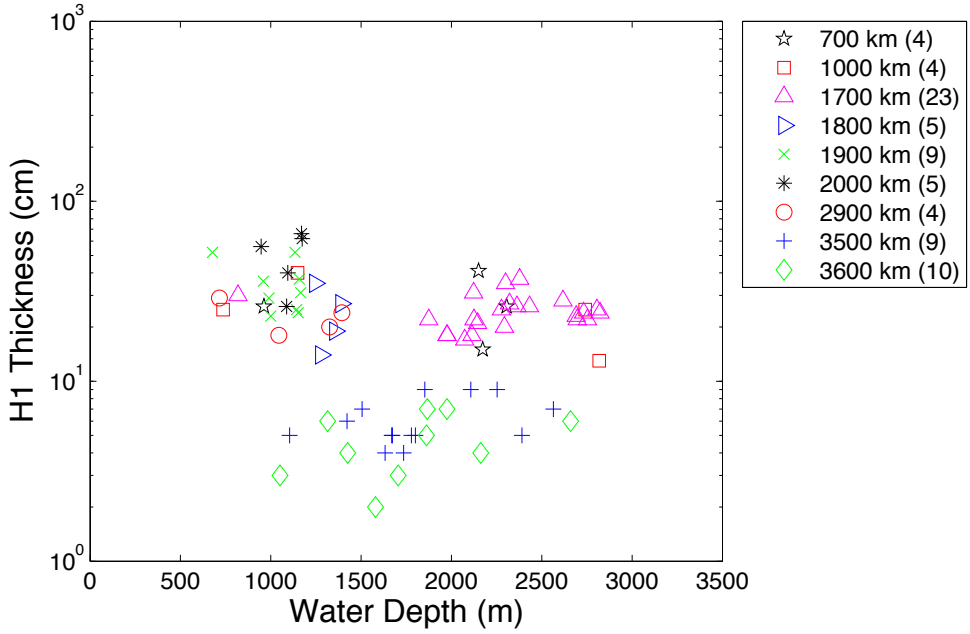

Figure 4.3: H1 layer thickness (cm) by cross-margin distance (km) on semilog-y axes for groups of cores from the western North Atlantic with the same along-margin distance. Layers within cores at 9 different along-margin distances are plotted with the total amount of cores at each along-margin distance indicated in parenthesis on the legend.

between 4 and 12 per core and fairly constant, although the total number of samples per core is decreasing. Occurrences of group #2 increase slightly with along-margin distance until the Flemish Pass region (core #8) is reached where they are highest at 12 occurrences and decrease slightly thereafter. The occurrence of group #3 is sporadic ranging from 0–5 occurrences per core and does not show any obvious along-margin evolution. The number of occurrences of group #1 is directly related to layer thickness.

In terms of cross-margin variability, the occurrence of group #1 ranges from 2–6 and decreases with seaward distance. Occurrences of group #2 range from 8–10 per core and group #3 occurrences range from 1–4 per core. There is no significant trend in the occurrence of group #2 cross-margin and occurrences of group #3 increase with seaward distance cross-margin.

Temporally, a total of 2–9 occurrences of group #1 in each layer fraction, 5–10 occurrences of group #2 in each layer fraction, and 1–9 occurrences of group #3 in each layer fraction were counted within cores. The occurrence of group #1 comprises the majority in core samples at the start of the H1 event and decreases as the event proceeds while

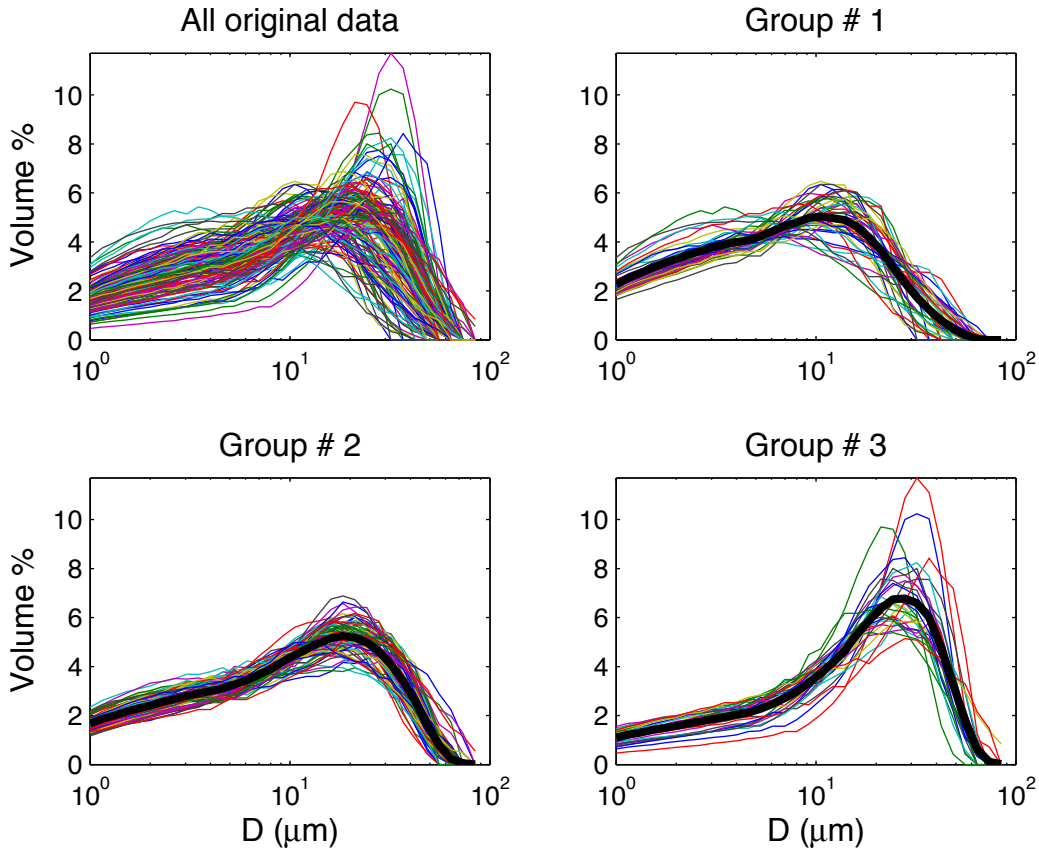

(a) Grouped sample DIGS spectra.

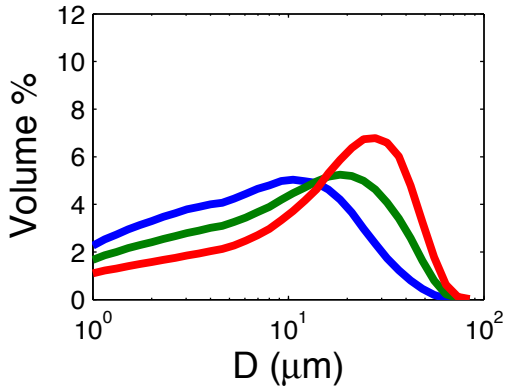

(b) Average group spectra.

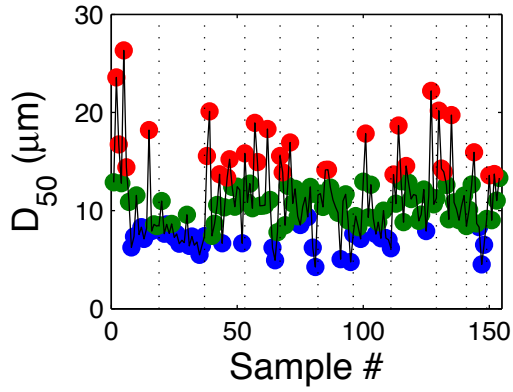

(c) D_{50} of grouped samples.

Figure 4.4: Entropy analysis of sample DIGS distributions (¡100 μm fraction) showing (a) all core sample spectra together and in their assigned groups with the average group spectra shown in black (b) the average group spectra for all three groups on the same axes (c) the median diameter of each sample spectra colored by group. Axes are semilog-x in (a) and (b). In (b) and (c) group #1 is shown in blue, group #2 is shown in green, and group #3 is shown in red.

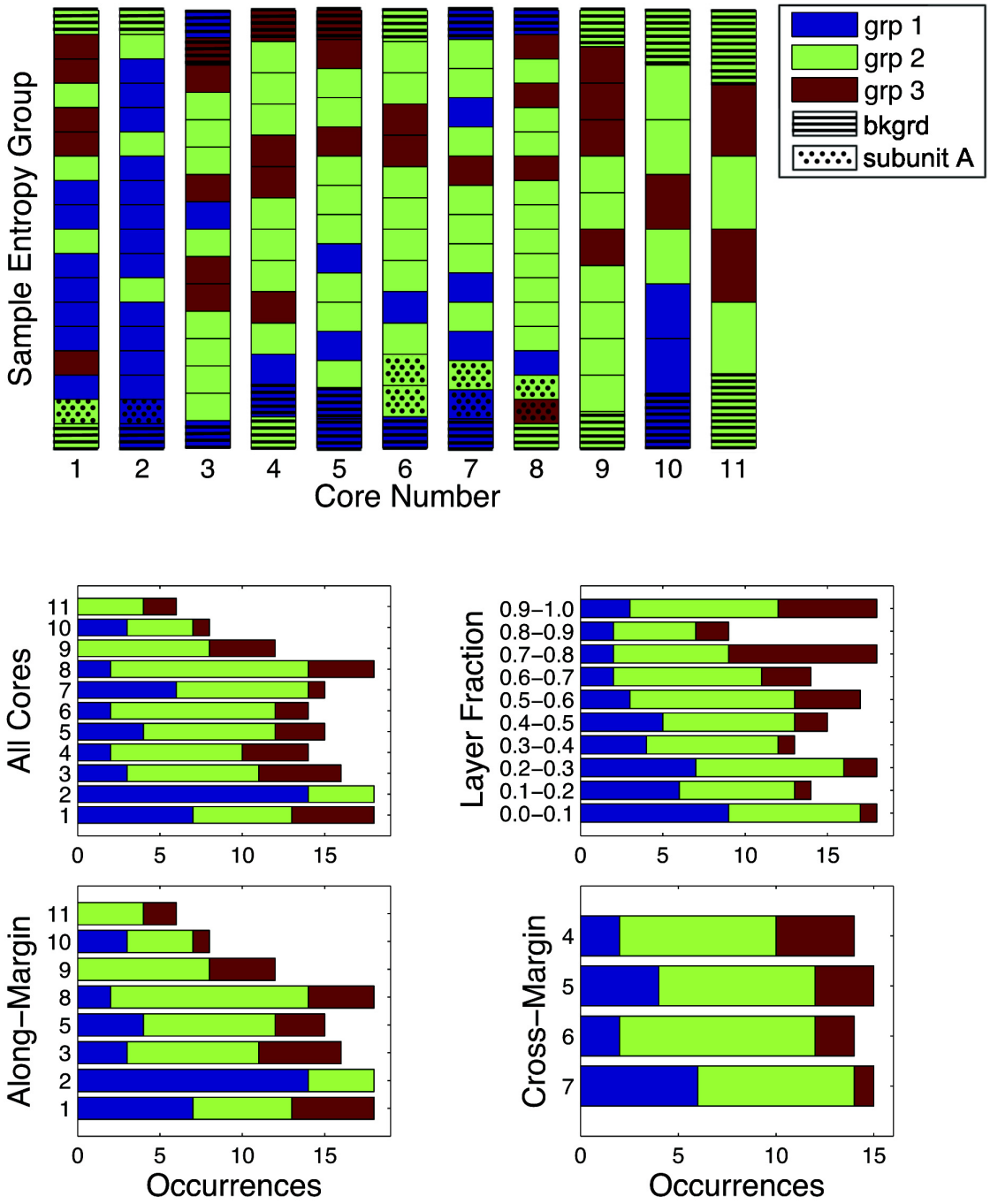

Figure 4.5: The entropy group # of each sample DIGS distribution is shown through each core. Samples just outside the H1 layer (background) and samples in subunit A are marked by horizontal lines and stipples. Cores are presented from left to right in order of increasing along-margin distance. Histograms show the number of occurrences of each group in all cores, by layer fraction, by cores in the along-margin transect, and by cores in the cross-margin transect.

the occurrence of group #3 increases during the event to comprise a significant portion of samples at the end of the event. The occurrence of group #2 is fairly constant through the duration of the event.

4.3 Calcium Carbonate and Sand-Gravel Content

Along-margin, cross-margin, and temporal (downcore) variability in the $CaCO_3$ and sand-gravel content of the core samples are shown by boxplots in Fig. 4.6, Fig. 4.7, and Fig. 4.8 respectively. Both $CaCO_3$ and sand-gravel content are expressed as percents by mass.

The median $CaCO_3$ content within the H1 layers decreases from 47–13% with distance from the source. Lowest median % sand-gravel is recorded proximally at 8%. The sand-gravel content increases initially and then decreases, peaking with a median value of 25% in the Orphan Basin (core #5) and of 27% in the Grand Banks (core #9) regions. Cross-margin, the median % $CaCO_3$ is between 28–35% and the median % sand-gravel ranges between 21% and 27%. Both % $CaCO_3$ and % sand-gravel have smaller ranges of values cross-margin than along-margin and both have maxima at core #6. Core #7 is a particularly shallow core and appears to have the most unique values in the cross-margin transect.

At the start of the event, the $CaCO_3$ content quickly increases from a median value of 10% to a maximum at 41% (layer fraction 0.2-0.3 bin). Then, % $CaCO_3$ slowly decreases for the duration of the event but does not return to pre-H1 levels. The % sand-gravel in the core samples shows a similar trend although less pronounced with medians ranging from 11–25%.

4.4 Inverse Model Parameters

Along-margin, cross-margin, and temporal variability in model parameters m, $\hat{d}$ (μm), d_f (μm), and K_f for the DIGS distributions of the core samples are shown in Fig. 4.6, Fig. 4.7, and Fig. 4.8 respectively.

There is no clear along-margin trend in source slope, m. Median values of m range from 0.35–0.52. The highest m values are recorded proximally (core #1) and in the Orphan Basin (core #5) and Grand Banks (core #9) regions. Median values of falloff diameter, $\hat{d}$, are between 22 μm and 34 μm and median values of floc limit, d_f, are between 37

μm and 56 μm. Both $\hat{d}$ and d_f increase slightly with distance from the source. The mass fraction of flocs deposited, K_f, remains constant around 0.9 and shows no along-margin evolution.

Cross-margin, median values of m initially increase and then decrease peaking in the middle of the transect at 0.52 (core #5). Median values of $\hat{d}$ are constant around 30 μm cross-margin. Median values of d_f are also constant around 49 μm except for the higher value of 56 μm in core # 7. K_f, remains constant around 0.9 and shows no cross-margin evolution. Core #7 is a particularly shallow core and appears to have the most unique values in the cross-margin transect.

Temporally, m median values increase from 0.25 at the beginning of the event reaching maximum values of 0.56 at the layer fraction 0.7-0.8 bin after which values decrease. Median m values at the end of the event are much higher in comparison with values from the start of the event. The median values of $\hat{d}$ ranges from 28–32 μm and shows no temporal evolution. The medians of d_f, and K_f are constant with time at 49 μm (except 42 in bin 0.3–0.4) and 0.9 each.

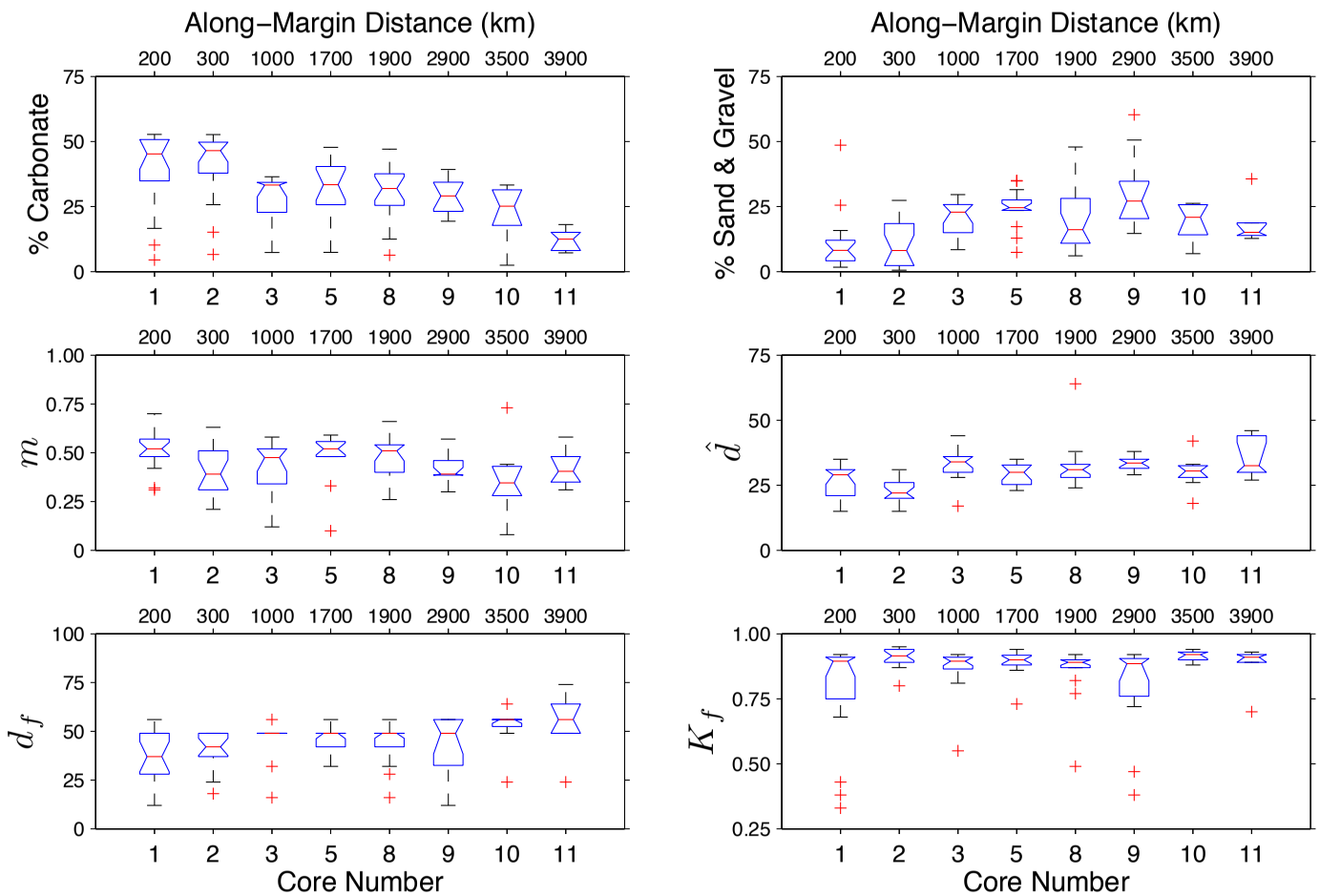

Figure 4.6: Variability of % carbonate, % sand & gravel, and model parameters m, $\hat{d}$ (μm), d_f (μm), K_f in cores of the along-margin transect. The box extends from the lower quartile to upper quartile and the median is shown in red. Whiskers extend to 1.5 times the interquartile range and outliers are displayed with a red '+'. The width of a notch is calculated so that box plots whose notches do not overlap have different medians at the 5% significance level.

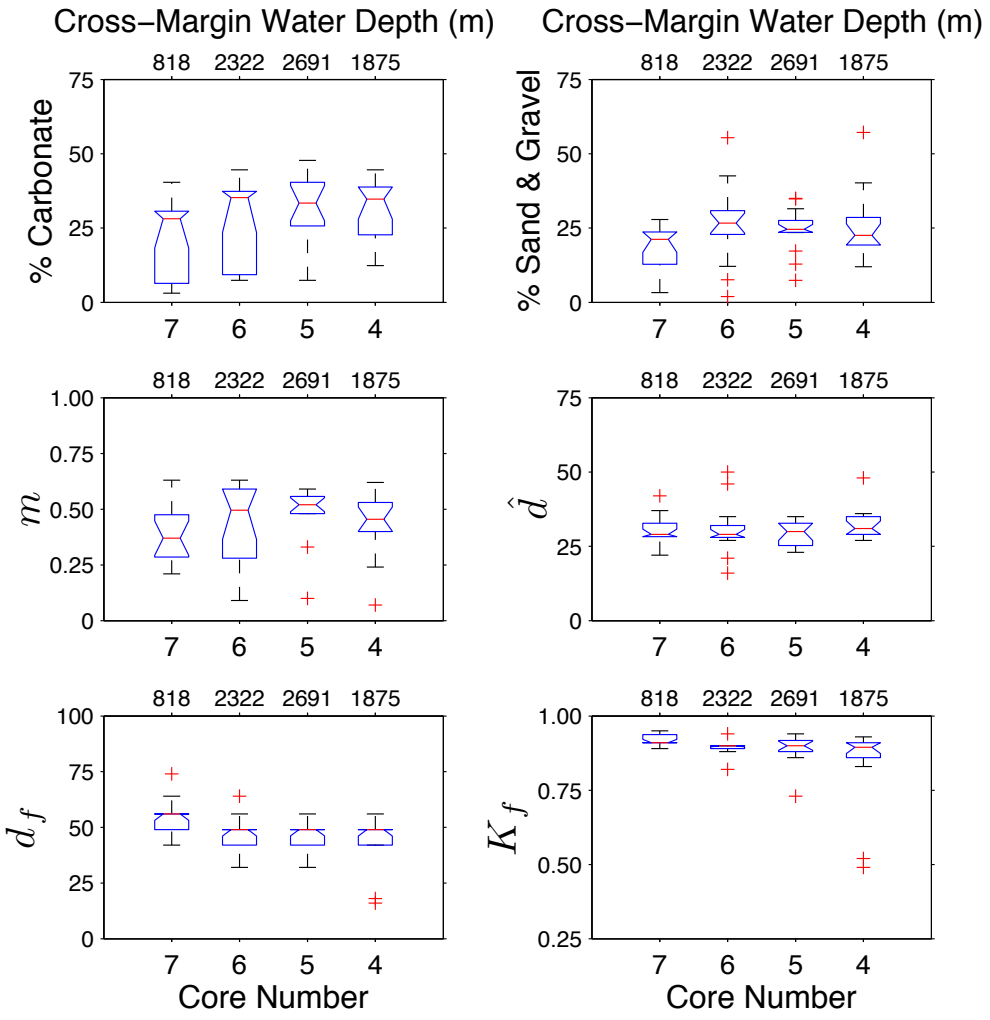

Figure 4.7: Variability of % carbonate, % sand & gravel, and model parameters m, $\hat{d}$ (μm), d_f (μm), K_f in cores of the cross-margin transect. The box extends from the lower quartile to upper quartile and the median is shown in red. Whiskers extend to 1.5 times the interquartile range and outliers are displayed with a red '+'. The width of a notch is calculated so that box plots whose notches do not overlap have different medians at the 5% significance level.

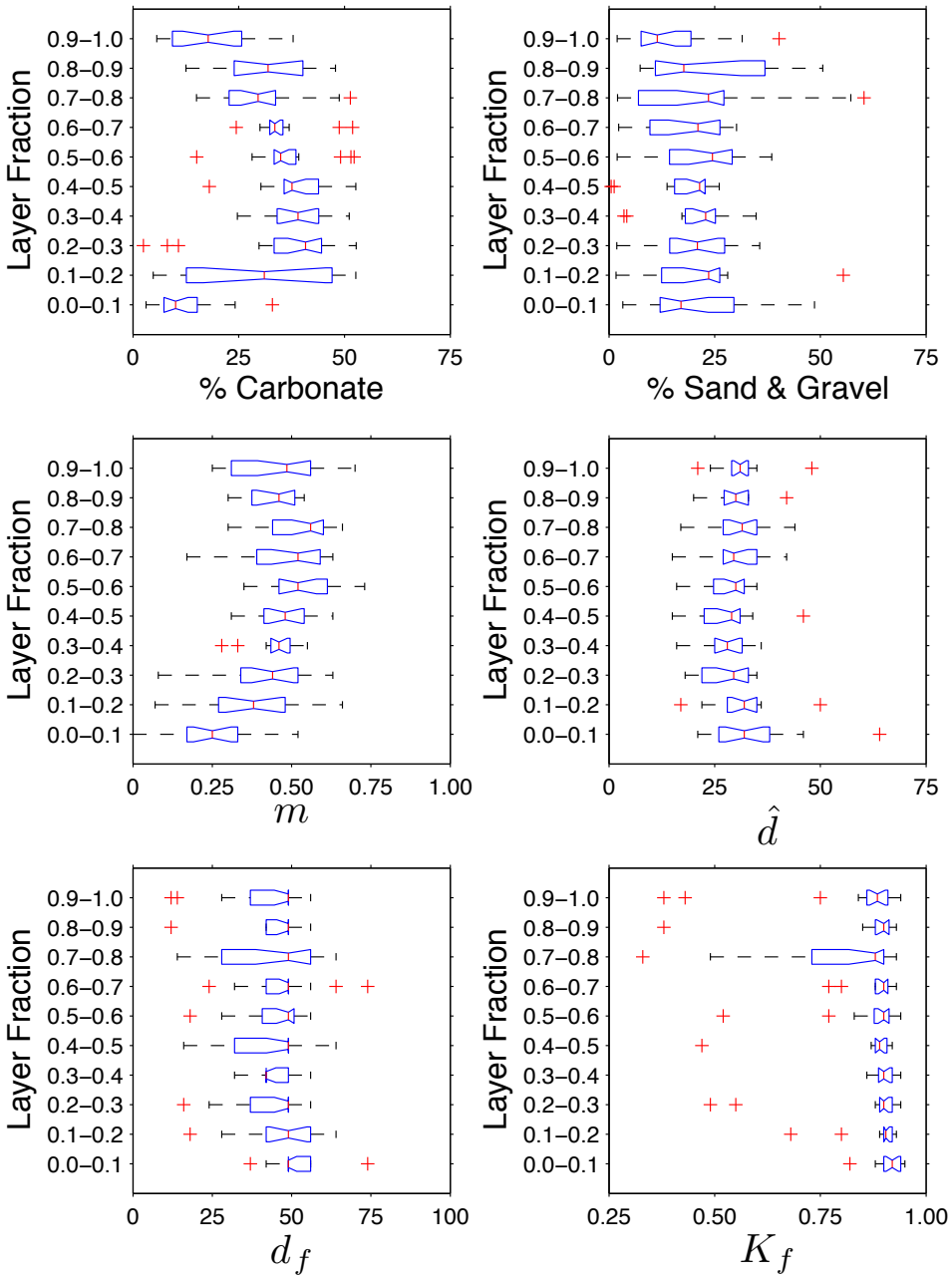

Figure 4.8: Variability of % carbonate, % sand & gravel, and model parameters m, $\hat{d}$ (μm), d_f (μm), K_f downcore. The box extends from the lower quartile to upper quartile and the median is shown in red. Whiskers extend to 1.5 times the interquartile range and outliers are displayed with a red '+'. The width of a notch is calculated so that box plots whose notches do not overlap have different medians at the 5% significance level.

CHAPTER 5

DISCUSSION

5.1 Association of Textural Groups with Delivery Mechanisms

Entropy analysis allowed all DIGS distributions to be divided into three textural groups. Each of these textural groups can be associated with a delivery mechanism necessary to produce that size distribution in bottom sediments. According to facies analysis [e.g., *Rashid et al.*, 2003b], three main delivery mechanisms are characteristic of the region during H events: plume fallout, ice-rafting, turbidity currents. Because the group #1 average spectrum is poorly sorted and has the largest volume-percent of the finest particles, it is most likely to result from flocculated plume-style deposition. Aggregation of grains into flocs is not sized-biased and floc deposition removes sediment in the same proportions it is found in suspension [*Kranck*, 1980]. *Milligan et al.* [2007] measured DIGS in the bottom sediments of the Po River Delta after a 100-year flood plume and found highly flocculated deposits that resemble the group #1 spectrum. The average distribution of group #3 has an abundance of well-sorted coarse particles that would result from significant single grain deposition characteristic of a higher energy sorting process. Similar distributions were found in turbidite sequences of cores on the Laurentian Fan [*Curran et al.*, 2004]. In the study region, turbidity currents are a common high energy sedimentological process [*Piper*, 2005] and high rates of sedimentation characteristic of H events may have increased the likelihood of turbidity current occurrence. Group #2 has more coarse particles and a lesser percentage of fine particles. Because this group shows little sign of sorting and contains a significant amount of coarser material, it is most likely associated with sediment delivery by ice-rafting. Fig. 5.1 shows the sand-gravel content

by weight for all samples in each entropy group, and as expected, group #2 and group #3 have the highest amounts. Alternatively, group #2 may be the product of bioturbation that caused mixing of grains between group #1 and group #3 type sediments, especially when considering the lower sedimentation rates in distal regions or near the event end. Although this possibility cannot be dismissed, it seems group #2 would have an intermediate sand-gravel content, which it does not, if it was a product of mixing.

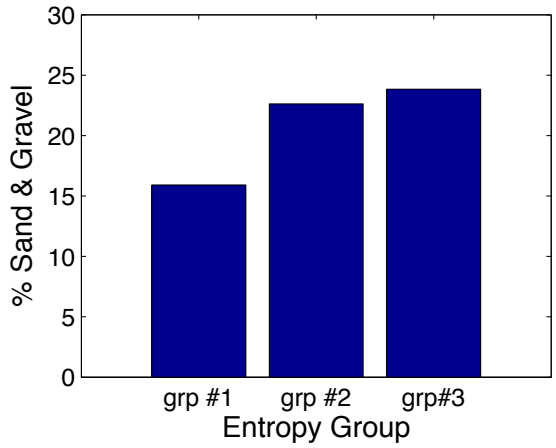

Figure 5.1: Sand-gravel content by weight for all samples in each entropy group.

5.2 Unfolding the H1 Event Using Sediment Texture

By investigating the downcore variance of entropy group in context of associated delivery mechanisms, a reconstruction of the H1 event begins to unfold that is supported by variability in H1 layer thickness, % $CaCO_3$, % sand & gravel, and inverse floc model parameters. Temporally, it is clear from Fig. 4.5 that group #1 dominates sediments deposited at the beginning of the H1 event. This implies that freshwater discharge was greatest at the beginning of the event. Spatially, the occurrence of group #1 is greatest proximally and significantly decreases with distance along the margin. This aligns with the expectation that the rate of plume-style sedimentation should decrease with distance from the source and lends support to the Hudson Strait region as the major source of meltwater discharge. Additionally, the decreasing cross-margin trend in the occurrence of group #1 suggests that more seaward cores are located below the edge of the plume trajectory as it moves southward while hugging the slope.

To address the feasibility of rapid plume deposition in the proximal region, a rough calculation can be performed to estimate the distance sediment would be carried by a typical coastal plume before deposition. The distance, x, particles with a settling velocity, w_s, will travel in a plume of thickness, h, with current speed, u, is $x = hu/w_s$. Consider a flocculated plume 100 m thick traveling 50 cm/s with a typical bulk settling velocity of 0.1 mm/s [*Hill et al.*, 2000; *Curran et al.*, 2002]. After traveling 500 km, sediment concentrations would have fallen to $1/e$ of their initial concentration, assuming no dilution by mixing. Cores #1 and #2 are both within 500 km of Hudson Strait and are the only cores that show significant plume deposition.

In Fig. 4.5, the occurrence of group #2 is relatively constant within cores suggesting that ice-rafting occurred throughout the H1 event and was steadily delivering sediment to the seafloor. Occurrences of group #2 are slightly elevated in the Orphan Basin (cores #4–7) and Flemish Pass (core #8) regions. Today, this is a region of complicated circulation where the Labrador Current encounters bathymetric and topographic barriers, and much of it is forced through the relatively narrow Flemish Pass. Additionally, it is near this region that the cold, south-flowing Labrador Current begins to mingle with the warmer, north-flowing Gulf Stream as it continues its north-eastward path across the North Atlantic Ocean. These conditions could have caused either a slowing of iceberg advection or increased melting rates in the region or a combination of both. Icebergs moving more slowly and/or melting more quickly would have delivered more sediment to the seafloor, explaining the increased occurrence of group #2 in the Orphan Basin and Flemish Pass region.

The occurrence of group #3 is indicative of high energy sorting events like turbidity currents and appears to be sporadic over distance and becomes more abundant over the course of the event as shown in Fig. 4.5. Turbidity currents can occur when sediment accumulates rapidly on slopes and is subsequently disturbed by physical forcing. Conditions for triggering turbidity currents would vary spatially due to local differences such as those in bathymetry, current, and sediment supply. As a result, turbidites may appear randomly over great areas when these local differences have not been considered. The occurrence of group #3 increases towards the end of the event, when large amounts of sediment previously deposited during the event may have contributed to slope instabilities resulting in turbidity currents. Furthermore, cross-margin variation shows an increase in group

#3 occurrence downslope and seaward that correlates with where turbidite deposits are expected to be found.

H1 layer thickness supports the H1 event scenario painted by the entropy grouping. The layer thickness within a particular core is the result of the overall sedimentation rate at that particular location. Based on the entropy groupings, three main sediment delivery mechanisms have been identified. Thus, the layer thickness is a result of the summation of all sedimentation from all three mechanisms during the event. With this in mind, support for the same trends evident from the entropy groupings can be found in the H1 layer thicknesses. H1 thicknesses are mapped in Fig. 4.1 and reveal that as distance from the source along the margin increases, the layer thickness decreases. This decreasing trend in layer thickness can be seen clearly in Fig. 4.2 where it has been fitted by an exponential function. However, it is obvious this decreasing trend is a result of distance from the source of the meltwater and icebergs, which are both triggers of turbidity currents, and does not offer information about the relative importance of each delivery mechanism. Focus on where and why the thickness varies from this exponentially decreasing trend provides more insight. The thickest H1 layers are found proximally and the entropy groupings indicate that much of this layer is composed of plume delivered sediments. All of the cores from the Labrador margin (400–1400 km) are thinner than expected from the exponential fit. This is likely because most sediment from the plume has been deposited more proximally, and this component of the total sedimentation has decreased without compensation from any other delivery mechanism. Layer thickness in cores from the Orphan Basin region (1500–1700 km) are well-fit by the exponential trend and reflect the relative increase in sediment delivery by ice-rafting, also evident from the entropy groupings. Layer thickness in cores from the Flemish Pass region (1800–2200 km) are generally higher than the exponential fit, which reflects the same increase in sediment delivery by ice-rafting as well as an increase in high energy sorting evident from entropy group #3 occurrences.

The slope of the exponential fit of the H1 layer thickness data (Fig. 4.2) can be used to estimate a bulk settling velocity. This exponential fit takes the form of $y = Ae^{bx}$ on linear axes or $y = bx + A_n$ on semilog-y axes. The slope of the regression, b, is equal to w_s/hu, where w_s is settling velocity, h is plume thickness, and u is plume velocity (see Section 2.4, Eq. 2.3). Assuming a plume thickness of 100 m and a current speed of 50 cm/s yields a settling velocity of 0.04 mm/s for all recorded H1 layers, which is

very low for plume sedimentation [*Hill et al.*, 2000]. This is likely the result of the dominant ice-rafting delivery of sediments for most of the region. Considering only the H1 layer thicknesses within 1000 km of Hudson Strait where plume sedimentation is most important, however, yields a much steeper slope of 2.5×10^{-6} shown in red on Fig. 4.2. Using this slope, a settling velocity of 0.13 mm/s is calculated that is in good agreement with bulk settling velocities observed in flocculated plumes [*Hill et al.*, 2000; *Curran et al.*, 2002].

The $CaCO_3$ content and sand-gravel content of each sample reflect similar trends in sediment delivery where both % $CaCO_3$ and % sand-gravel are relatively constant until core #9 and then decrease. The DC in H1 layers has a distinct source near the Hudson Strait region so any decrease in the sediment $CaCO_3$ content must be due to deposition or dilution. $CaCO_3$ is delivered to the seafloor by both plume and ice-rafting. The sand-gravel content in H1 layers is the coarse grains whose presence in slope cores can only be explained by ice-rafting or turbidity current delivery. The H1 layer comprises sediment from plume, ice-rafting and other background sources. A decrease in sediment delivery by plume or ice-rafting decreases overall $CaCO_3$ input relative to background sediment input. It follows that a change in the rate of plume delivery of sediment would change the $CaCO_3$ content of a core, a change in the rate of turbidity current delivery would change the sand-gravel content of a core, and a change in the rate of ice-rafting delivery would change both the $CaCO_3$ and sand-gravel content of a core. Along-margin, % $CaCO_3$ decreases with a marked decline between core #2 and #3 where plume deposition would have also decreased markedly. $CaCO_3$ levels remain relatively constant through the Orphan Basin and Flemish Pass regions as delivery by ice-rafting increases. The % sand-gravel increases through the proximal region as plume delivery becomes less important and reaches its maxima in the Orphan Basin and Grand Banks regions. Again, this reflects the increased ice-rafting delivery likely caused by stalled icebergs and/or increased iceberg melting as well as the complex sediment dynamics of the region that make turbidity currents more prominent. $CaCO_3$ and sand-gravel content decrease in distal cores #9–11. Cross-margin, both $CaCO_3$ and sand-gravel content increase slightly and then level off or slightly decrease as the main trajectory of the advected icebergs is crossed.

Because DC is unique to the Hudson Strait source region, carbonate content can be used to assess the degree of dilution by non-Hudson Strait materials. Then, layer thickness can

be adjusted to reflect this dilution and regress the normalized thicknesses to obtain another estimate of bulk settling velocity. Fig. 5.2 shows 11 H1 layer thicknesses normalized to median carbonate content for each core. The slope of the regression of the normalized layer thicknesses is 1.1×10^{-6} and yields a settling velocity of 0.06 mm/s that is closer to typical bulk settling velocities than that calculated from the actual layer thicknesses. This implies that the plume signature is considerably diluted. There are lesser sources of DC in western Newfoundland and the Saint Lawrence River, but these would only affect cores #9–11. If these other DC sources could be accounted for, the regression slope would become steeper yielding a higher settling velocity. However, it does not appear that dilution alone cannot explain the thickness of the H1 layer in the distal region and significant delivery of sediment by ice-rafting must occur.

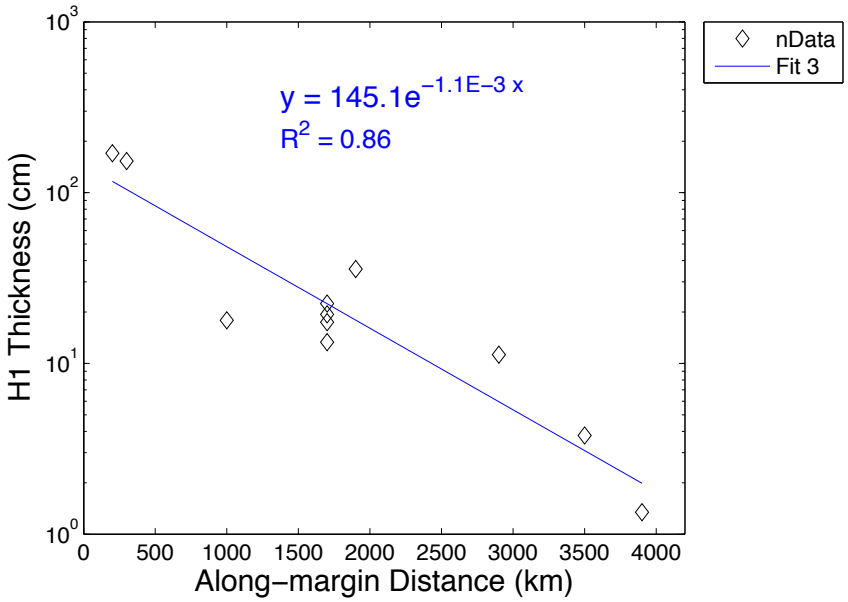

Figure 5.2: H1 layer thickness (cm) by along-margin distance (km) on semilog-y axes. Layer thickness is normalized to median carbonate content for each core to account for dilution by non-Hudson Strait sources. Fit 3 is a linear regression of 11 normalized layer thicknesses and is shown in blue with the equation and R^2 value.

A rapid increase in % $CaCO_3$ is seen between the first and second layer fractions indicating that meltwater and iceberg discharge occurred immediately upon the start of the event. This is also supported by an immediate increase in the sand-gravel content at the beginning of the event. The % sand-gravel remains constant throughout the event indicating that ice-rafting is a consistent method of sediment delivery during the event. After

reaching its maximum near the event start, % $CaCO_3$ slowly decreases for the remainder of the event as plume deposition becomes less important. $CaCO_3$ levels do not return to background levels at the end of the event, but this may be due to post-depositional dilution by bioturbation.

Parameterization of the DIGS spectra provides an additional variable useful in describing the H1 event. Values of m calculated by the inverse floc model show no trend along margin. Because m is a property of the source material, elevated levels during the event indicate a single, distinct source of sediment during the event that is not a significant contributer outside the event. In this way, m acts as a proxy for detrital carbonate content, the unique sediment source during the event. Cross-margin, m reflects the crossing of the main advection trajectory. Temporally, m seems to vary in accordance with % $CaCO_3$ except that maximum levels are not immediately attained at the start of the event and values at the end of the event are even more elevated relative to pre-H1 levels than % $CaCO_3$. Similar to % $CaCO_3$, the failure of the m values to return to background levels may be due to post-depositional dilution by bioturbation.

Other parameters calculated by the inverse floc model are not particularly helpful in describing the H1 event themselves, but do support the event description suggested by other data. As distance from the source increases, the time allotted for particles to settle increases, allowing smaller particles with slower settling speeds to be deposited. Because of this, the size of particles in suspension decreases with distance, and it is expected that $\hat{d}$ and d_f would also decrease. However, $\hat{d}$ and d_f parameters are relatively constant and may even increase slightly with distance from the source. Although this is not expected for sediments deposited purely by plume, this trend can be explained by the hypothesis that plume delivery becomes relatively less important as ice-rafting becomes more relatively important. An increase in $\hat{d}$ and d_f parameters would occur in bottom sediments with proximity to the sediment source, and because ice-rafting delivery is not a sorting process, it mimics a moving discharge source. Thus, increases in $\hat{d}$ and d_f would be expected as the importance of ice-rafting to sediment delivery increases. Cross-margin, $\hat{d}$ and d_f do not show evidence indicating the main trajectory is crossed as other data do.

5.3 Comparison with Facies Interpretations

Interpretation of sediment texture and facies within H layers from the Labrador Sea have both revealed plume fallout, ice-rafting, and turbidity current sediment delivery mechanisms, although sediment delivery by turbidity currents is sometimes divided into fast and slow mechanisms by facies analysis [i.e., *Hesse and Khodabakhsh*, 1998]. However, the delivery mechanism suggested by a particular sample DIGS distribution does not always align with the delivery mechanism suggested by facies interpretations. For example, the H1 layer of core # 1 contains all three subunits that are easily distinguished from photographs and x-radiographs in Appendix A (subunit A: 555–568cm , B: 465–568cm , and C: 388–465cm). All but one sample in this core with a group #3 DIGS distribution are located within subunit C where x-radiographs do not reveal turbidite structures, while DIGS distributions from samples within structures of subunit C interpreted as turbidites belong to group #2. Similarly, subunit A was identified in 5 of the 11 cores used for DIGS analysis based on a peak in sand-gravel content while carbonate content is steadily increasing from background concentrations to elevated event concentrations. Subunit A is also visually distinct because of the high levels of IRD resulting in coarse texture and dark colour. However, not every DIGS sample distribution taken within subunit A belongs to the ice-rafting group #2. It is important to note that differences in texture at grain sizes of < 100 μm determined here address variability at much smaller scales than typically considered in facies analysis and cannot be distinguished visually from photographs or x-radiographs. This work highlights small scale variability of texture within facies that is often ignored and not always in agreement with facies interpretations.

5.4 Implications

Entropy analysis proved useful for comparing DIGS spectra and provided insight into the H1 event not evident from the other analyses. The textural groupings can be associated with different delivery mechanisms, allowing a richer description of the H1 event. Although other analyses provided support for the description of the H1 event, entropy analysis was the only method that allowed for clear delineation of delivery mechanisms. However, it is important to note that the robustness of this application is limited by post-depositional dilution resulting from bioturbation. For the most part, H1 layer sediments

are plume delivered proximal to Hudson Strait and ice-rafted distally. Plume delivery of sediments distally may occur but is overwhelmed by the more dominant ice-rafting delivery of sediments. Because of this, inferring plume processes based on properties of distal sediments is not recommended. However, the lack of plume deposited sediments distally only implies absence of plume sedimentation and does *not* imply the absence of a freshwater plume. In fact, many researchers have found evidence for decreased surface salinity during H events using δ^{18}O and δ^{13}C [e.g., *Cortijo et al.*, 2005; *Vidal et al.*, 1997; *Elliot et al.*, 2002].

CHAPTER 6

CONCLUSION

Entropy analysis allowed delineation of three distinct delivery mechanisms during the H1 event: plume, ice-rafting, turbidity current. In general, H1 layer sediments are plume delivered proximal to Hudson Strait (< 1000 km) and ice-rafted distally. Plume delivery of sediments distally may occur but is overwhelmed by the more dominant delivery of sediments by ice-rafting. However, the lack of plume deposited sediments distally only implies absence of plume sedimentation and does *n*ot imply the absence of a freshwater plume. Plume delivery is greatest at the beginning of the H event, ice-rafting is constant throughout the event, and turbidity currents are more common toward the end of the event. H1 layer thicknesses, carbonate content, sand-gravel content, and inverse floc model parameters support the spatial and temporal variability described by the entropy analysis. In light of this, inferring plume properties from distally (> 1000 km from Hudson Strait) deposited sediments is not recommended. Differences between mechanistic interpretations based on sediment texture and those based on facies highlight small scale variability of texture within facies that is often ignored and not always in agreement with facies interpretations.

APPENDIX A

CORE SUMMARIES

Summary figures for the cores examined can be found in this appendix. Each core summary spans two pages and each page contains a header providing core ID, location description, GPS location, and water depth. The following core information is presented where available.

Core Photography Photographs of the H1 layer taken after sampling. Depth in core (cm) appears on the left, the top and bottom of the H1 layer are marked by a horizontal black line, and sample locations are marked with a red box.

X-radiographs X-radiographs of the working half of each H1 layer taken prior to sampling. White corresponds to high density. Depths are aligned with core photos to the left.

% $CaCO_3$ The carbonate content by weight of each sample downcore.

% Sand & Gravel The fraction of grains > 63 μm by weight of each sample downcore.

DIGS Downcore log-log, slope-preserving plots of sample DIGS < 100 μm.

Parameters m, $\hat{d}$ (μm), d_f (μm), K_f Variation of inverse floc model parameters downcore.

In all plots, samples taken outside of the H1 layer are considered background samples and are marked with an symbol. Five cores have a subunit A and the position of this facies in the core is indicated by a grey shaded region. If present, samples taken within subunit A are distinguished by filled markers.

#1. 2006040–0045pc

Labrador Sea – mouth of Hudson Strait

60.725866°N 60.551713°W

1589 m water depth

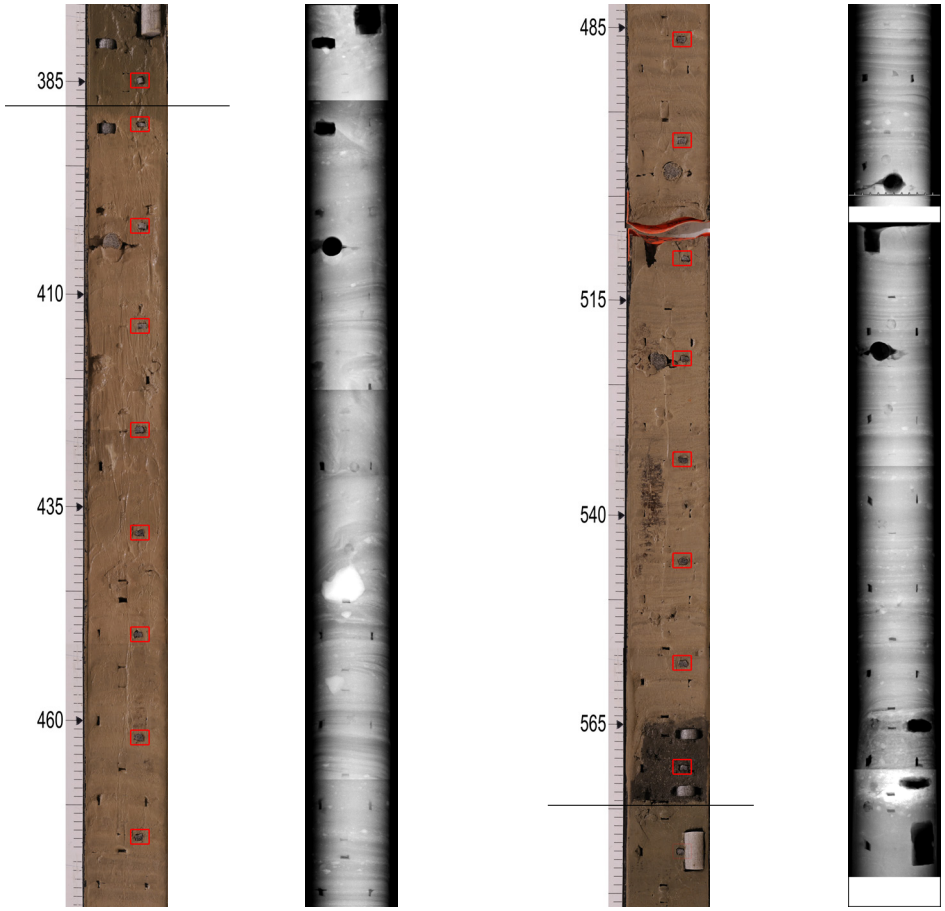

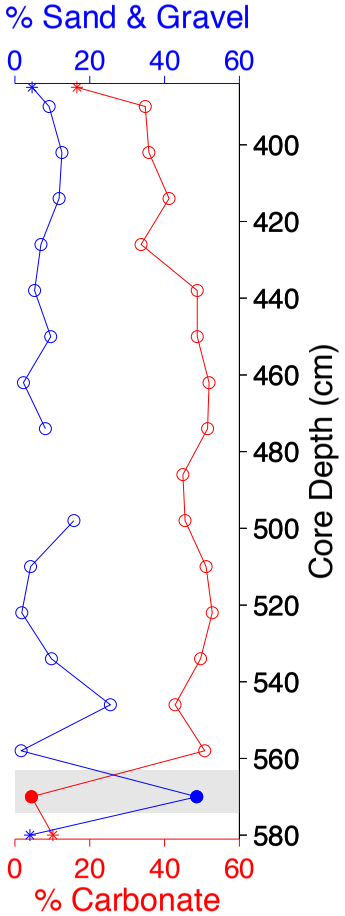

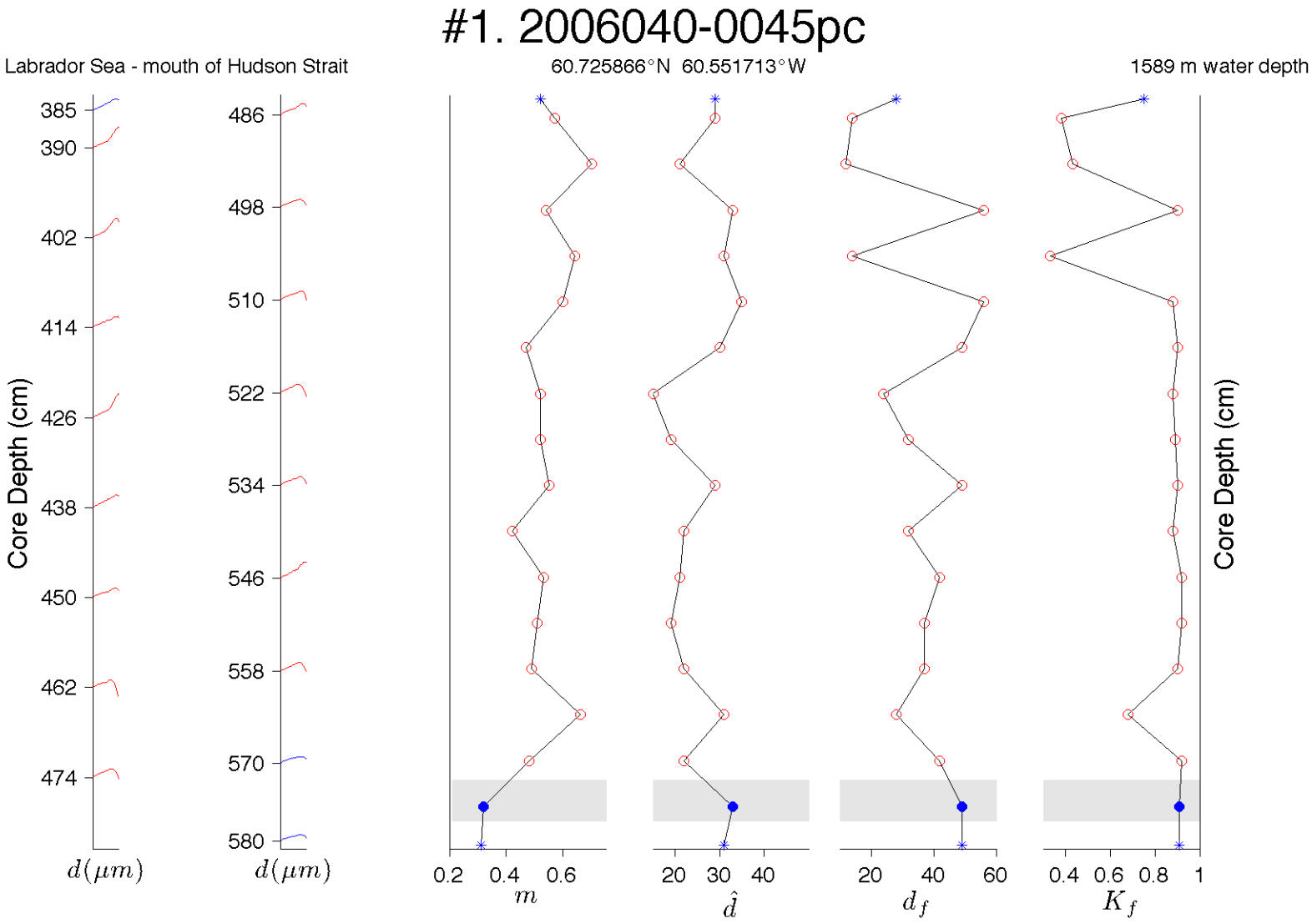
#1. 2006040-0045pc
Labrador Sea - mouth of Hudson Strait
60.725866°N 60.551713°W
1589 m water depth
Core Depth (cm)
385
390
402
414
426
438
450
462
474
$d(\mu m)$
486
498
510
522
534
546
558
570
580
$d(\mu m)$
0.2 0.4 0.6
m
20 30 40
$\hat{d}$
20 40 60
d_f
0.4 0.6 0.8 1
K_f
Core Depth (cm)

#2. 99MD–2233pc

Labrador Sea – slope off Saglek Bank

59.824333°N 59.155833°W

2350 m water depth

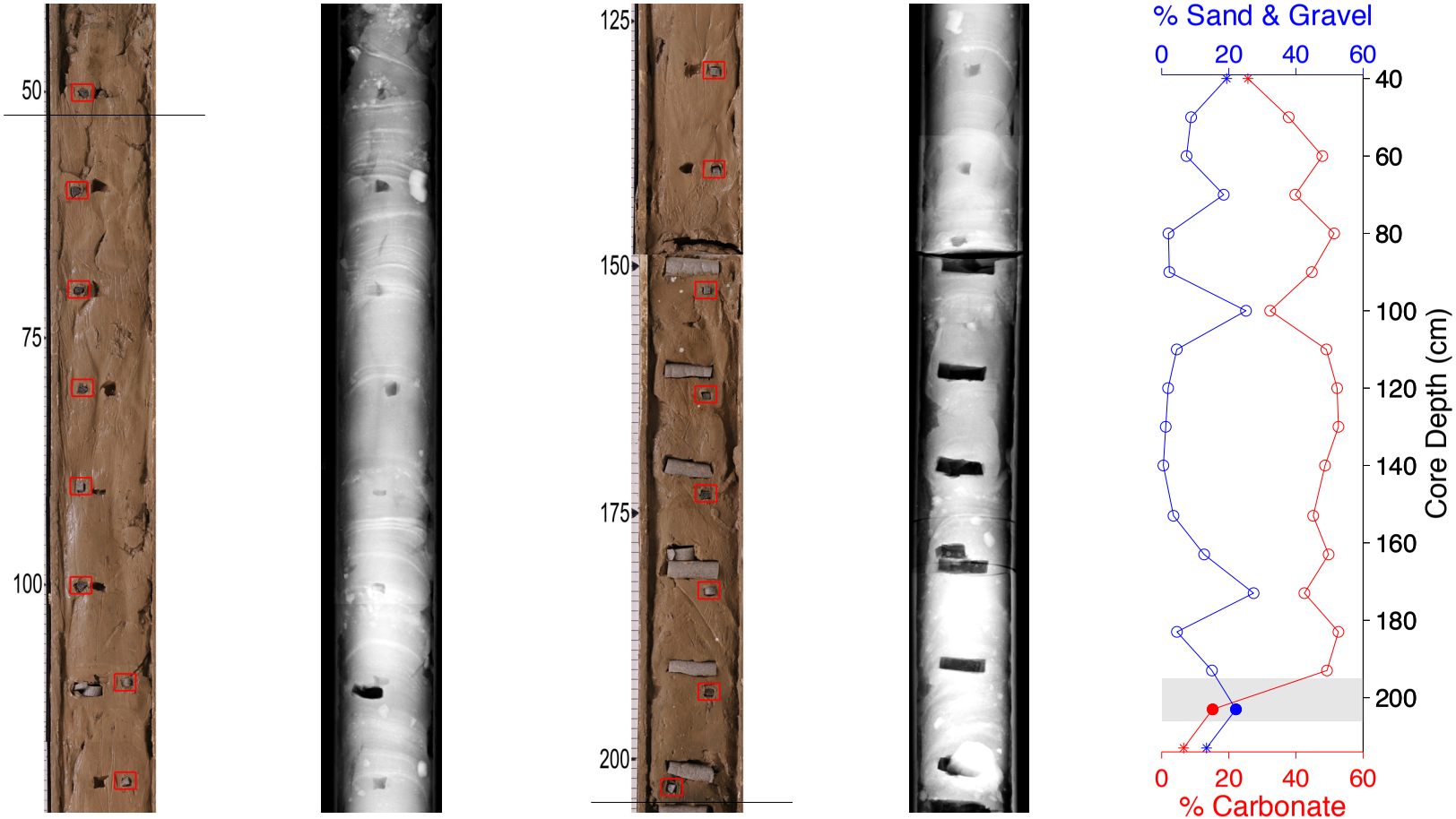

#2. 99MD-2233pc

Labrador Sea - slope off Saglek Bank

59.824333°N 59.155833°W

2350 m water depth

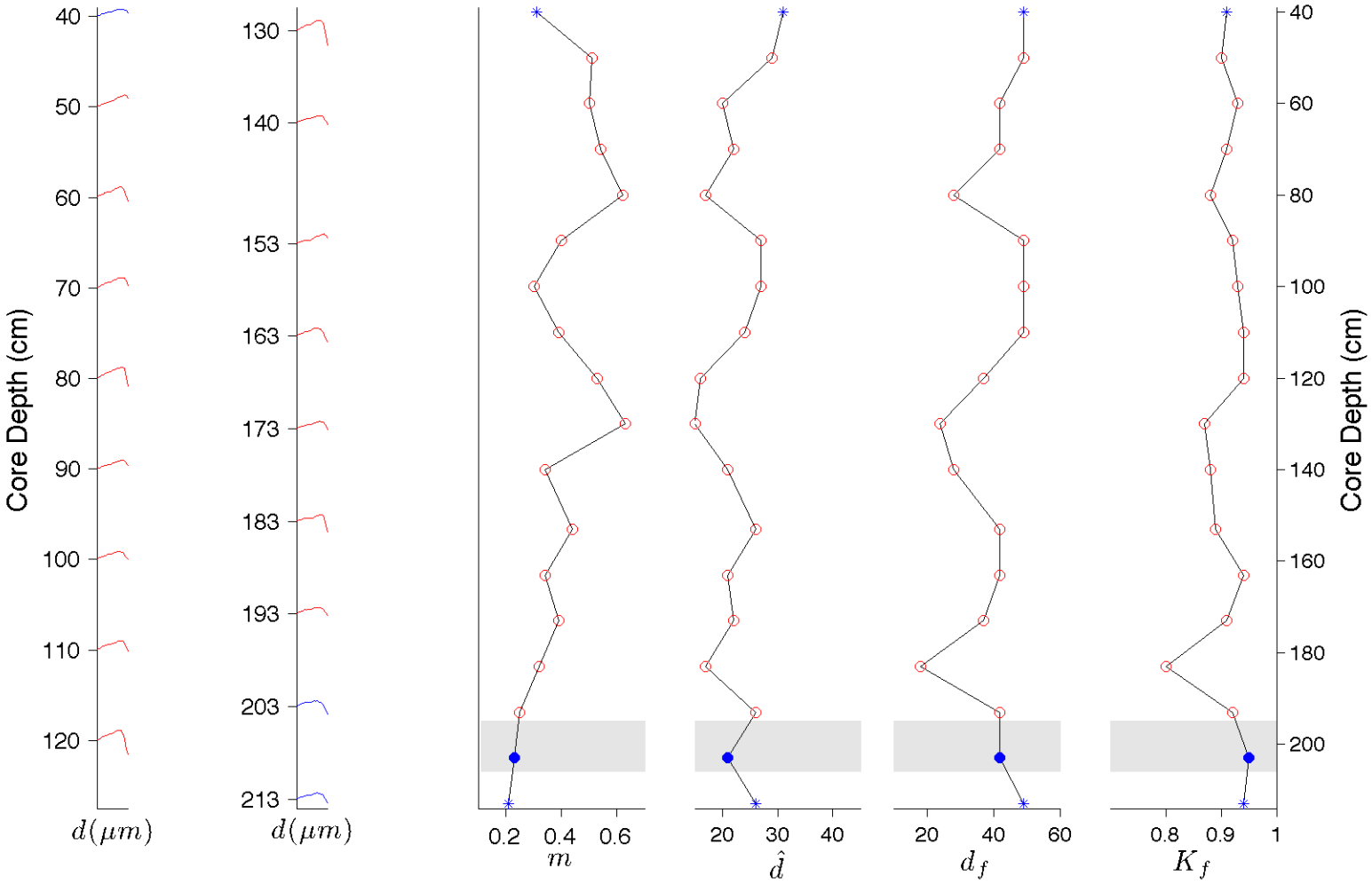

#3. 2005033B–0051pc

Labrador Sea – Hamilton Spur 55.071696°N 51.545544°W 2740 m water depth

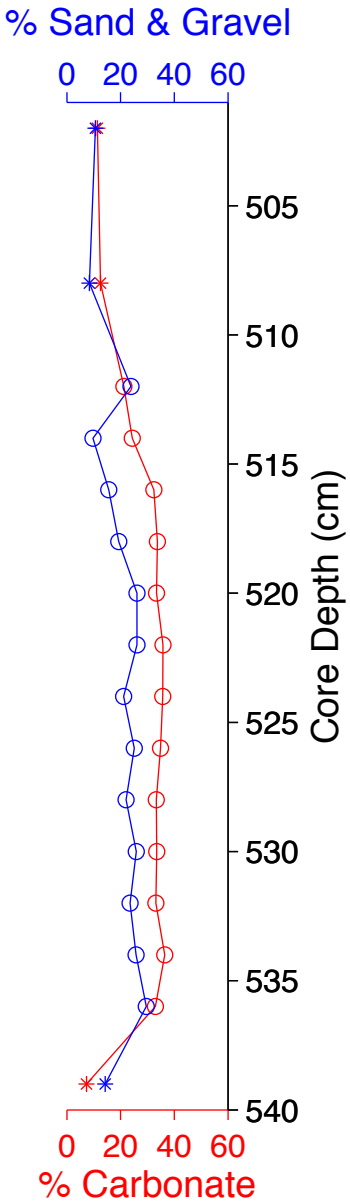

#3. 2005033B–0051pc

Labrador Sea – Hamilton Spur 55.071696°N 51.545544°W 2740 m water depth

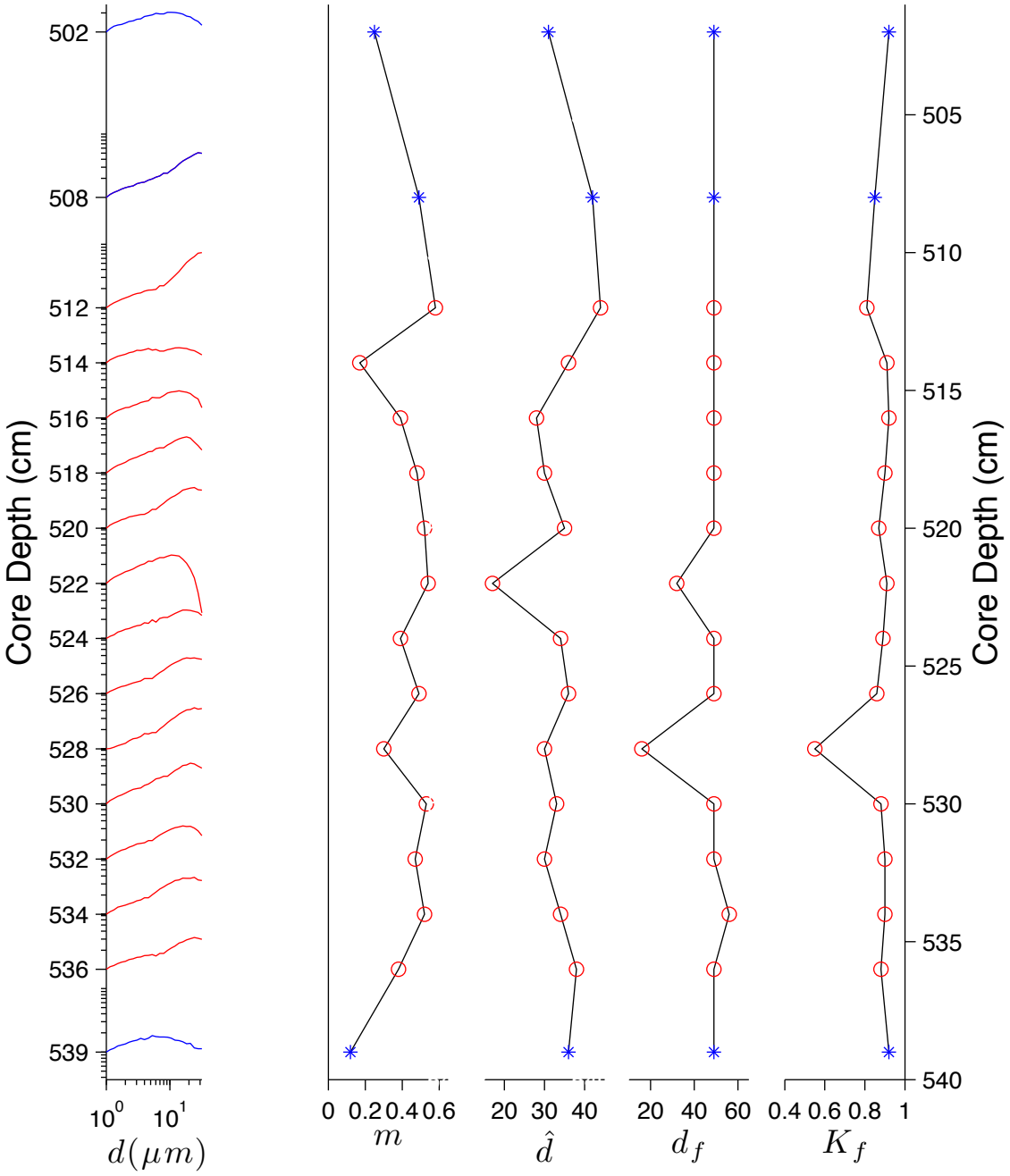

#4. 2004024–0042pc

Labrador Sea – Orphan Knoll 50.378196°N 46.211153°W 1875 m water depth

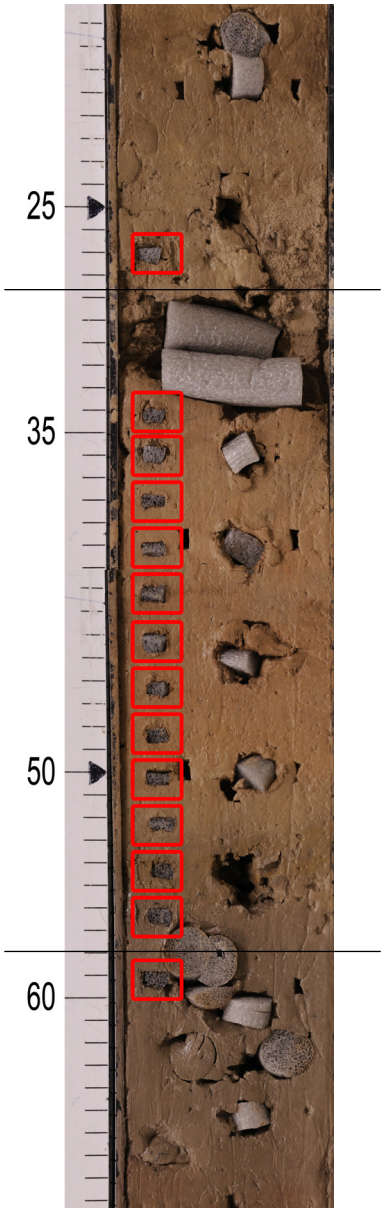

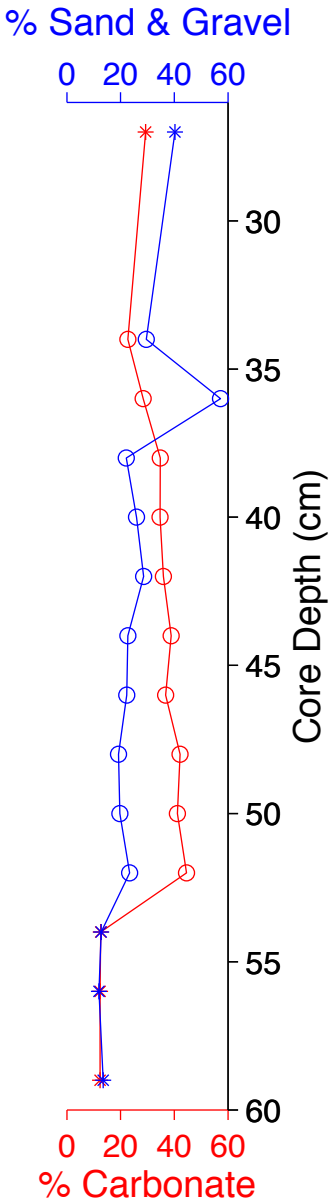

#4. 2004024–0042pc

Labrador Sea – Orphan Knoll 50.378196°N 46.211153°W 1875 m water depth

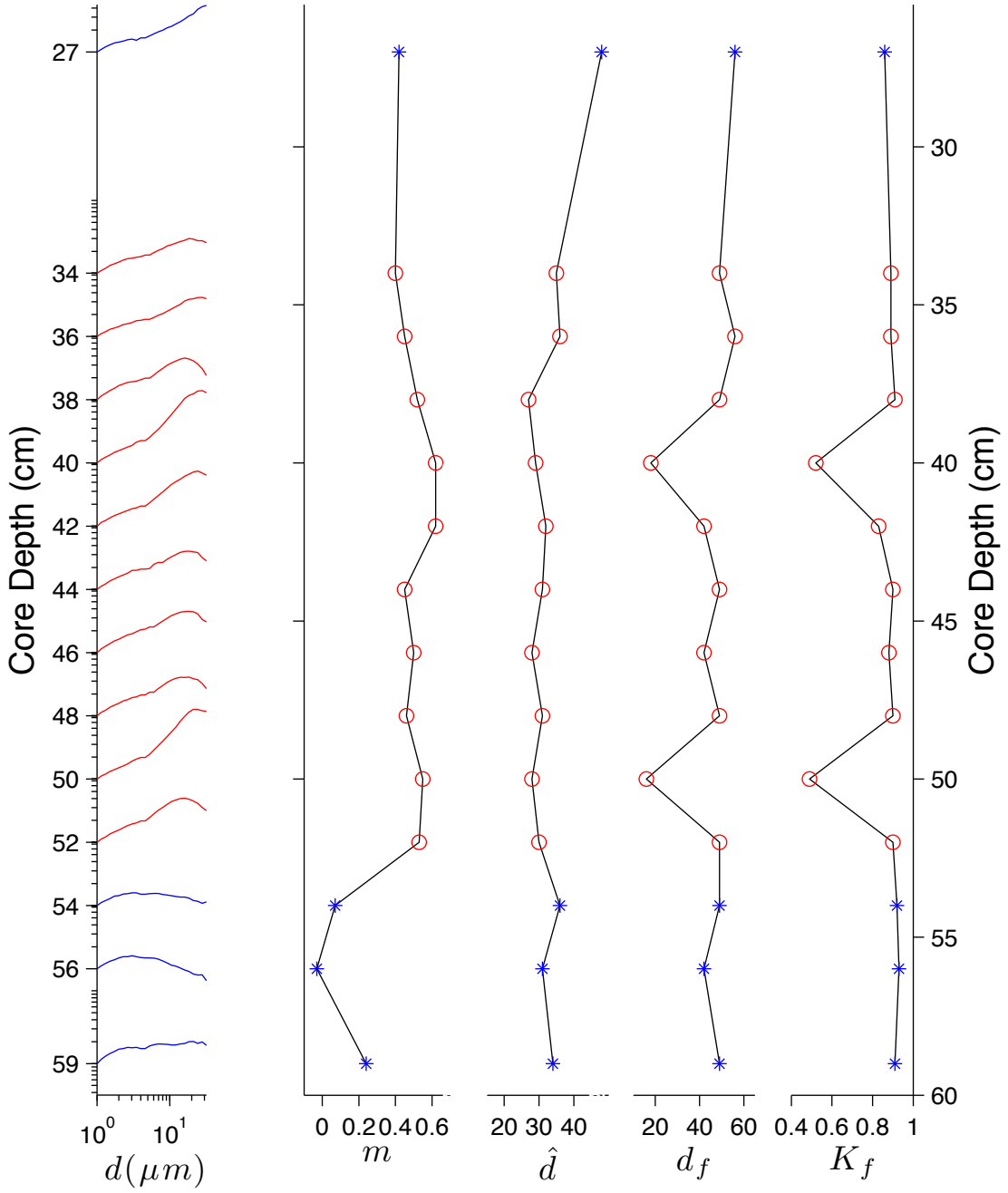

#5. 2004024–0047pc

Labrador Sea – Orphan Basin 49.950746°N 47.400085°W 2691 m water depth

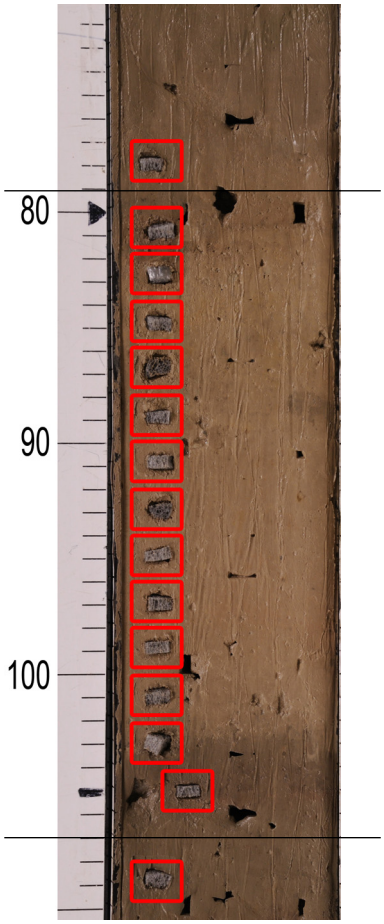

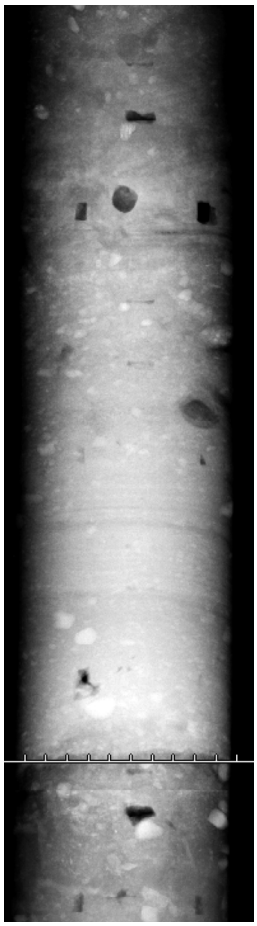

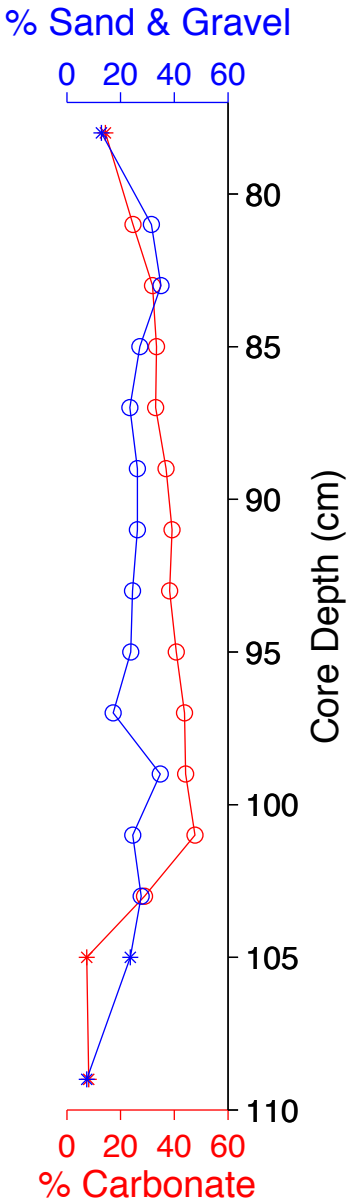

#5. 2004024–0047pc

Labrador Sea – Orphan Basin 49.950746°N 47.400085°W 2691 m water depth

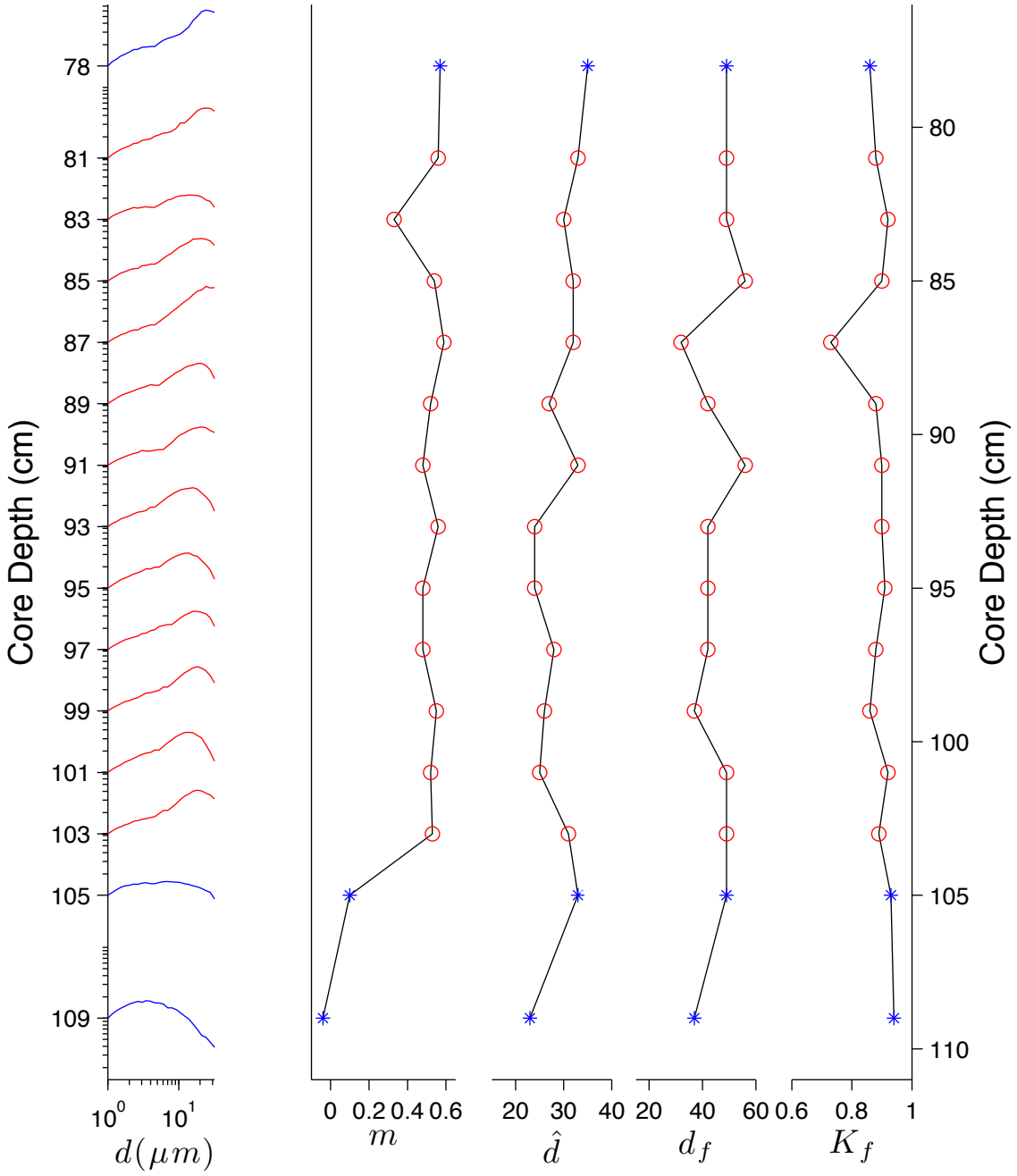

#6. 2004024–0049pc

Labrador Sea – Orphan Basin 49.476120°N 48.163693°W 2322 m water depth

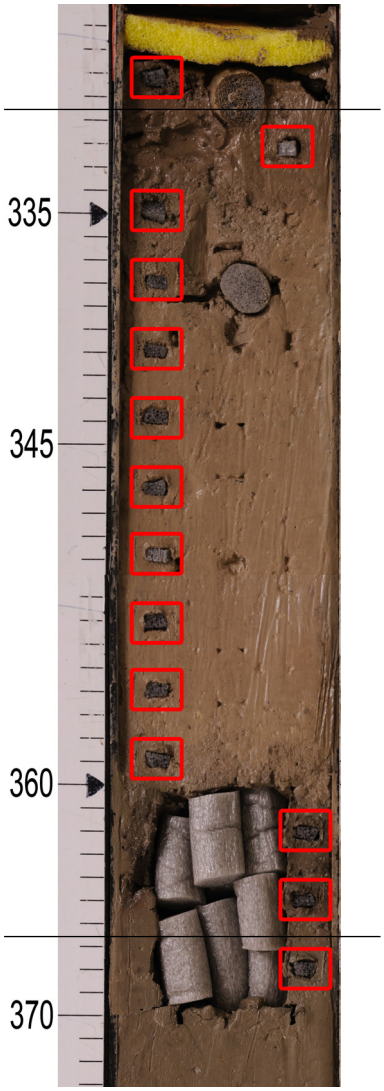

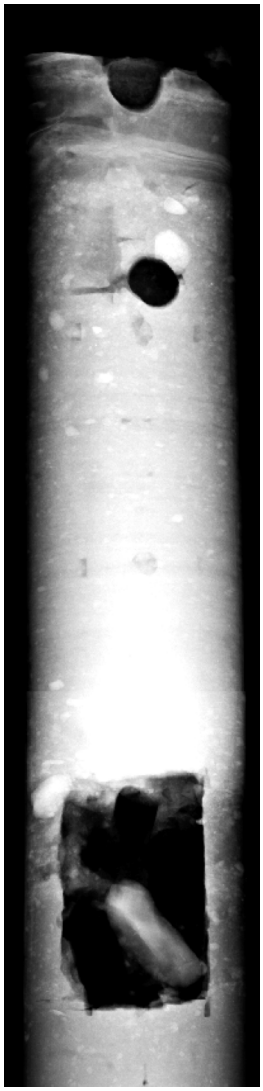

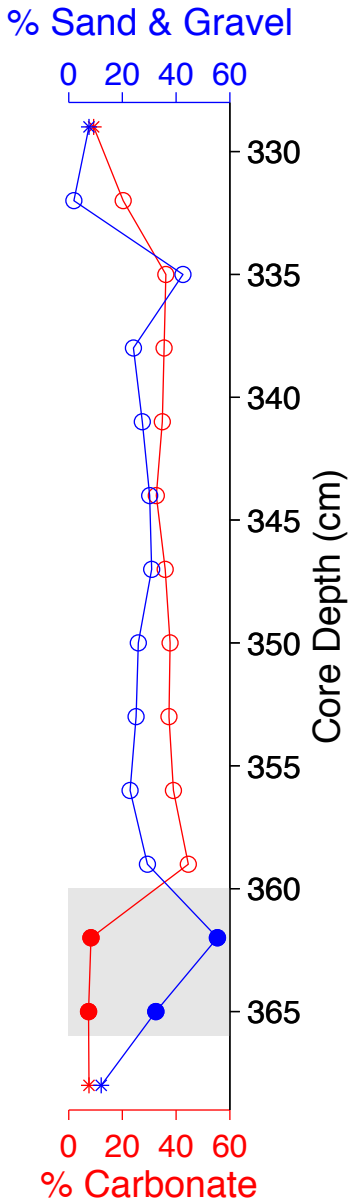

#6. 2004024-0049pc

Labrador Sea - Orphan Basin 49.476120°N 48.163693°W 2322 m water depth

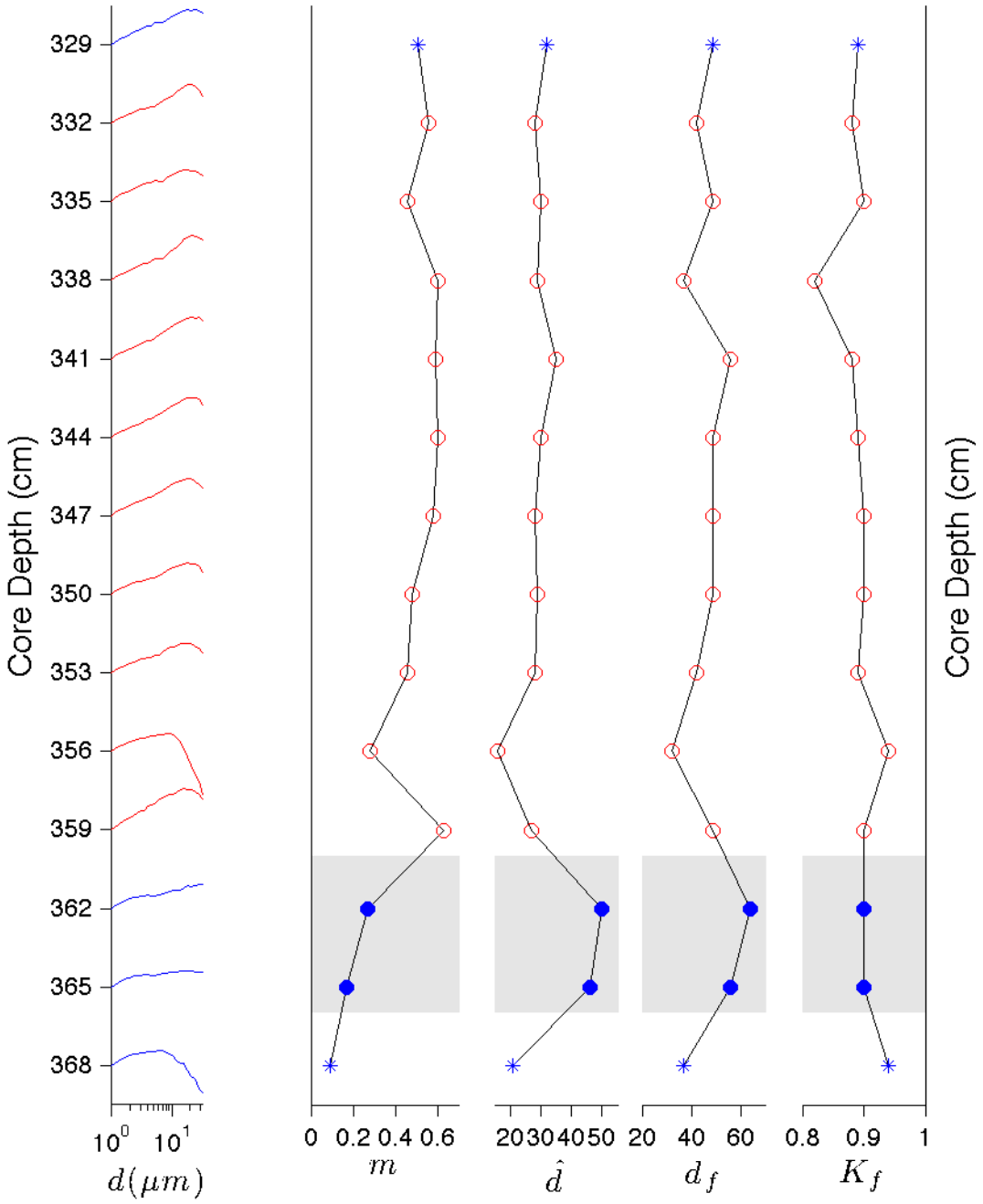

#7. 2003033–0015pc

NE NFLD Slope 48.710150°N 49.641273°W 818 m water depth

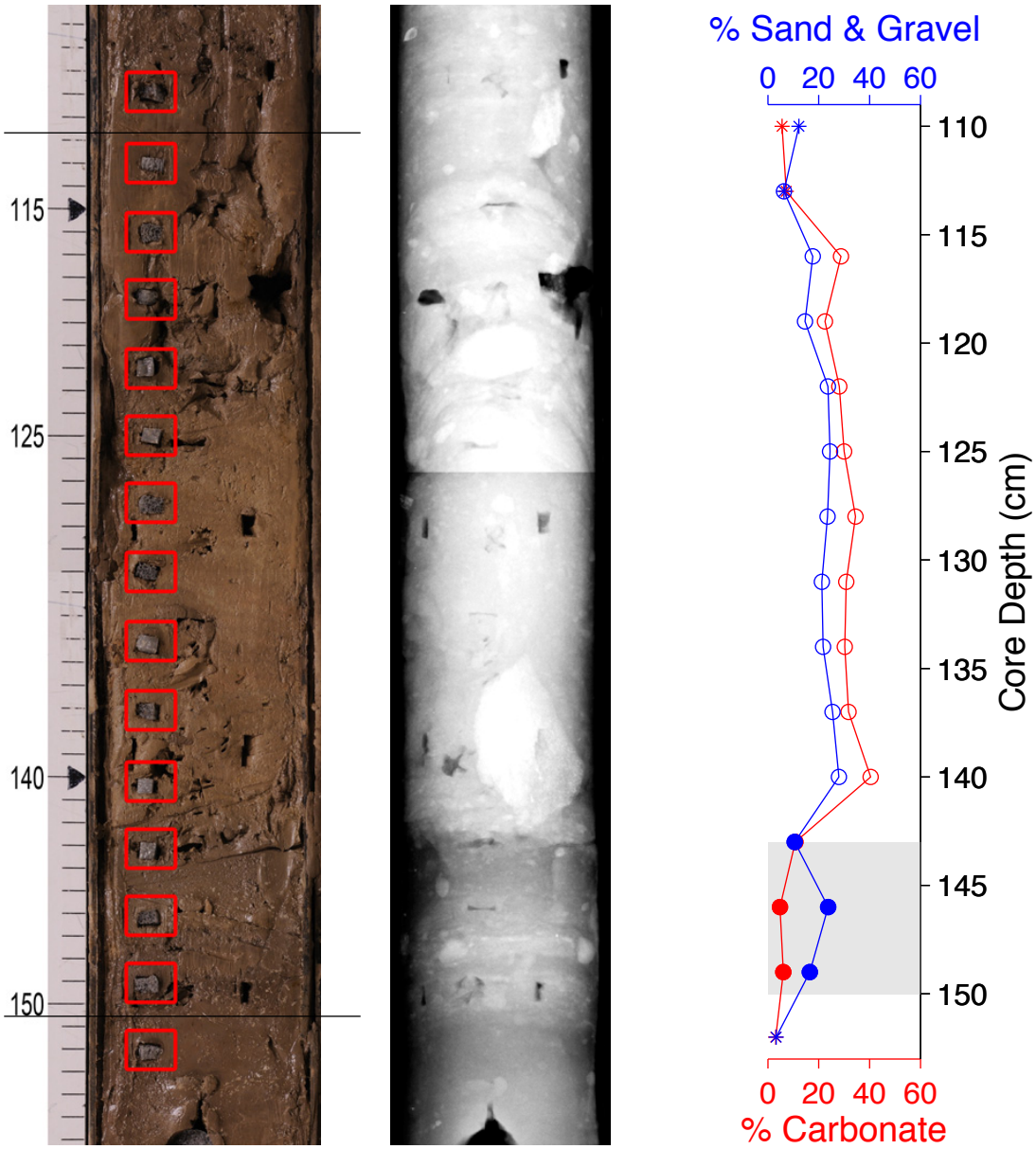

#7. 2003033-0015pc

NE NFLD Slope 48.710150°N 49.641273°W 818 m water depth

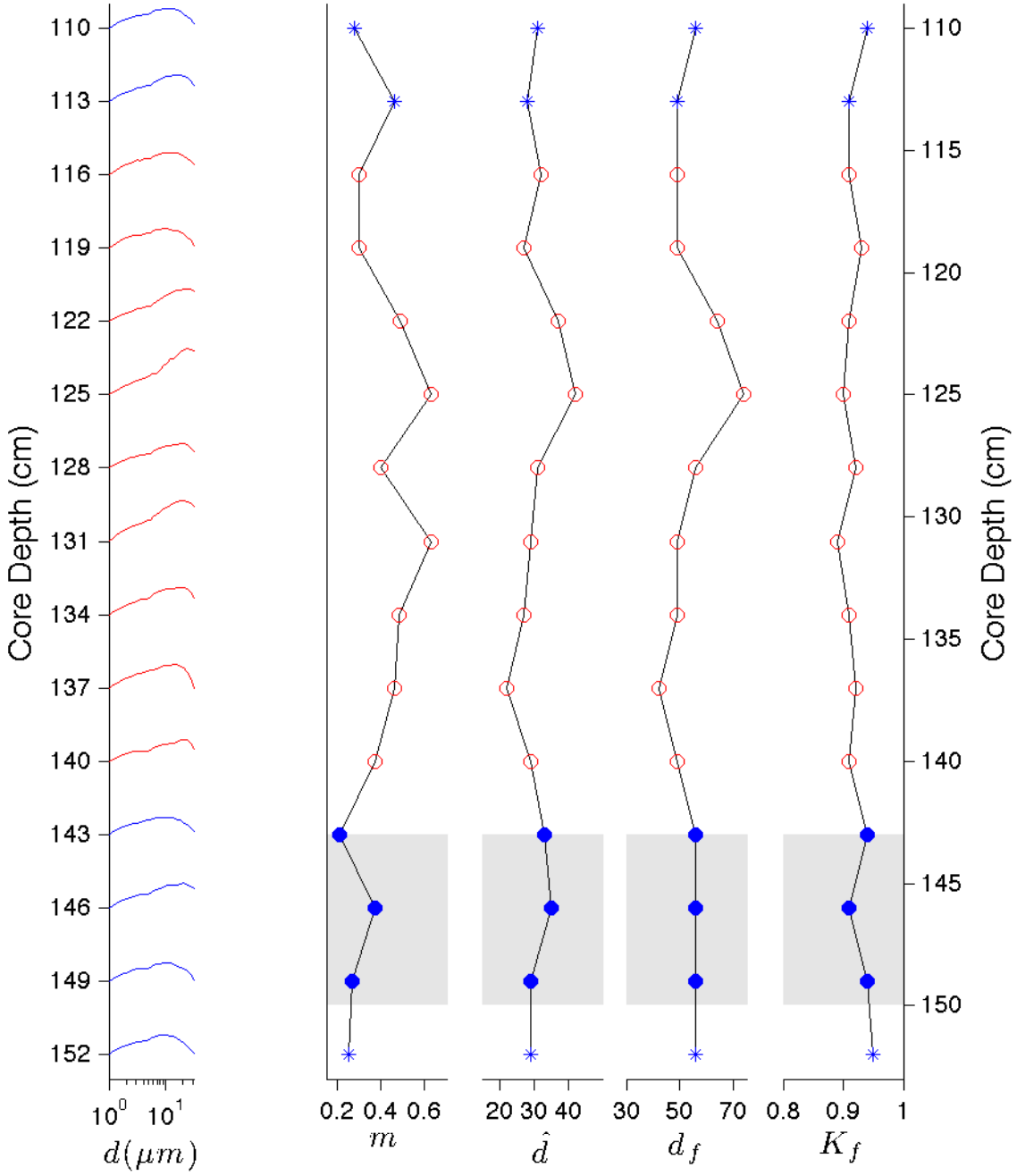

#8. 2006048–0007pc

Grand Banks NFLD – Flemish Pass

47.586376°N 46.374656°W

1134 m water depth

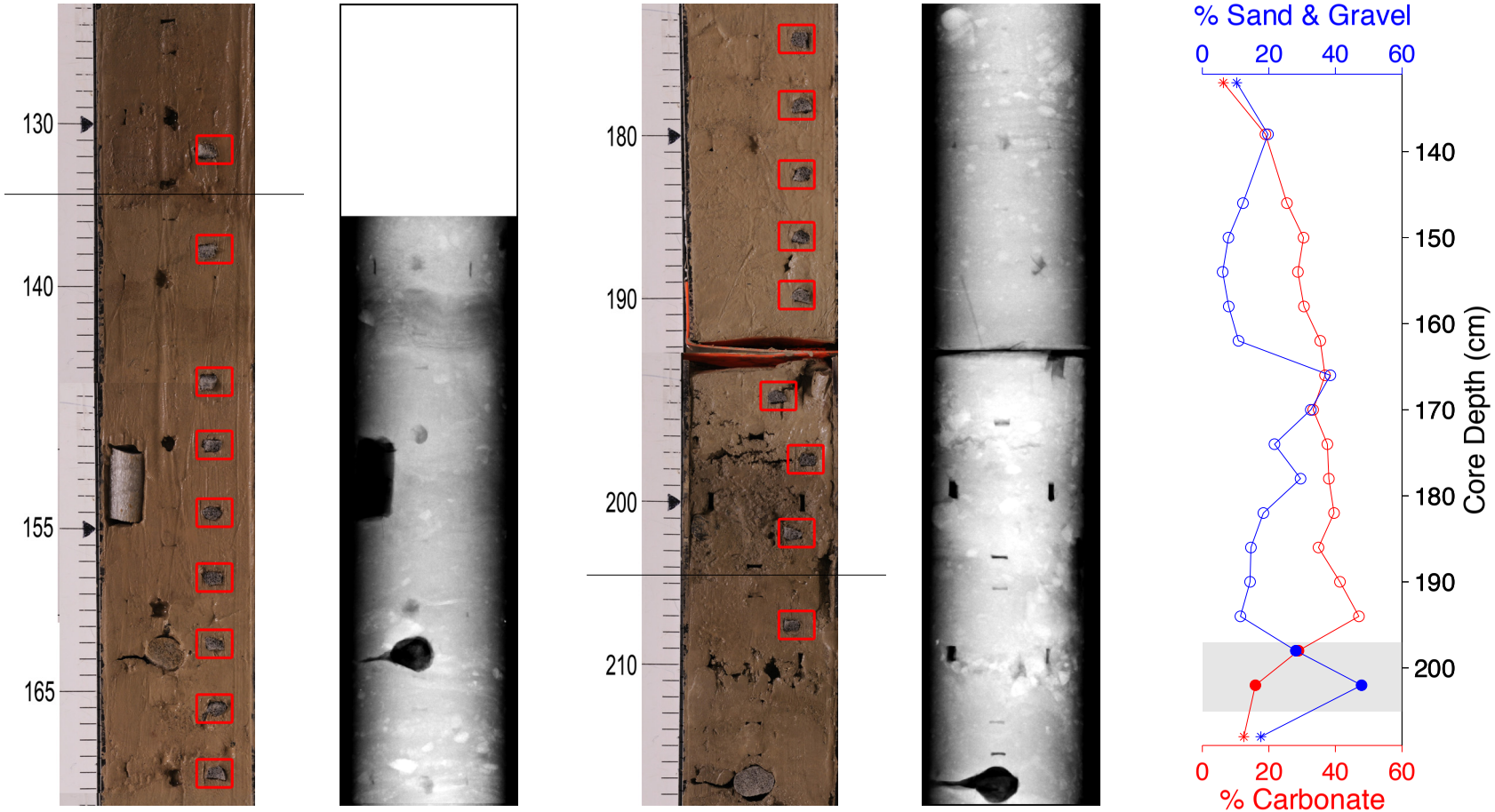

#8. 2006048-0007pc

Grand Banks NFLD - Flemish Pass

47.586376°N 46.374656°W

1134 m water depth

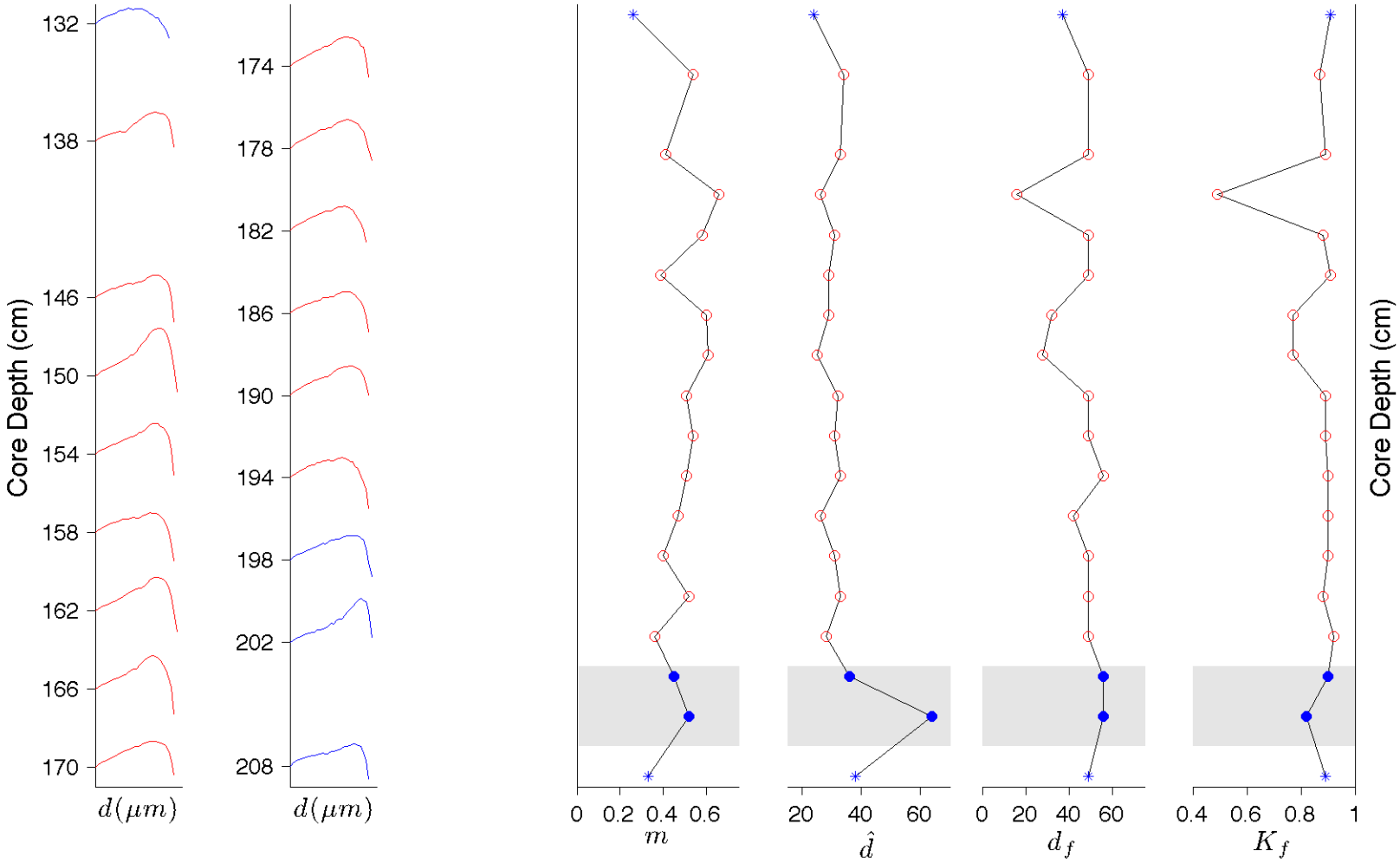

#9. 2004024–0015pc

GB NFLD – DesBarres Canyon 44.265675°N 53.413316°W 1045 m water depth

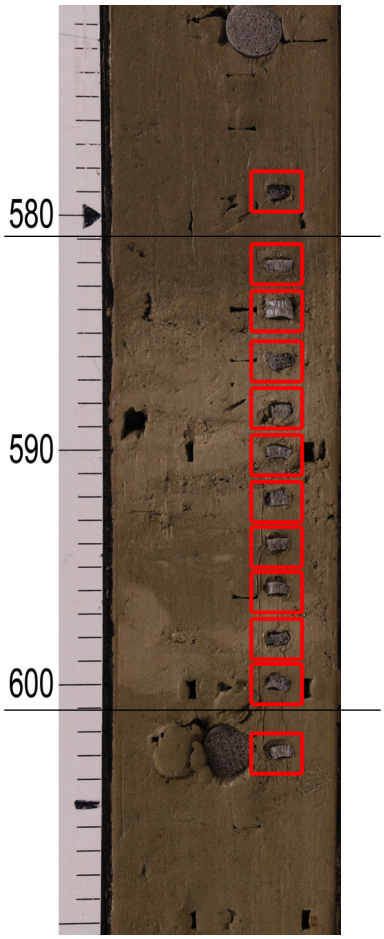

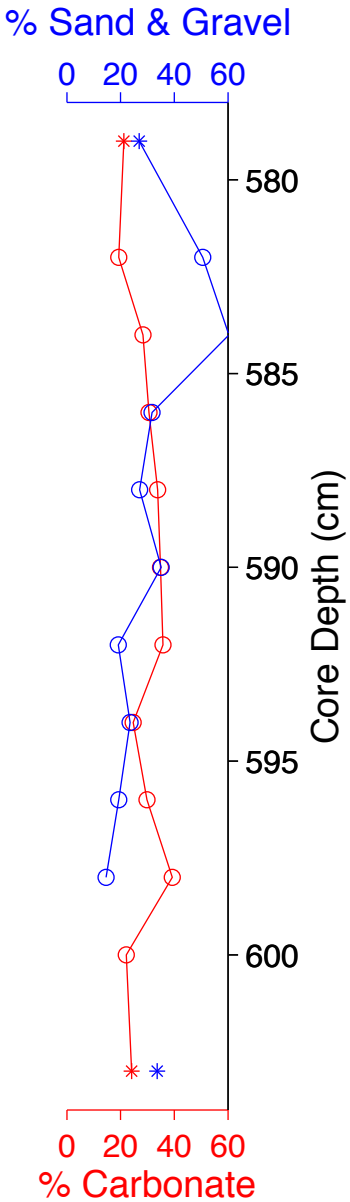

#9. 2004024–0015pc

GB NFLD – DesBarres Canyon 44.265675°N 53.413316°W 1045 m water depth

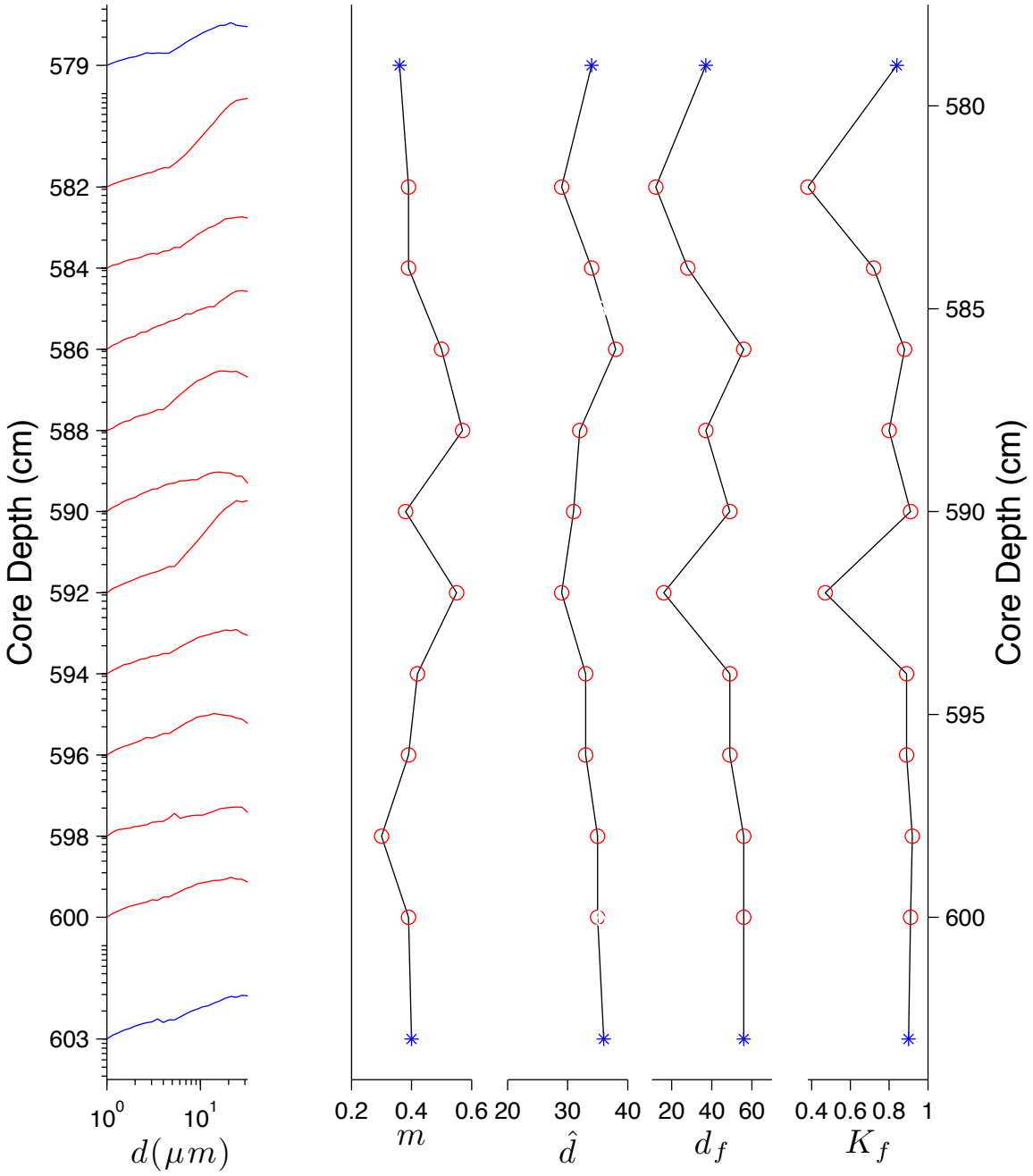

#10. 2002046–0067pc

Scotian Slope – Logan Canyon 43.288488°N 59.643251°W 2564 m water depth

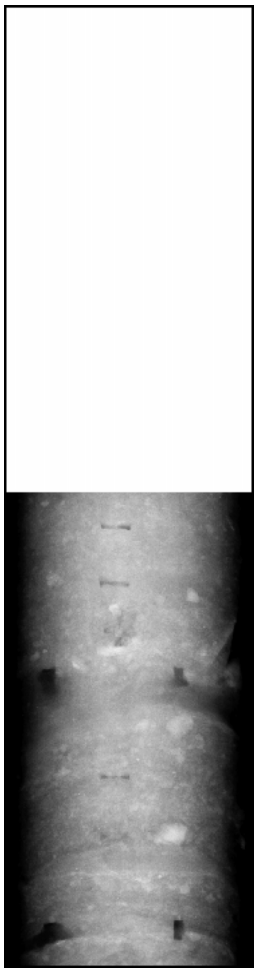

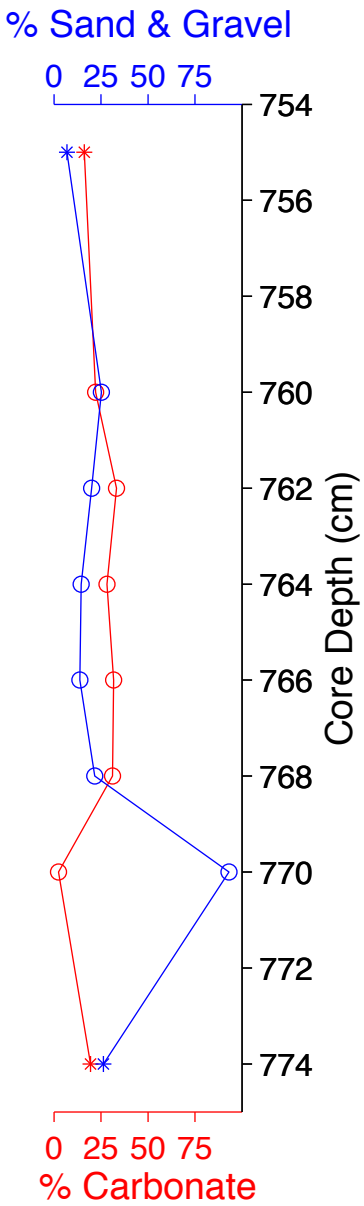

#10. 2002046–0067pc

Scotian Slope – Logan Canyon 43.288488°N 59.643251°W 2564 m water depth

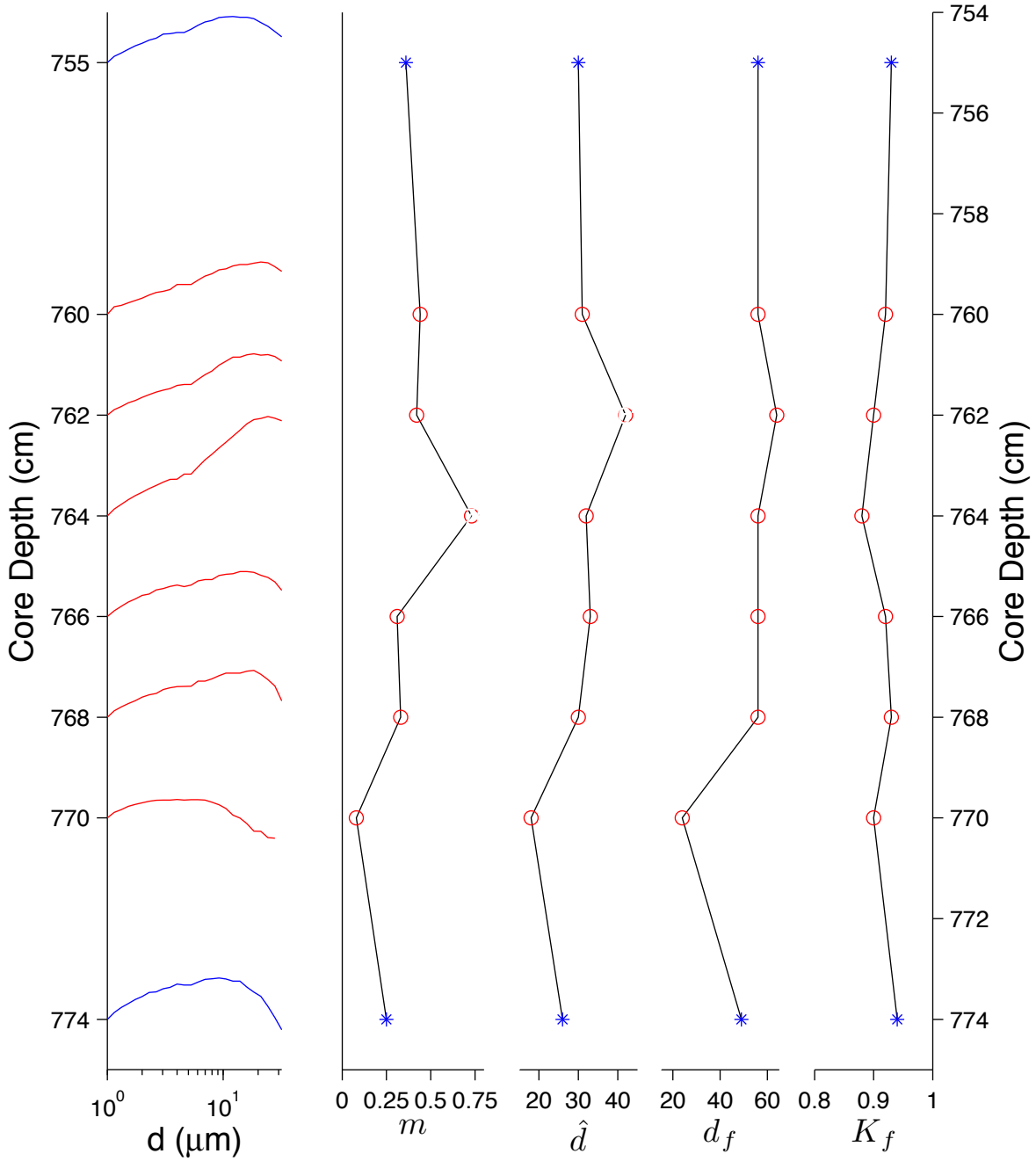

#11. 2002046–0033pc

Scotian Slope off LaHave Bank 42.507875°N 64.288666°W 1270 m water depth

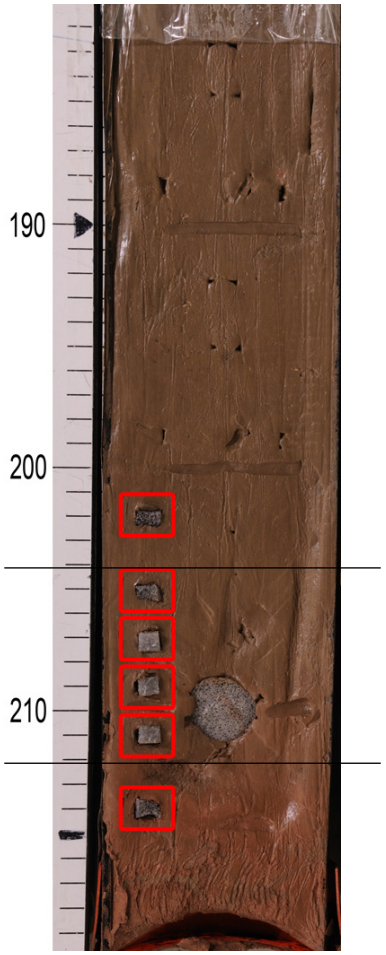

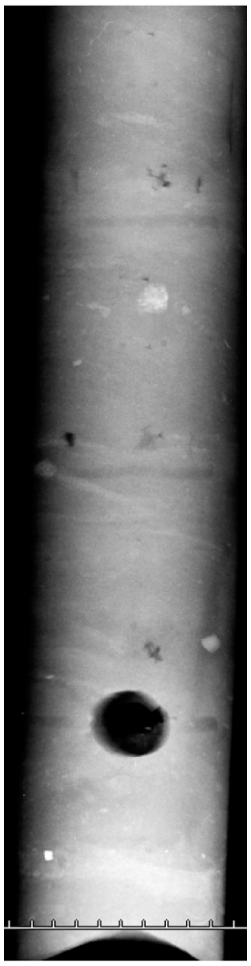

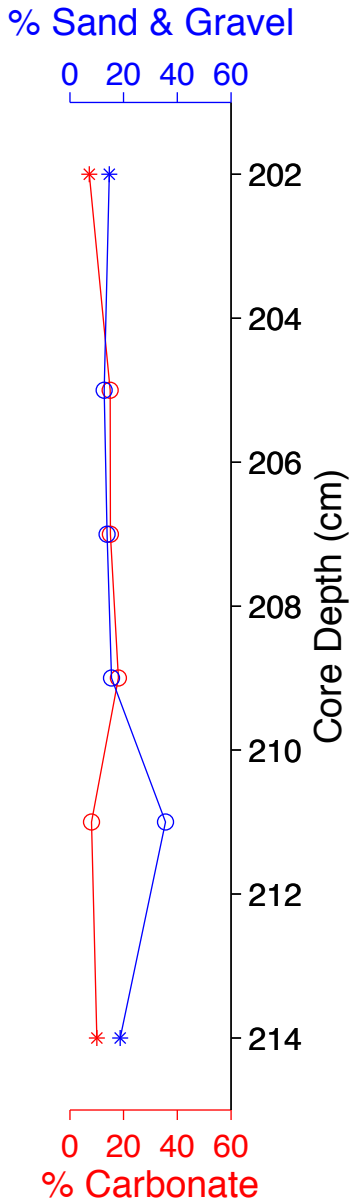

#11. 2002046–0033pc

Scotian Slope off LaHave Bank 42.507875°N 64.288666°W 1270 m water depth

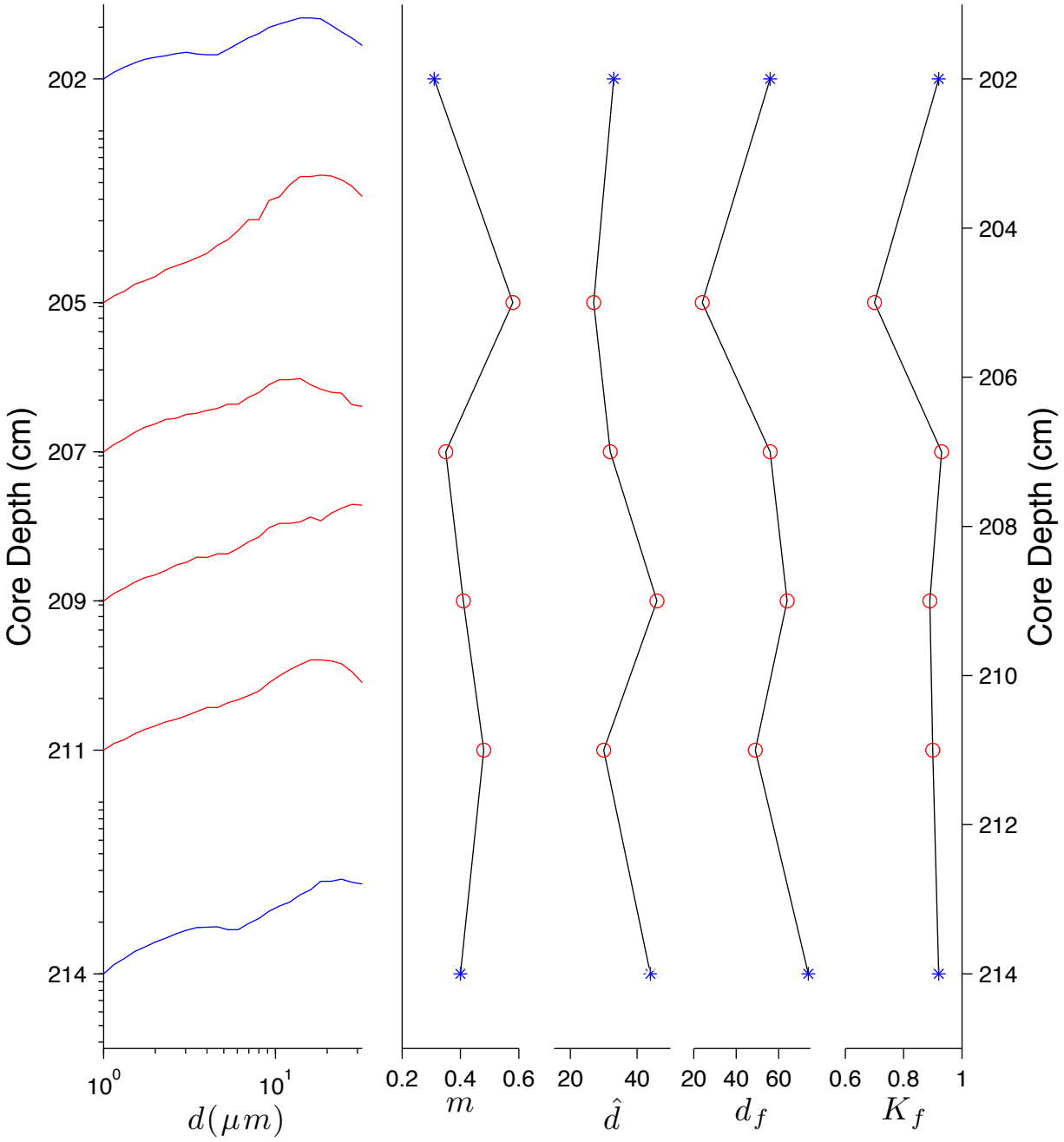

APPENDIX B

ELECTRONIC SUPPLEMENT

The following data used in this research are available digitally at Dalspace
`<http://dalspace.library.dal.ca/>`

H1thick.xls This contains core ID, H1 layer thickness (cm), core depth (cm), along-margin distance (km), and other core information from 104 cores in the study region shown in Fig. 4.1. See Section 3.2 for methods.

DIGS.zip This contains DIGS distributions for all samples from the 11 cores shown in Fig. 3.2. There is one tab delmited .txt file per core. The first column is the bin midpoint diameter (μm) and the remaining columns are samples volume concentrations. The first row is the sample ID and the second row is sample core depth (cm). See Section 3.3 for methods.

CaCO3.xls This contains %$CaCO_3$ by weight (mg) in all samples from the 11 cores shown in Fig. 3.2. See Section 3.4 for methods.

sand&gravel.xls This contains the weight (mg) of the coarse (> 63 μm) and fine (< 63 μm) fractions of grains in all samples from the 11 cores shown in Fig. 3.2. See Section 3.5 for methods.

BIBLIOGRAPHY

Allen, J. R. M., et al., Rapid environmental changes in southern Europe during the last glacial period, *Nature*, *400*, 740–743, 1999.

Andrews, J., and K. Tedesco, Detrital carbonate-rich sediments, northwestern Labrador Sea: Implications for ice-sheet dynamics and iceberg rafting (Heinrich) events in the North Atlantic, *Geology*, *20*, 1087–1090, 1992.

Andrews, J. T., Abrupt changes (Heinrich events) in late Quaternary North Atlantic marine environments: A history and review of data and concepts, *Journal of Quaternary Science*, *13*, 3–16, 1998.

Andrews, J. T., K. Tedesco, W. M. Briggs, and L. W. Evans, Sediments, sedimentation rates, and environments, SE Baffin Bay and NW Labrador Sea 8 to 26 ka, *Canadian Journal of Earth Sciences*, *31*, 90–103, 1994.

Bard, E., F. Rostek, J.-L. Turon, and S. Gendreau, Hydrological impact of heinrich events in the subtropical northeast atlantic, *Science*, *289*, 1321–1324, 2000.

Benson, L. V., J. W. Burdett, M. Kashgarian, S. P. Lund, F. M. Phillips, and R. O. Rye, Climatic and hydrological oscillations in the Owens Lake Basin and adjacent Sierra Nevada, California, *Science*, *274*, 746–749, 1996.

Blunier, T., and E. J. Brook, Timing of millinial-scale climate change in Antarctica and Greenland during the last glacial period, *Science*, *291*, 109–112, 2001.

Bond, G., W. Broecker, S. Johnsen, J. McManus, L. Labeyrie, J. Jouzel, and G. Bonani, Correlations between climate records from North Atlantic sediments and Greenland ice, *Nature*, *365*, 143–147, 1993.

Bond, G., et al., Evidence for massive discharges of icebergs into the North Atlantic ocean during the last glacial period, *Nature*, *360*, 245–249, 1992.

Bond, G. C., and R. Lotti, Iceberg discharges into the North Atlantic on millennial time scales during the last glaciation, *Science*, *267*, 1005–1010, 1995.

Broecker, W., G. Bond, M. Klas, E. Clark, and J. McManus, Origin of the northern Atlantic's Heinrich events, *Climate Dynamics*, *6*, 265–273, 1992.

Broecker, W. S., Massive iceberg discharges as triggers for global climate change, *Nature*, *372*, 421–424, 1994.

Brook, E. J., J. W. C. White, A. S. M. Schilla, M. L. Bender, B. Barnett, J. P. Severinghaus, K. C. Taylor, R. B. Alley, and E. J. Steig, Timing of millinial-scale climate change at Siple Dome, West Antarctica, during the last glacial period, *Quaternary Science Reviews*, *24*, 1333–1343, 2005.

Clark, P. U., N. G. Pisias, T. F. Stocker, and A. J. Weaver, The role of the thermohaline circulation in abrupt climate change, *Nature*, *415*, 863–869, 2002.

Cortijo, E., J.-C. Duplessy, L. Labeyrie, J. Duprat, and D. Paillard, Heinrich events: hydrological impact, *C.R. Geoscience*, *337*, 897–907, 2005.

Cruz, F. W., Jr., S. J. Burns, I. Karmann, W. D. Sharp, M. Vuille, A. O. Cardoso, J. A. Ferrari, P. L. S. Dias, and O. V. Jr, Insolation-driven changes in atmospheric circulation over the past 116,000 years in subtropical Brazil, *Nature*, *434*, 63–66, 2005.

Curran, K. J., P. S. Hill, and T. G. Milligan, The role of particle aggregation in size-dependent deposition of drill mud, *Continental Shelf Research*, *22*, 403–414, 2002.

Curran, K. J., P. S. Hill, T. M. Schell, T. Milligan, and D. J. W. Piper, Inferring the mass fraction of floc-deposited mud: application to fine-grained turbidites, *Sedimentology*, *51*, 927–944, 2004.

Dansgaard, W., et al., Evidence for general instability of past climate from a 250-kyr ice-core record, *Nature*, *364*, 218–220, 1993.

Dowdeswell, J., M. Maslin, J. Andrews, and I. McCave, Iceberg production, debris rafting, and the extent and thickness of Heinrich layers (H-1, H-2) in North Atlantic sediments, *Geology*, *23*, 301–304, 1995.

Elliot, M., L. Labeyrie, and J.-C. Duplessy, Changes in North Atlantic deep-water formation associated with the Dansgaard-Oeschger temperature oscillations (60–10 ka), *Quaternary Science Reviews*, *21*, 1153–1165, 2002.

Francois, R., and M. P. Bacon, Heinrich events in the North Atlantic: Radiochemical evidence, *Deep-Sea Research*, *41*, 315–334, 1994.

Genty, D., D. Blamart, R. Ouahdi, M. Gilmour, A. Baker, J. Jouzel, and S. Van-Exter, Precise dating of Dansgaard-Oeschger climate oscillations in western Europe from stalagmite data, *Nature*, *421*, 833–837, 2003.

Geyer, W., P. Hill, and G. Kineke, The transport, transformation and dispersal of sediment by buoyant coastal flows, *Continental Shelf Research*, *24*, 927–949, 2004.

Gherardi, J.-M., L. Labeyrie, S. Nave, R. Francois, J. McManus, and E. Cortijo, Glacial-interglacial changes inferred from ^{231}Pa/^{230}Th sedimentary record in the North Atlantic region, *Paleoceanography*, *24*, 2009.

Grootes, P. M., M. Stulver, J. W. C. White, S. Johnsen, and J. Jouzel, Comparison of oxygen isotope records from the GISP2 and GRIP Greenland ice cores, *Nature*, *366*, 552–554, 1993.

Grousset, F., L. Labeyrie, J. Sinko, M. Cremer, G. Bond, J. Duprat, E. Cortijo, and S. Huon, Patterns of ice-rafted detritus in the glacial North Atlantic (40–55°N), *Paleoceanography*, *8*, 175–192, 1993.

Gwiazda, R., S. Hemming, and W. Broecker, Provenance of icebergs during Heinrich event 3 and the contrast to their sources during other episodes, *Paleoceanography*, *11*, 371–378, 1996.

Heinrich, H., Origin and consequences of cyclic ice rafting in the Northwest Atlantic Ocean during the past 130,000 years, *Quaternary Research*, *29*, 142–152, 1988.

Hemming, S. R., Heinrich events: Massive Late Pleistocene detritus layers of the North Atlantic and their global climate imprint, *Reviews of Geophysics*, *42*, 2004.

Hemming, S. R., G. C. Bond, W. S. Broecker, W. D. Sharp, and M. Klas-Mendelson, Evidence from $^{40}Ar/^{39}Ar$ ages of individual hornblende grains for varying Laurentide sources of iceberg discharges 22,000 to 10,500 yr B.P., *Quaternary Research*, *54*, 372–383, 2000.

Hendy, I. L., and J. P. Kennett, Dansgaard-Oeschger cycles and the California Current System: Planktonic foraminferal response to rapid climate change in Santa Barbara Basin, Ocean Drilling Program hole 893A, *Paleoceanography*, *15*, 30–42, 2000.

Hesse, R., and S. Khodabakhsh, Depositional facies of late Pleistocene Heinrich events in the Labrador Sea, *Geology*, *26*, 103–106, 1998.

Hesse, R., and S. Khodabakhsh, Significance of fine-grained sediment lofting from meltwater generated turbidity currents for the timing of glaciomarine sediment transport into the deep sea, *Sedimentary Geology*, *186*, 1–11, 2006.

Hill, P. S., J. P. Syvitski, E. A. Cowan, and R. D. Powell, *In Situ* observations of floc settling velocities in Glacier Bay, Alaska, *Marine Geology*, *145*, 85–94, 1998.

Hill, P. S., T. G. Milligan, and W. R. Geyer, Controls on the effective settling velocity of suspended sediment in the Eel River flood plume, *Continental Shelf Research*, *20*, 2095–2111, 2000.

Hill, P. S., et al., *Sediment delivery to the seabed on continental margins*, pp. 49–99, Blackwell Publishing Ltd, 2007.

Hillaire-Marcel, C., A. de Vernal, G. Bilodeau, and G. Wu, Isotope stratigraphy, sedimentation rates, deep circulation, and carbonate events in the Labrador Sea during the last ~200 ka, *Canadian Journal of Earth Sciences*, *31*, 63–89, 1994.

Hulbe, C. L., An ice shelf mechanism for Heinrich layer production, *Paleoceanography*, *12*, 711–717, 1997.

Hulbe, C. L., D. R. MacAyeal, G. H. Denton, J. Kleman, and T. V. Lowell, Catastrophic ice shelf breakup as the source of Heinrich event icebergs, *Paleoceanography*, *19*, 2004.

Hundert, T., and D. J. W. Piper, Late Quaternary sedimentation on the southwestern Scotian Slope, eastern Canada: relationship to glaciation, *Canadian Journal of Earth Sciences*, *45*, 267–285, 2008.

Jenner, K. A., D. J. W. Piper, D. C. Campbell, and D. C. Mosher, Lithofacies and origin of late Quaternary mass transport deposits in submarine canyons, central Scotian Slope, Canada, *Sedimentology*, *54*, 19–38, 2007.

Johnson, R. G., and S.-E. Lauritzen, Hudson Bay-Hudson Strait jökulhlaups and Heinrich events: A hypothesis, *Palaeogeography, Palaeoclimatology, Palaeoecology*, *117*, 123–137, 1995.

Johnston, R. J., and R. K. Semple, *Classification using information statistics*, p. 43, Geo-Books, Norwich, 1983.

Keigwin, L. D., and S. J. Lehman, Deep circulation change linked to HEINRICH event 1 and Younger Dryas in a middepth North Atlantic core, *Paleoceanography*, *9*, 185–194, 1994.

Khodri, M., G. Ramstein, D. Paillard, J. Duplessy, and M. Kageyama, Modelling the climate evolution from the last interglacial to the start of the last glaciation: The role of Arctic Ocean freshwater budget, *Geophysical Research Letters*, *30*, 2003.

Kranck, K., Experiments on the significance of flocculation in the settling behaviour of fine grained sediment in still water, *Canadian Journal of Earth Sciences*, *17*, 1517–1526, 1980.

Kranck, K., P. C. Smith, and T. G. Milligan, Grain-size characteristics of fine-grained unflocculated sediments I: 'one-round' distributions, *Sedimentology*, *43*, 589–596, 1996.

Law, B. A., P. S. Hill, T. G. Milligan, K. J. Curran, P. L. Wiberg, and R. A. Wheatcroft, Size sorting of fine-grained sediments during erosion: Results from western Gulf of Lions, *Continental Shelf Research*, *28*, 1935–1946, 2008.

Lebreiro, S., J. Moreno, I. McCave, and P. Weaver, Evidence for Heinrich layers off Portugal (Tore Seamount: 39°N, 12°W), *Marine Geology*, *131*, 47–56, 1996.

MacAyeal, D., Binge/purge oscillation of the Laurentide ice sheet as a cause of the North Atlantic's Heinrich events, *Paleoceanography*, *8*, 775–784, 1993.

McManus, J., R. Francois, J.-M. Gherardi, L. Keigwin, and S. Brown-Leger, Collapse and rapid resumption of the Atlantic meridional circulation linked to deglacial climate signals, *Nature*, *428*, 834–837, 2004.

Mikkelsen, O. A., K. J. Curran, P. S. Hill, and T. G. Milligan, Entropy analysis of in situ particle size spectra, *Estuarine, Coastal and Shelf Science*, *72*, 615–625, 2007.

Milligan, T. G., and K. Kranck, *Electroresistance particle size analyzers*, pp. 109–118, Cambridge University Press, 1991.

Milligan, T. G., P. S. Hill, and B. A. Law, Floculation and the loss of sediment form the po river plume, *Continental Shelf Research*, *27*, 309–321, 2007.

Ohkouchi, N., T. I. Eglinton, L. D. Keigwin, and J. M. Hayes, Spatial and temporal offsets between proxy records in a sediment drift, *Science*, *298*, 1224–1227, 2002.

Orpin, A. R., and V. E. Kostylev, Towards a statistically valid method of textural sea floor characterization of benthic habitats, *Marine Geology*, *225*, 209–222, 2006.

Peterson, L. C., G. H. Haug, K. A. Hughen, and U. Rohl, Rapid changes in the hydrologic cycle of the tropical Atlantic during the last glacial, *Science*, *290*, 1947–1951, 2000.

Piper, D. J. W., Late Cenozoic evolution of the continental margin of eastern Canada, *Norwegian Journal of Geology*, *85*, 231–244, 2005.

Piper, D. J. W., T. Lawrence, K. Gould, and R. Noftall, Report on cores 2004-024 15 and 16, DesBarres Canyon area, SW Grand Banks, *Open FIle 5118*, Geological Survey of Canada, 2006.

Rahmstorf, S., Ocean circulation and climate during the past 120,000 years, *Nature*, *419*, 207–214, 2002.

Rashid, H., and D. J. W. Piper, The extent of ice on the continental shelf off Hudson Strait during Heinrich events 1–3, *Canadian Journal of Earth Sciences*, *44*, 1537–1549, 2007.

Rashid, H., R. Hesse, and D. J. W. Piper, Origin of unusually thick Heinrich layers in ice-proximal regions of the northwest Labrador Sea, *Earth and Planetary Science Letters*, *208*, 319–336, 2003a.

Rashid, H., R. Hesse, and D. J. W. Piper, Evidence for an additional Heinrich event between H5 and H6 in the Labrador Sea, *Paleoceanography*, *18*, 1077–1091, 2003b.

Rasmussen, T. L., D. W. Oppo, E. Thomsen, and S. J. Lehman, Deep sea records from the southwest Labrador Sea: Ocean circulation changes and ice-rafting events during the last 160,000 years, *Paleoceanography*, *18*, 2003.

Ruddiman, W. F., Late Quaternary deposition of ice-rafted sand in the subpolar North Atlantic (lat 40° to 65°N), *Geological Society of America Bulletin*, *88*, 1813–1827, 1977.

Schmitz, W. J., Jr., and M. S. McCartney, On the North Atlantic circulation, *Reviews of Geophysics*, *31*, 29–49, 1993.

Schulz, H., U. von Rad, and H. Erlenkeuser, Correlation between Arabian Sea and Greenland climate oscillations of the past 110,000 years, *Nature*, *393*, 54–57, 1998.

Shannon, C. E., A mathematical theory of communication, *The Bell System Technical Journal*, *27*, 379–423, 623–656, 1948.

Sheldon, R. W., A. Prakash, and W. H. Sutcliffe, Jr., The size distribution of particles in the ocean, *Limnology and Oceanograhpy*, *17*, 327–339, 1972.

Stocker, T. F., Past and future reorganizations in the climate system, *Quaternary Science Reviews*, *19*, 301–319, 2000.

Stott, L., C. Poulsen, S. Lund, and R. Thunell, Super ENSO and global climate oscillations at millennial time scales, *Science*, *297*, 222–226, 2002.

Syvitski, J. P. M., J. N. Smith, E. A. Calabrese, and B. P. Boudreau, Basin sedimentation and the growth of prograding deltas, *Journal of Geophysical Research*, *93*, 6895–6908, 1988.

Tripsanas, E. K., and D. J. W. Piper, Late Quaternary stratigraphy and sedimentology of Orphan Basin: Implications for meltwater dispersal in the southern Labrador Sea, *Palaeogeography, Palaeoclimatology, Palaeoecology*, *260*, 521–539, 2008.

Tripsanas, E. K., D. J. W. Piper, and K. A. Jarrett, Logs of piston cores and interpreted ultra-high-resolution seismic profiles, Orphan Basin, *Open File 5299*, Geological Survey of Canada, 2007.

Veiga-Pires, C., and C. Hillaire-Marcel, U and Th isotope constraints on the duration of Heinrich events H0–H4 in the southeastern Labrador Sea, *Paleoceanography*, *14*, 187–199, 1999.

Vidal, L., L. Labeyrie, E. Cortijo, M. Arnold, J. C. Duplessy, E. Michel, S. Becque, and T. C. E. van Weering, Evidence for changes in the North Atlantic Deep Water linked to meltwater surges during the Heinrich events, *Earth and Planetary Science Letters*, *146*, 13–27, 1997.

Wang, D., and R. Hesse, Continental slope sedimentation adjacent to an ice-margin. II. Glaciomarine depositional facies on Labrador Slope and glacial cycles, *Marine Geology*, *135*, 65–96, 1996.

Wang, Y. J., H. Cheng, R. L. Edwards, Z. S. An, J. Y. Wu, C.-C. Shen, and J. A. Dorale, A high-resolution absolute-dated late Pleistocene monsoon record from Hulu Cave, China, *Science*, *294*, 2345–2348, 2001.

Woolfe, K. J., and K. Michibayashi, "Basic" entropy grouping of laser-derived grain-size data: and example from the Great Barrier Reef, *Computers and Geosciences*, *21*, 447–462, 1995.